



Auto-assemblage de quasicristaux dans des mélanges 2D de sphères dures

Etienne Fayen

► To cite this version:

Etienne Fayen. Auto-assemblage de quasicristaux dans des mélanges 2D de sphères dures. Statistical Mechanics [cond-mat.stat-mech]. Université Paris-Saclay, 2022. English. NNT : 2022UPASP128 . tel-04009728

HAL Id: tel-04009728

<https://theses.hal.science/tel-04009728>

Submitted on 1 Mar 2023

HAL is a multi-disciplinary open access archive for the deposit and dissemination of scientific research documents, whether they are published or not. The documents may come from teaching and research institutions in France or abroad, or from public or private research centers.

L'archive ouverte pluridisciplinaire **HAL**, est destinée au dépôt et à la diffusion de documents scientifiques de niveau recherche, publiés ou non, émanant des établissements d'enseignement et de recherche français ou étrangers, des laboratoires publics ou privés.

Quasicrystal self-assembly in 2D hard sphere mixtures

*Auto-assemblage de quasicristaux dans des mélanges 2D
de sphères dures*

Thèse de doctorat de l'université Paris-Saclay

École doctorale n°564 : physique en Île-de-France (PIF)

Spécialité de doctorat : Physique

Graduate School : Physique, Référent : Faculté des sciences d'Orsay

Thèse préparée au Laboratoire de Physique des Solides (Université Paris-Saclay, CNRS), sous la direction de **Giuseppe FOFFI**, Professeur, le co-encadrement de **Frank SMALLENBURG**, Chargé de Recherche

Thèse soutenue à Paris-Saclay, le 30 novembre 2022, par

Etienne FAYEN

Composition du jury

Marie JARDAT

Professeure, Sorbonne Université

Christos LIKOS

Professeur, Universität Wien

Chantal VALERIANI

Professeure, Universidad Complutense Madrid

Zorana ZERAVCIC

Maîtresse de conférences, Université Paris (PSL)

Présidente

Rapporteur & Examineur

Rapporteuse & Examinatrice

Examinatrice

Titre : Auto-assemblage de quasicristaux dans des mélanges 2D de sphères dures

Mots clés : Quasicristaux, Simulations numériques, Physique statistique

Résumé : Les quasicristaux sont des structures présentant un ordre à longue portée (signalé par la présence de pics de Bragg dans leur diagramme de diffraction), mais sans la périodicité des cristaux traditionnels. L'absence de périodicité leur permet d'adopter des symétries exotiques impossibles sinon. Cet intrigant ordre aperiodique a été initialement découvert dans des alliages métalliques. Par la suite, il a aussi été observé dans plusieurs systèmes de matière molle remarquablement divers tels que des assemblages de micelles, polymères ou nanoparticules... Cela suggère que des mécanismes généraux promeuvent son émergence, au delà des détails des constituants microscopiques des systèmes.

Dans cette thèse, nous tentons d'identifier de tels ingrédients minimaux en utilisant des simulations numériques pour explorer l'auto-assemblage de quasicristaux dans l'un des systèmes les plus simples : des mélanges binaires de sphères dures, confinées à une interface bidimensionnelle. Nous montrons que des quasicristaux de symétrie 8 et 12 basés sur des pavages aléatoires se forment en effet spontanément dans ce système purement entropique. Contrairement à la plupart des autres modèles utilisés jusqu'à présent, les mélanges binaires quasi-2D de sphères dures pourraient être facilement réalisés dans des expériences de colloïdes, permettant une étude en temps réel et dans l'espace direct de quasicristaux à l'échelle micrométrique.

Title : Quasicrystal self-assembly in 2D hard sphere mixtures

Keywords : Quasicrystals, Numerical simulation, Statistical mechanics

Abstract : Quasicrystals are structures that exhibit long range order (as signalled by sharp Bragg peaks in their diffraction patterns), but that lack the periodicity of traditional crystals, allowing them to adopt exotic symmetries prevented by the strong constraint of periodicity. This puzzling aperiodic order was first discovered in metallic alloys. Later on, it has also been observed in several, very different soft matter systems such as assemblies of micelles, polymer melts or nanoparticles... This suggests that general mechanisms promote its emergence, regardless of the microscopic details of the system constituents.

In this thesis, we try to identify such minimal ingredients by using computer simulations to investigate the self-assembly of quasicrystals in one of the simplest models: binary mixtures of hard spheres, confined at a 2D interface. We show that random tiling quasicrystals of symmetry 8 and 12 indeed spontaneously form in this purely entropic system. In contrast to most other models studied so far, quasi-2D binary mixtures of hard spheres could be easily realised in colloidal experiments, allowing direct-space and direct-time study of quasicrystals at the micron scale.

LABORATOIRE DE PHYSIQUE DES SOLIDES

1 RUE NICOLAS APPERT, BÂT 510, ORSAY

UNIVERSITE PARIS-SACLAY

Quasicrystal self-assembly in 2D hard sphere mixtures

PhD candidate
Etienne FAYEN

Supervisors
Frank SMALLENBURG
Giuseppe FOFFI

Jury
Chantal VALERIANI, rapporteure
Christos LIKOS, rapporteur
Marie JARDAT, examinatrice
Zorana ZERAVCIC, examinatrice

September 28, 2022

Contents

Acknowledgements	7
Introduction	9
.1 Basic concepts in quasicrystal theories	11
.1.1 Aperiodic tilings	11
.1.2 High-dimensional representation	13
.2 Soft quasicrystals	16
.3 Quasicrystal stability	18
.4 A brief note on theoretical treatments of quasicrystal stability . .	20
.5 Numerical simulations	21
.6 A minimal model for quasicrystal self-assembly	23
.6.1 Motivations	23
.6.2 Non-additive hard disks mixtures	24
.7 Outline	26
I Infinite pressure	27
I.1 A packing problem	27
I.2 Phase diagram construction	28
I.2.1 Obtaining candidate crystal structures	28
I.2.2 Common tangent construction	31
I.3 Infinite pressure phase diagram of hard disks mixtures	33
I.3.1 Special regions	35
I.4 Random tiling quasicrystals	38
I.4.1 Entropic quasicrystal locking	38
I.5 Effects of non-additivity	40
I.6 Acknowledgements	43
II Finite pressure self-assembly	45
II.1 Numerical experiments	45
II.1.1 Spheres on a plane	45
II.1.2 Event-driven molecular dynamics	46
II.2 Self-assembly results	47
II.2.1 Infinite pressure	47
II.2.2 Finite pressure self-assembly	49

II.3	A new octagonal quasicrystal	52
II.3.1	Random tiling reconstruction	52
II.3.2	A random tiling model	53
II.3.3	Lift to four dimensions	55
II.3.4	Tile concentrations	58
II.3.5	Perpendicular space analysis	61
II.3.6	Simple geometrical constraints	65
II.4	Perspectives	68
II.5	Acknowledgements	70
III	Thermodynamic stability of the dodecagonal quasicrystal	71
III.1	General strategy	72
III.1.1	Common tangent construction with fluid	72
III.1.2	State point choice	72
III.2	Fluid free energy	73
III.2.1	Thermodynamic integration	74
III.2.2	Obtaining an equation of state	75
III.3	Cell approximation	78
III.3.1	General setting	79
III.3.2	Application to our solid phases	80
III.3.3	Approximate phase diagram	83
III.4	Frenkel-Ladd method	84
III.4.1	The method	85
III.4.2	Estimating uncertainties	90
III.4.3	Finite size correction	91
III.4.4	Solids free-energies	91
III.4.5	Finite pressure phase diagram	94
III.5	The random tiling hypothesis	96
III.5.1	Inflation rules	96
III.5.2	Zipper moves	99
III.5.3	Ideal versus random quasicrystals	99
III.6	Perspectives	102
III.7	Acknowledgements	103
	Conclusion	105
	Résumé en français	109
A	Infinite pressure phases	117
A.1	Magic ratios	117
A.2	Deformation paths	117
A.3	Shield-triangle structures	127
A.4	Calculations of the volumes per particle	128

B Automatic detection of non-equilibrated simulations	131
B.1 Linear fit	131
B.2 Normality test	133
B.3 Block averages	133

Acknowledgements

I am grateful to Giuseppe and Frank for taking me onboard for the last 3 years. Learning the arcanae of computer simulation and soft matter physics with this joyful duo remained, even in my grumpy days, a source of intense intellectual satisfaction. In addition to the physics side, their constant support and understanding makes me feel like an extremely lucky PhD student.

To avoid embarrassing omissions and keep the social graph obscure, I address general, but sincere thanks to all those with who we shared knowing smiles and sincere chats.

This thesis was funded by the ANR grant 18-CE09-0025 “SoftQC”.

Introduction

On April 8, 1982, Dan Shechtman conducts routine transmission electron microscopy on aluminium alloy samples at the National Bureau of Standards. The diffraction pattern of one of the samples in the batch plunges him into great perplexity. Indeed, the diffraction pattern of sample 1725 seems to exhibit 10-fold symmetry. Well versed in crystallography, Shechtman knows that a periodic crystal can only adopt one of the so-called crystallographic rotational symmetries, namely 1, 2, 3, 4 or 6-fold. He also knows that the crystallographic zoo houses strange beasts, and starts to investigate the sample in more details, suspecting that the apparent 10-fold symmetry might in fact be caused by the twinning of multiple periodic crystals in different orientations. Further research convinces him that twinning is not the answer. Sample 1725 is a new kind of material, the first of many materials with new symmetries that would trigger a paradigmatic shift in crystallography.

Indeed, before Shechtman's discovery, crystallography treated order and periodicity as equivalent [2]. Ordered materials were assumed to be periodic crystals, that could be described by a periodically repeated *unit cell*. A simple geometrical argument shows that the only allowed rotational symmetries in that case are the “crystallographic” ones. Some structures were known to deviate from the ideal periodic behaviour. For instance, in *incommensurately modulated* phases, the position of the atomic sites of a periodic structure are modulated by a periodic function whose period is incommensurate with the lattice parameter of the base structure [3–5], resulting in an overall aperiodic structure. Examples were also known where the occupancy, or chemical nature of the sites are modulated [6]. Likewise, a few *incommensurate composites* were known, which are composed of multiple weakly interacting periodic sub-structures, with incommensurate lattice parameters [7]. In both cases, the diffraction patterns exhibit sharp Bragg peaks. The modulation manifests itself by additional “satellite” peaks around the main reflections corresponding to the base periodic order [8, 9]. Although they could have suggested the existence of order without periodicity, these structures were considered as rare oddities, and since in all cases they could be easily linked back to base periodic structures, their existence did not challenge the established equivalence between order and periodicity.

In the diffraction pattern measured by Shechtman and reproduced in Figure 1-left, it is not possible to identify a set of main reflections accompanied by satellites. Hence, the structure cannot be rationalised as modulations of an un-

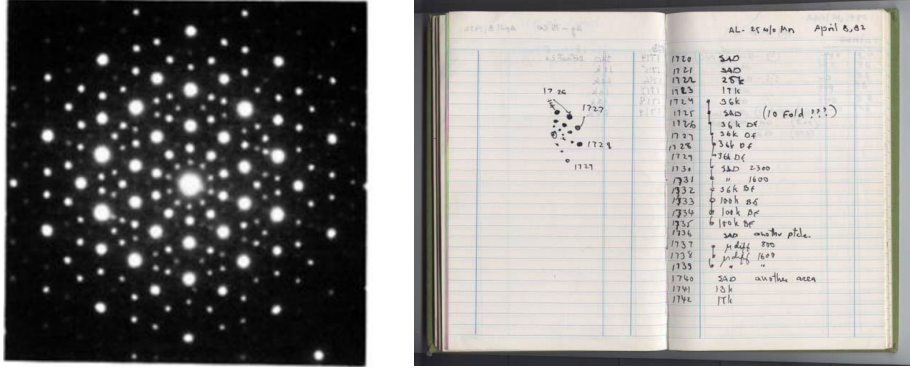


Figure 1: (Left) Electron diffraction pattern of an alloy of aluminium and manganese along an axis with 10-fold symmetry. Taken from Reference 1. (Right) Shechtman's notebook on the page of the April 8th 1982, showing a puzzled annotation about the 10-fold symmetry of sample 1725. Courtesy of Dan Shechtman.

derlying periodic structure. Yet, the existence of sharp Bragg peaks proves the very ordered nature of the solid. Earlier research on mathematical tilings turned out to be a key for the understanding of this discovery. In the 70's, Penrose had studied a family of tilings that now bear his name¹. Penrose tilings exhibit pentagonal symmetry, and incidentally are not periodic. Figure 2 shows a portion of a two-dimensional Penrose tiling made of two tiles: an obtuse and an oblate rhombus. The tiles of this aperiodic tiling can be decorated with particles (for instance putting one particle at each vertex of the tiles) to create an aperiodic yet ordered structure. Before Shechtman discovery, several attempts had been made to construct plausible solid structures based on the Penrose tiling [11, 12]. Mackay built an atomic model based on the 3D Penrose tiling and used an optical diffractometer to directly measure the diffraction pattern [13]. Finally, Levine and Steinhardt were the first ones to recognise Shechtman sample as the first experimental realisation of an aperiodic crystal [14]. They computed the diffraction pattern of a structure based on a 3D generalised Penrose tiling, showed that the peaks matched exactly those found in the experimental measurement, and coined the term *quasicrystal* to name this new kind of ordered but aperiodic materials. A very nice first-hand, personal account of this story by Steinhardt can be found in Reference 15.

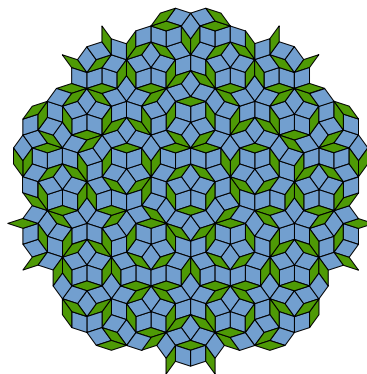
The discovery of the first quasicrystal was met with some scepticism in the ranks of the crystallographers. Indeed, the accuracy of Shechtman's measurements could not rule out some twinning scenarios [16]. Yet, soon enough, quasicrystals started to be discovered in other metallic alloys [17–19], establishing

¹In fact, aperiodic tilings can be found as early as the medieval era, in Islamic architectural art. Their very high degree of perfection suggests that scholars and craftsmen of the time had in-depth knowledge of these structures [10].

the existence of quasicrystals on a much more convincing ground. In 1992, the Commission on Aperiodic Crystals of the International Union of Crystallographers (IUCr) proposed a new definition of *crystal* as “any solid having an essentially discrete diffraction diagram”, hence qualifying quasicrystals as crystals on their own right [20]. Three decades later though, the use of the vocabulary has still not converged, and the terms *crystal*, *quasicrystal*, *aperiodic crystal* and the like are still used differently by different authors. In this work, we try to abide by the definitions proposed by Lifshitz in Reference 2. *Crystal* is used according to the IUCr definition, hence encompassing both periodic and aperiodic ordered structures. We use *quasicrystal* as a synonym for *aperiodic crystal*. Note that, following Lifshitz arguments, we do not require quasicrystals to exhibit a non-crystallographic symmetry, but only to lack periodicity. Indeed, there exist interesting aperiodic crystals with *e.g.* symmetry 4 [21] or 6 (see the hexagonal Stampfli tiling discussed in Chapter III, or Ref. 22).

.1 Basic concepts in quasicrystal theories

The physics of quasicrystals is very rich, with its own peculiar phenomenology. But what makes quasicrystals so rich and fascinating also makes the entry cost for newcomers quite high. In this section, we introduce the essential concepts of quasicrystal theories through the example of the Fibonacci chain. This toy model has been discussed numerous times and in-depth studies can be found in many textbooks [8, 9]. Yet, we discuss it here once again briefly to try make this thesis as self-contained as possible.



.1.1 Aperiodic tilings

Many ordered structures can be naturally described as tilings, *i.e.* space filling arrangements of tiles without gaps or overlaps. The tiles that comprise the tiling are all copies of a finite number of distinct *prototiles*. Periodic crystal can be viewed as periodic tilings of the 2D or 3D space by a single decorated prototile: the unit cell. Likewise, quasicrystals can be rationalised as a set of more than one decorated prototiles used to tile the space in an aperiodic way. Aperiodic tilings are actively studied by mathematicians, and a whole zoo of them have been precisely described². In particular, the three dimensional

Figure 2: Two-dimensional Penrose tiling formed of two tiles. The tiling is aperiodic, but ordered. It exhibits 5-fold rotational symmetry.

²See for instance the tilings encyclopedia, maintained by Frettlöh, Harriss and Gähler: <https://tilings.math.uni-bielefeld.de/>

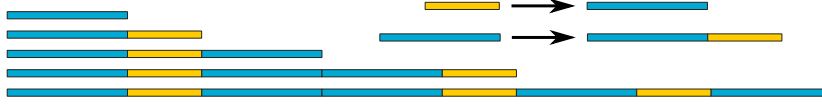


Figure 3: Illustration of the inflation scheme used to generate the Fibonacci chain. As a result of the substitution rules depicted on the right, the tiling obtained at one step is the concatenation of the tilings generated at the two previous steps.

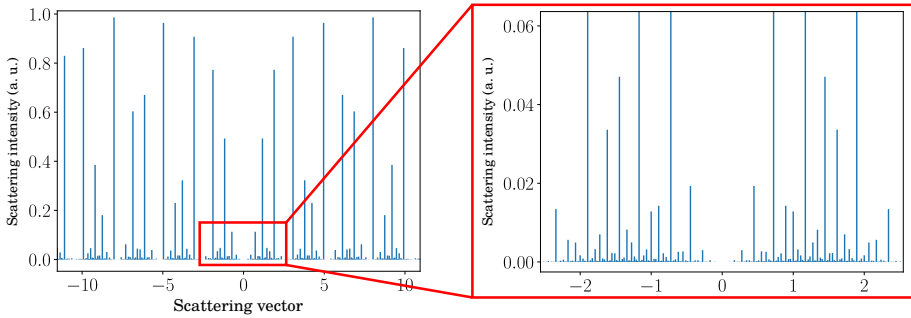


Figure 4: Fourier spectrum of the Fibonacci chain. The spectrum is a discrete but mathematically dense set of Bragg peaks. The right plot is a magnification of the central region, highlighting the self-similarity of the diffraction pattern.

Penrose tiling is used to model the structure of most icosahedral quasicrystals. In two dimensions, structures have been related to the 8-fold symmetric Ammann-Beenker or Watanabe-Ito-Soma tiling [23–26] and 12-fold Stampfli or Schlotmann square-triangle tiling [27, 28].

Let's consider here a one dimensional tiling made of two prototiles (line segments in 1D) of length 1 (S tile) and $\tau = (1 + \sqrt{5})/2$ the golden mean (L tile). We generate the tiling by the so-called *inflation method*. Starting from an initial seed, we apply recursively the following substitution rules:

$$\begin{aligned} S &\rightarrow L \\ L &\rightarrow LS. \end{aligned} \tag{1}$$

The procedure is illustrated in Figure 3. When repeated *ad infinitum*, it generates an aperiodic tiling that geometrically realises the Fibonacci sequence: step n of the inflation is the concatenation of steps $n - 1$ and $n - 2$, similarly to the Fibonacci recurrence relation $F_n = F_{n-1} + F_{n-2}$.

If tiles are decorated with one particle at each contact point between adjacent tiles, one obtains a 1D quasicrystal. Its order is revealed by its diffraction pattern displayed in Figure 4, which is discrete³. However, in contrast to periodic crystals which exhibit discrete but sparse diffraction patterns, that of

³Note that the existence of order cannot be inferred by the existence of the deterministic

the Fibonacci chain and quasicrystals in general are dense in the mathematical sense: in any volume, no matter how small, around a diffraction peak, another diffraction peak can be found [9]. In practice however, if this quasicrystal was realised in an experiment, only a few peaks would carry enough of the incident intensity to be detected. Another striking feature of the diffraction pattern is the self-similarity property. Figure 4-right is a magnification of the highlighted region, which reproduces essential features of the full diffraction pattern. This is the counterpart in Fourier space of the self-similarity of the Fibonacci chain in direct space enforced by the successive concatenations. Fractal properties are a general feature of ideal quasicrystals.

1.2 High-dimensional representation

All Bragg peaks in the diffraction pattern of a periodic crystal in dimension d are located at integer combinations of d linearly independent vectors in Fourier space. Hence, they can be indexed in a unique way (up to a choice of origin) with d integers. For quasicrystals, $D > d$ integers are required. In the case of the Fibonacci chain, two integers are necessary ($d = 1$, $D = 2$), corresponding to the two vectors that generate the positions of the peaks. In this one-dimensional example, the vectors are simply real numbers, proportional to the inverse length of the small and large tiles. Note that while D vectors are necessarily linearly dependant over \mathbb{R} in a d -dimensional vector space, the D d -dimensional vectors used to index the diffraction patterns of quasicrystals are linearly independent *over the integers*. They generate a \mathbb{Z} -module which is mathematically dense, like their diffraction patterns.

This observation motivates the so-called hyperspace, or high-dimensional representation of quasicrystals. By analogy with the periodic case, aperiodic crystals of rank D (*i.e.* whose diffraction pattern is uniquely indexed by D vectors) can be represented as periodic crystals in dimension D , projected onto the physical or so-called *parallel space* E^{\parallel} of dimension d . The complementary space of dimension $D - d$ orthogonal to E^{\parallel} is the *perpendicular space* (or sometimes perp-space) E^{\perp} . The Fibonacci chain is a quasicrystal of rank two, so it can be represented as the projection of a 2D periodic crystal onto a line, as depicted in Figure 5-top. Consider a square grid of unit-cell size 1, cut by an axis with angle α . This axis is the parallel space E^{\parallel} . If the slope of the parallel space with respect to the grid is a rational number p/q , then the projection of the grid vertices onto E^{\parallel} generates a periodic structure with period q . With an irrational slope however, the projection of the grid results in a mathematically dense set of points in E^{\parallel} which is not physical for a realistic structure. To fix this, only the vertices inside a strip are projected. This amounts to imposing that the projected vertices belong to a so-called *selection region* in perpendicular space (thick green segment in E^{\perp} in Figure 5). The Fibonacci chain is

construction procedure. Indeed, the Thue-Morse substitution rule $L \rightarrow LS$, $S \rightarrow SL$ generates a sequence with no long range order (no Bragg peaks). Determinism does not imply long range order [29].

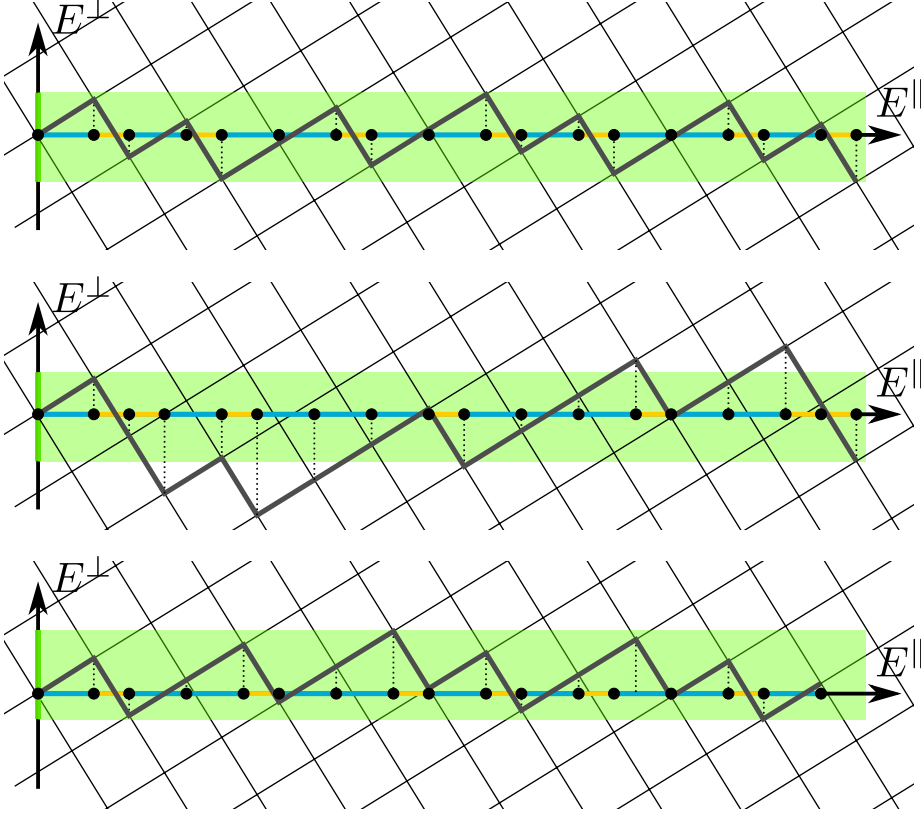


Figure 5: High-dimensional representation of the Fibonacci chain. The square grid has an irrational slope with respect to the parallel space E^{\parallel} . Representative surfaces are shown as thick grey lines. (Top) Cut-and-project construction: vertices of the 2D grid with perpendicular coordinate inside the selection region depicted as a thick green segment in E^{\perp} are projected onto the parallel space to generate an ideal Fibonacci chain. (Middle) Sketch of fluctuations of the representative surface corresponding to a phason mode with a wavelength of about 7 tiles. Note that in this 1D Fibonacci example, such a fluctuation destroys long range quasiperiodic order. (Bottom) A shift of the origin in perpendicular space generates another ideal Fibonacci chain which differs from the top one by correlated tile flips corresponding to a phason mode of infinite wavelength. The infinite structures corresponding to the top and bottom constructions are indistinguishable (all n -points correlation functions equal).

obtained by taking α such that $\tan(\alpha) = 1/\tau$ and a selection region corresponding to the projection of the 2D square unit cell on E^\perp , *i.e.* a line segment of length $l = \cos(\alpha) + \sin(\alpha)$. This method, known as *cut-and-project*, can be generalised to efficiently generate quasicrystals with all kinds of symmetries in any dimension. As an alternative to the selection region, the same result can be obtained by instead decorating the square grid with line segments of length l , perpendicular to E^\parallel . The location of the particles is then obtained as the intersections of these *atomic surfaces* with E^\parallel .

Irrational numbers can be approximated by a sequence of rational numbers, using continued fractions for instance. Replacing the irrational ideal slope in the cut-and-project method by its rational approximations generates a sequence of periodic structures with larger and larger unit cells, whose local structure is very close to that of the quasicrystals. These periodic crystals are called *rational approximants* of the quasicrystal.

To study quasicrystals found in experiments or simulations, it is convenient to use the high-dimensional representation to walk our way “backwards” and *lift* the self-assembled structures to sets of points forming a *representative surface* in the higher dimensional space [30–32]. The representative surface of the Fibonacci chain is shown as thick grey lines in Figure 5. Real quasicrystals never correspond exactly to the ideal structure obtained by a cut-and-project construction. Instead, they exhibit a peculiar kind of disorder which can be understood as fluctuations of the representative surface in the perpendicular direction E^\perp around the average ideal one. These fluctuations can be decomposed into modes in Fourier space. In analogy with the phonons that correspond to modes of lattice fluctuations, modes of the representative surface fluctuations in the high-dimensional representation of quasicrystals are called *phasons*. A phason mode (of rather short wavelength) in the Fibonacci chain is sketched in Figure 5-middle. Analogous to phonon fluctuations (Mermin-Wagner theorem), the effect of phason fluctuations depends on the dimension of the system. In 1D systems, long range aperiodic order is destroyed by phason modes. In 2D, the order remains, but becomes only quasi-long-range in the presence of phasons: Bragg peaks broaden and their intensity decays as a power-law. In 3D systems, weak phason fluctuations cause additional diffuse scattering in the diffraction patterns of real quasicrystals but do not destroy the long range quasiperiodic order.

The phason modes correspond to extra degrees of freedom that are unique to quasicrystals. This appears clearly when realising that, in the cut-and-project construction, the origin of the cut in perpendicular space can be chosen freely. For a periodic structure, generated by a cut with a rational slope, shifting the origin of the cut simply translates the whole structure. This correspond to a trivial phonon mode of infinite wavelength. In the case of a quasicrystal however, a shift of the origin in perpendicular space generates a new structure that differs from the previous one by correlated local rearrangements of tiles all over the tiling. All quasicrystals obtained this way are equally valid and *indistinguishable* in the sense that all n -points correlation functions of their density fluctuations are the same [33, 34]. The correlated tile rearrangements caused by a shift of

the cut origin correspond to phason modes of infinite wavelength, and have no equivalent in periodic structures⁴. In the Fibonacci chain, tile rearrangements associated with the phasonic degree of freedom correspond to correlated local flips of L and S tiles as shown in Figure 5-bottom. These kind of local tile flips are possible in most quasicrystals and are sometimes confusingly referred to as “phason flips”. This terminology is misleading because phasons correspond to tiles rearrangements across the whole structure as a collective excitation. A tile flip is related to the phasons in the same way that a small displacement of a particle away from its ideal lattice site is related to phonons. The Fourier modes of the collective fluctuations of particles positions in E^{\parallel} and E^{\perp} give rise to phonons and phason respectively⁵ [35, 36]. As will be discussed briefly in Section III.5.3, phonon and phason dynamics are coupled in quasicrystals.

We end here the introduction of essential quasicrystal concepts. Additional crucial concepts are introduced later in the thesis, when needed. In Section II.3.3, we present the details of the lift procedure and introduce the essential concept of *perpendicular strain*. In Section II.3.5, we briefly discuss the growth of quasicrystals. Very good text books exist for the reader interested in the many other wonders of quasicrystals theory not directly used in this thesis [8, 9, 37].

.2 Soft quasicrystals

Before the turn of the 21th century, all known quasicrystals had been discovered in metallic alloys. In 2004, Zeng *et. al.* discovered a dodecagonal quasicrystal (12-fold symmetry) in a micellar system of dendrons [38]. This finding introduced quasicrystals in the realm of soft-matter physics, which deals with system whose basic constituents are much larger than atoms (nanoparticles, macromolecules, colloids...). The interaction between the basic constituents of soft-matter systems is typically weaker than the strong interactions holding atoms together in solids. Hence, the energy density and the elastic modulus of the assemblies are typically quite small, resulting in “soft” materials such as

⁴Consider a d -dimensional quasicrystal of rank D . It might be generated as the cut of a D -dimensional periodic structure by a hyperplane of dimension d . The hyperslope of this cut is can be written as a $(D-d) \times d$ matrix quantifying how much displacement in perp-space is caused by a displacement in parallel space, for each direction in both spaces. We will look at this in more detail for an octagonal 2D quasicrystal in Section II.3.3. Along some perp-space directions, this hyperslope might only contain rational elements. Then, no phason mode is associated to shifts of the origin in this direction which is called a *discrete dimension*. Hence, for a quasicrystal of rank D in dimension d , there are *at most* $D-d$ phason degrees of freedom (and at least one) [30].

⁵The adequacy of the term phason itself has been the matter of debates. Indeed, the *-on* suffix suggests a particle interpretation. However, in contrast to phonons, phason modes are evanescent and do not propagate. Moreover, it was observed that over the years, the term phason was gradually used more and more for anything related to the perpendicular subspace of the high-dimensional representation of quasicrystals, leading to much confusion. In this thesis, we try to follow the experts prescription discussed in References 35 and 36, and in particular, avoid using misleading terms such as “phason flip” and “phason strain”.

gels, pastes or liquid crystals⁶.

Soft quasicrystals quickly became a topic of active research. Indeed, the ordered nature of the quasicrystals combined with their unusual symmetries promise interesting optical properties [39–42], which manifest when the wavelength of the light is comparable to the typical distances in the material. In metallic quasicrystals, the relevant constituents are atoms, which interact mostly with X-rays. In order to harness the optical properties of quasicrystals at larger wavelengths, bigger building blocks, such as those found in soft matter systems, are required.

Even though quasicrystals exist in both metallic and soft matter systems, they differ quite a lot. In particular, while icosahedral symmetry is commonly observed in metallic quasicrystals [1, 17, 43–45], it has to date never been observed in soft-matter systems. Icosahedral quasicrystals are quasiperiodic in all 3 directions of space. Instead, soft quasicrystals discovered to date are only quasiperiodic in two dimensions, and stack periodically in the third one. In the quasicrystalline layers, the dodecagonal (12-fold) symmetry seems to be the most common one. The communities dealing with metallic and soft quasicrystals are also quite different. Researchers working on metallic quasicrystals typically have a strong background in crystallography and hard condensed matter. The soft matter community on the other hand is usually more familiar with statistical mechanics and self-assembly concepts. Of course, many bridges exist between the fields. Coming from the soft side of the barricade, this thesis adopts mainly the self-assembly perspective and tends to leave aside crystallographic aspects, both purposely and by ignorance.

Most soft quasicrystals to date have been observed in systems of micelles, with the micelles formed by very different building blocks. This includes the first soft quasicrystal, of symmetry 12, reported in a micellar system of dendrons [38]. Quasicrystals of symmetry 12 and 18 have later been reported formed of micelles made of block copolymers [46]. A dodecagonal quasicrystal has been found in a system of micelles turned into mesoporous silica [47] and in star polymer melts [48]. In diblock copolymer melts, a metastable dodecagonal quasicrystal has been found to be kinetically favoured upon fast cooling [49]. Aside from micelles, a dodecagonal quasicrystal has been observed in a binary mixture of nanoparticles self assembling at an interface [50].

Note that while icosahedral quasicrystals remain elusive in the bulk, large clusters with icosahedral symmetry have been stabilised by confining colloids in spherical droplets [51].

As can be seen from this survey of past experimental results, quasicrystalline order appears robustly in a striking variety of systems. The nature of the constituents (micelles or nanoparticles), as well as their chemistry (micelles of very different composition) seem rather unimportant as far as the quasiperiodic order is concerned. The size of the building blocks varies by almost two orders of magnitude between the silica micelles [47] (a few Angströms) and the star

⁶Daan Frenkel once defined soft matter as “stuff that does not get through airport security checks”.

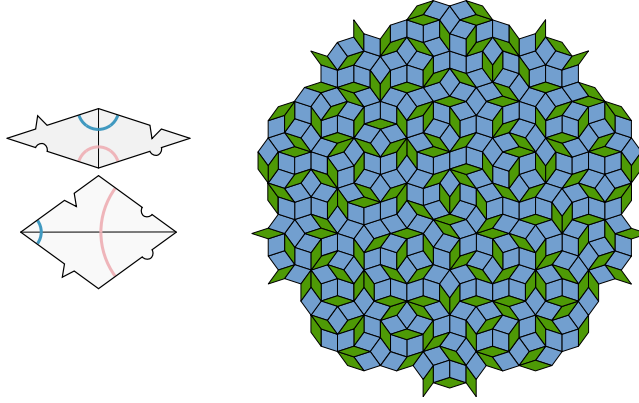


Figure 6: (Left) Penrose prototiles with matching rules enforcing ideal quasiperiodic order. To experience the frustrating fact that matching rules are not growing rules, the curious reader is encouraged to print many of those tiles and try making a large patch of ideal Penrose tiling. (Right) Random version of the Penrose tiling obtained by reshuffling tiles in the tiling of Figure 2. This tiling contains a very high number of violations of the matching rules depicted on the left.

polymers [48] (several tens of nanometers), yet they form similar quasicrystals. This suggests that, regardless of the microscopic details of the interactions, general mechanisms stabilise quasicrystals in soft-matter systems. This thesis is an attempt at contributing to unravelling these mechanisms.

.3 Quasicrystal stability

The question of the mechanisms stabilising quasicrystals was raised as soon as they were discovered in metallic alloys. Right after the publication of Shechtman’s puzzling diffraction pattern [1], Levine and Steinhardt rationalised the underlying structure with a three dimensional Penrose tiling, suggesting that this aperiodic structure might be the ground state of the system [14]. Soon after, in a reply to this paper, Elser commented that the constraints that must be satisfied to construct an ideal Penrose tiling are not compatible with a rapid growth process [52]. Hence, he suggested that the structure likely contained a high amount of peculiar defects, in the form of local tile flips (later recognised as phason fluctuations). Such fluctuations would only slightly broaden the diffraction peaks, and Shechtman’s data was not accurate enough to check for their presence. Over the course of four decades of active research, this question has remained open, and the two original approaches are referred to as the *energetic* or *entropic* stabilisation of quasicrystals.

The energetic point of view postulates that the interparticle interactions encode “matching rules” between the tiles, favoring an ideal quasicrystal. Match-

ing rules between adjacent tiles that enforce an ideal quasicrystal had previously already been discovered for several mathematical aperiodic tilings. For example, Figure 6-left shows the two prototiles of the Penrose tiling of Figure 2 decorated with notches and extrusions at the edges that limit their placement. The resulting matching rules then enforce ideal 10-fold quasiperiodic order. In the energetic picture of quasicrystal stability, matching rules violations then carry an energetic cost due to the particle interactions, and hence should anneal out towards an ideal tiling ground state. The resulting structures should have a minimum amount of phason disorder, and the diffraction pattern should be composed only of pure Bragg peaks. Note that in the rapid growth of a quasicrystal from the melt, matching rules violations inevitably get kinetically trapped, and annealing is likely to be slow. As a result, some perpendicular-space disorder is still expected in these systems.

In contrast, the entropic picture of quasicrystal stability ignores matching rules and considers instead random versions of the tilings. Indeed, in all tilings mentioned above, tiles can be reshuffled and reorganised in many different ways, while still covering the whole space without gaps or overlaps⁷. This defines a random tiling ensemble, in which the system can adopt many different discrete configurations. As an example, Figure 6-right shows one randomised version of the ideal Penrose tiling of Figure 2. The freedom of choosing a realisation from the random tiling ensemble brings an entropy contribution which is assumed to stabilise the quasicrystal at high temperatures, where tiles can easily rearrange to sample the random tiling ensemble. The high amount of disorder in perpendicular space in such structures adds diffuse scattering to the diffraction patterns. Note that in contrast to the energetic picture, this disorder is not expected to fully anneal out over time.

For the quasicrystals found in metallic alloys, four decades of discovery and many debates give a rather mixed picture. It seems that distinctive features of both scenarios are observed, depending on the system [35, 43]. To bolster the energetic picture, a few stable quasicrystals have been found which seem to exhibit little perpendicular space disorder and to remain stable down to low temperatures. In particular, after an epic quest of many years, involving systematic searches in mineralogy museums and expeditions in the Koryak Russian mountains, the first natural quasicrystal was found in a meteorite [45, 53, 54]. The quasicrystal is of high quality and exhibits a very high degree of order. Its stability on geological timescales (of the order of hundreds of million years) suggests that it might actually be stable at low temperatures, although metastability remains possible, as is the case for e.g. diamonds at room pressure. Yet, this suggests these structures might be stabilised by energetic matching rules encoded in the atomic interactions [17].

However, matching rules are not, in general, growing rules, in the sense that there are many ways of adding a new tile abiding by the matching rules to an already grown patch, but the majority of them will lead to inevitable

⁷Note that a random tiling model does not need a reference ideal tiling. Only a set a prototiles that allow random tiling of a space is required to define a random tiling ensemble [30].

gaps or overlaps later on. In practice, it is extremely hard to grow a patch of Penrose tiling by hand by following the matching rules shown in Figure 6-left with more than a few dozen of tiles, without creating defects [55]. Hence, a large amount of tile disorder (matching rule violations) is necessarily created during the fast growth of quasicrystals from the melt [52]. This suggests that energetic matching rules can only play a limited role in their formation, but leaves the door open to a two-step scenario: first, a highly disordered quasicrystal forms with many matching rule violations, which then anneals towards an energetic ground state with ideal quasicrystalline order [52, 56].

On the side of the entropic scenario, a very strong argument can be made based on the observation that most atomic quasicrystals are stable at high temperatures, where entropy favors perpendicular-space disorder, and where thermal motion allows an efficient sampling of the random tiling ensemble. They then loose stability to periodic approximants at low temperatures, when the magnitude of the entropic contribution of the random tiling is not sufficient to compete with the lower energy of the periodic ground state [30, 36, 57]. When this is the case, clearly the ground state of the system cannot be an ideal quasicrystal, and hence the energetic picture breaks down.

In the soft matter realm, owing to the larger size of the constituents, direct space images of the experimental systems organised in random tilings are often available, in addition to the diffraction patterns (see Figure 7)[48, 50, 58]. This observation bolsters the entropic scenario for the stability of soft quasicrystals. However, due to the much slower dynamics of soft-matter systems in comparison to atomic ones, it is possible this disorder is left over from the crystallisation kinetics. One way to test this would be to observe tile rearrangements in real-time and real-space, but colloidal systems where this is possible have thus far proven hard to achieve. Additionally, it should be noted that entropy naturally plays a significant role in soft-matter systems, and hence the appearance of quasicrystals in soft matter is in itself evidence that entropy may play an important role in their stabilisation. In fact, as we will show in this thesis, it is entirely possible to design numerical colloidal models that form quasicrystals purely stabilised by entropy.

.4 A brief note on theoretical treatments of quasicrystal stability

Various theoretical approaches have been used to tackle the stability of quasicrystals. Although we did not study them in depth, we mention the most important ones here as references for the interested reader.

Soon after the discovery of the first quasicrystals, a hydrodynamic theory was developed [30]. It predicts that phason modes in stable quasicrystals should relax with a characteristic time that increases (and diverges) with the wavelength. This relaxation process is associated to so-called *phason elastic constants* which drive the fluctuating representative surface of real quasicrystals towards the

ideal one. In the early days of quasicrystal research, significant efforts were invested into measuring these elastic constants from experiments and simulations [57, 59–63]. The hydrodynamic theory supports the entropic scenario as it predicts stable quasicrystals at high temperatures.

Mean-field, “à la Landau” approaches have also been attempted to elucidate the stability of quasicrystals. Following the discovery of quasicrystals in alloys, Mermin and Troian developed a simple Landau theory for systems of several components, which generated stable 2D decagonal and 3D icosahedral order [64, 65]. The discovery of soft quasicrystals in monodisperse systems motivated other Landau theories based on single component systems, but with more complex interaction potentials encoding two length scales [66]. This approach is mostly motivated by the energetic picture, and suggests that isotropic interaction potentials favouring quasiperiodic order can be designed by encoding two irrational length scales in the Fourier transform of the potential [67].

.5 Numerical simulations

Numerical simulations have been used extensively to study the self-assembly and stability of quasicrystals in many different models. Self-assembly simulations can be thought of as numerical experiments, on ideal systems. Indeed, one starts by preparing an initial state of specified parameters (composition, packing fraction...). Then the simulation is run and measurements are taken that provide raw data on which analysis can later be performed. Very much like in a lab experiment, the simulation provides direct access to the behaviour of the system without approximations. However, in contrast to most traditional experiments, the collected snapshots contain all the microscopic information about the system (position, velocity of every particle) which allows in-depth analysis. The price to pay is that the studied systems are usually very small (usually up to 10^8 particles, to be compared to 10^{23} in typical macroscopic samples), and simulated for very short lengths of time. Moreover, simulations only deal with model systems. This is both a strength and a limitation depending on the physicist’s ambitions. On the one hand, the model system never exists as-is in nature (for example, there is no such thing as a perfectly hard, perfectly spherical particle) and attempts at reproducing realistic interactions in complex systems typically result in incredibly complicated simulations that are extremely time-consuming, and still often fail to quantitatively match experimental results. On the other hand, numerical simulations are extremely valuable when used on simple systems, since one can strip a model down to a few key ingredients, and obtain the exact behaviour of this ideal system. If the phenomenon of interest persists, the minimal model provides precious insights into the underlying fundamental mechanisms.

Atomistic simulations using realistic interaction potentials have been used to study metallic quasicrystals. For instance, using potentials from density functional theory, simulations suggest that a dodecagonal quasicrystal should be stable in binary oxides of Ba-O and Ti-O [68]. Interestingly, a dodecagonal

quasicrystal has been reported in a simulation of a one-component system of tantalum [69]. Dodecagonal quasicrystals have also been reported in molecular dynamics simulations of compressed bilayers of water [70] and silicon [71].

Quasiperiodic order requires the interplay of several length scales. Hence, simpler numerical models for quasicrystals fall into two rough families. The length scales can either be obtained by mixing particles interacting with rather simple potentials, or by directly constructing a more complex interaction potential in one-component systems. Both approaches have been used to study quasicrystals in atomic and soft matter systems.

Decagonal (10-fold symmetric) and dodecagonal (12-fold symmetric) quasicrystals in 2D have been obtained very early in Monte Carlo simulations of Lennard-Jones binary mixtures [72, 73]. A dodecagonal quasicrystal was found to be stable at infinite pressure in 2D binary mixtures of hard disks [74], and at finite pressure in a binary mixture of disks with non-additive hard interactions [75]. Numerical density functional theory calculations of 3D binary mixtures of hard spheres have found only metastable ranges for icosahedral quasicrystal [76]. Inspired by the discovery of the first soft quasicrystals [38, 50], Iacovella *et al.* built a model system for hard particles with size polydispersity, grafted with ligands. Owing to the high computational cost of simulating explicit ligands, the study was limited to rather small systems, but self-assembly of quasicrystal approximants was observed nonetheless [77].

Several studies have reduced the number of components in the system to one, at the expense of some extra complexity in the interaction potential. Using an oscillating potential inspired by the Friedel oscillations that appear in the interaction of atoms in alloys, complex phases have been found to be stable including clathrates and icosahedral quasicrystals of very good quality [78]. Another family of oscillating potentials was found to stabilise icosahedral, dodecagonal, decagonal and octagonal quasicrystals [79]. In a remarkable study of systems interacting via a Lennard-Jones-Gauss potential, Kiselev *et al.* reported the existence of a stable decagonal quasicrystal, for which they could disentangle the free-energy contributions of the phononic and phasonic degrees of freedom [63]. An interesting dodecagonal quasicrystal based on a Moiré pattern of hexagonal layers rotated by $\pi/6$ was found in simulations of particles with a hard core, short range attraction and long range repulsion [80].

The experimental observation of quasicrystals in polymer systems motivated numerical studies of soft core particles, which can overlap for a finite energy cost. Density functional theory and Brownian dynamics simulations of systems interacting with such soft core potential with two length scales revealed a metastable dodecagonal quasicrystal phase [81]. Self-assembly of dodecagonal and octagonal quasicrystals was reported in Monte Carlo simulations of purely repulsive soft core particles interacting via a generalised Hertzian potential [82, 83]. Adding an attractive range and repulsive tail to soft core particles allowed self-assembly of quasicrystals of symmetry 12 and 18 [84]. Free-energy calculations for systems of tetrablock copolymers showed that a metastable dodecagonal quasicrystal could form [85].

Great progress in the numerical study of soft quasicrystals has been achieved

by simulations of particles with a hard core and a repulsive square shoulder at short distances [86]. These systems model hard colloidal particles surrounded by a soft corona of ligands. In two dimensions, Monte Carlo simulations have shown that careful choice of the core-to-corona ratio can lead to the self-assembly of quasicrystals of symmetry 6 [22], 10, 12, 18 and even 24 [87]. Free-energy calculations have confirmed that the dodecagonal quasicrystal is indeed thermodynamically stable for a range of temperatures [88]. Smooth versions of the square shoulder potential have been shown to form a decagonal quasicrystal [89] in 3D, and quasicrystals of symmetry 10, 12, 18 and 24 in 2D [90]. These simulations contain only one type of particles which nonetheless interact via a remarkably simple potential. They show that, indeed, two carefully chosen length scales in a one component system are sufficient ingredients for quasiperiodic order to emerge. In this thesis, we aim at obtaining a similar minimal system with the mixture approach.

Keeping the interaction simple (hard repulsion), some studies have tried encoding the different length scales in the shape of the particles instead. Self-assembly of a dodecagonal quasicrystal has been reported in Monte Carlo simulations of hard tetrahedra [91, 92], and approximants have been observed in hard rounded tetrahedra [93]. Interestingly, since the interactions are hard in these systems, the energy plays no role in the equilibrium properties and entropy is the only drive for self-assembly.

Finally, several studies have explored the possibility of replacing length scale constraints by bond orientations, in systems of particles with patches on the surface, that encode preferential bonding directions. In two dimensions, disks with 5 or 7 patches have been found to form dodecagonal quasicrystals [94–96]. Octagonal and decagonal quasicrystals have been observed for very narrow patches [97]. In three dimensions, patchy particles can self-assemble in dodecagonal [98] and icosahedral [99] quasicrystals. Colloidal patchy particle systems could be experimentally realised with DNA origami [100], although to date, no quasicrystal was observed in these systems.

.6 A minimal model for quasicrystal self-assembly

.6.1 Motivations

While quasicrystals have been experimentally observed in several very different soft matter systems, these discoveries are mostly serendipitous. Designing an experimental system targeted for quasicrystal self-assembly remains a challenge. Yet, a simple colloidal system that robustly and reliably self-assembles into quasicrystals is highly desirable as it would allow direct real-space and real-time access to quasicrystal dynamics on the micron scale. Such an experimental platform would be extremely valuable to tackle many open questions pertaining to the nucleation and growth of quasicrystals, or the dynamics of their peculiar defects for example. The wealth of numerical simulations have explored the possibility of quasicrystal self-assembly in many models, but most of them

remain rather hard to realise in experiments. The remarkable studies of the hard-core-square-shoulder potential have established that quasicrystalline order can emerge in quite general settings from carefully chosen interplaying length scales, built into a single potential. Although the hard-core-square-shoulder model might be a good approximation of a hard colloid grafted with a soft corona of ligands, it is still very hard to control the corona interaction in experiments: ligands interact in complex ways and in the dense systems used for self-assembly, coronas deform giving rise to many-body interactions that are hard to control [101, 102].

In contrast, purely hard colloids can nowadays be easily produced with impressive control on their size [103–105]. They are extremely well approximated by purely hard spheres, to the point where hard-sphere simulations and experiments match quantitatively in extended regimes [106, 107]. Motivated by this experimental possibility and following the work of Likos and Henley that showed the existence of a stable dodecagonal quasicrystal in binary mixtures of hard disks at infinite pressure [74], our work takes a closer look at quasicrystal self-assembly in binary mixtures of hard spheres. Since all soft quasicrystals observed in experiments to date exhibit quasiperiodic order in two dimensions, and periodically stack in the third dimension, we focus on a two-dimensional model and assume that the binary mixture of hard spheres is confined at an interface.

This geometry is similar to the one used by Talapin *et. al.*, who reported a dodecagonal quasicrystal in binary mixtures of nanoparticles (see Figure 7).

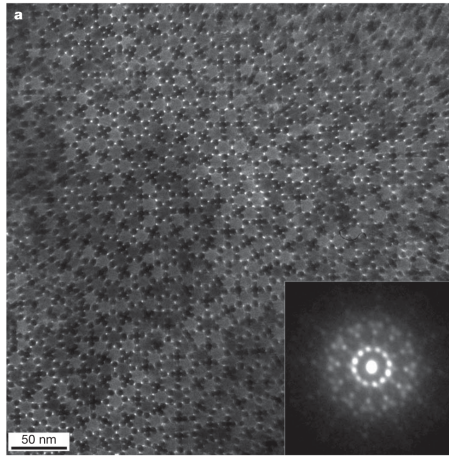


Figure 7: Dodecagonal quasicrystal obtained in binary nanoparticle mixtures self-assembled at an interface. The 12-fold symmetry is shown in the diffraction pattern in inset. Taken from Ref. 50.

.6.2 Non-additive hard disks mixtures

A binary mixture of hard spheres confined at an interface can be mapped onto an equivalent 2D system of hard disks by looking at the projection of the system in the interface plane, as sketched in Figure 8. In general, particles made of different materials will have different wetting properties with the fluid interface, and hence will rest at different heights (see Figure 8-right). Then, in the 3D configuration, a small sphere can slide under (or above) a large one before contact is made. This translates in the equivalent 2D model by having a contact distance for large and small disks smaller than the sum of their radii. Spheres

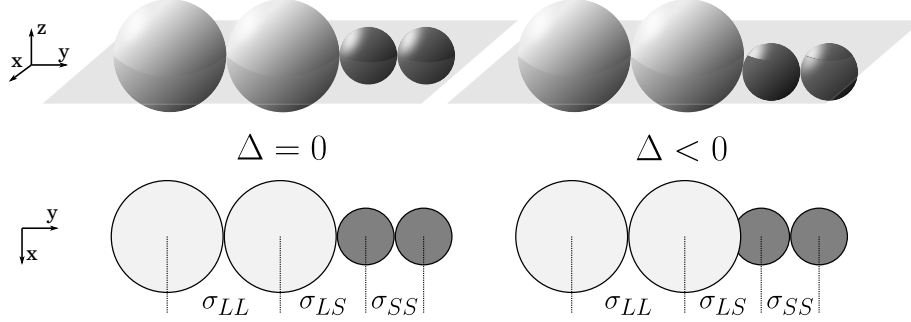


Figure 8: Binary mixtures of 3D hard spheres confined at an interface (top) can be described by an equivalent 2D mixture of hard disks, when looking at the projection of the spheres on the interface plane (bottom). If particles of different types rest at different heights with respect to the interface, due to different wetting angles with the fluids, the contact distance between the equivalent small and large disks becomes smaller than the sum of the spheres radii and the resulting system is a *non-additive* hard disk mixture.

of one type all sit at the same level, and hence behave as standard hard disks in the 2D equivalent system. In this very simple model, we ignore the interactions that may result from deformations of the interface. The resulting 2D model is called a *non-additive* hard disk mixture and it will be our companion for the rest of this thesis.

A non-additive hard disk mixture containing large disks of diameter σ_{LL} and small disks of diameter σ_{SS} is characterised, in the thermodynamic limit, by only two parameters:

- the size ratio of large and small disks $q = \sigma_{SS}/\sigma_{LL}$
- the composition of the mixture, which we parametrise by the number fraction of small disks $x_S = N_S/(N_L + N_S)$, with N_L and N_S the number of large and small disks respectively.

The interaction potentials between two disks u_{ij} ($i, j = L$ or S for large and small disks respectively) a distance r apart, is given by

$$u_{ij}(r) = \begin{cases} \infty & \text{if } r < \sigma_{ij} \\ 0 & \text{otherwise.} \end{cases} \quad (2)$$

Here, σ_{LS} is the contact distance for large and small disks.

$$\sigma_{LS} = \sigma_{SL} = (1 + \Delta) \frac{\sigma_S + \sigma_L}{2}, \quad (3)$$

where Δ is the so-called *non-additivity parameter*. When $\Delta = 0$, the model is called *additive* and the disks behave like standard hard disks that cannot

overlap. The 3D situation of spheres at an interface corresponds to negative non-additivity, *i.e.* $\Delta < 0$. If the floating levels of the two species are offset by a distance z , the non-additivity parameter is given by $\Delta = 1 - \sqrt{1 - 4z^2/(\sigma_{SS} + \sigma_{LL})^2}$.

While self-assembly at an interface is a common geometry in soft matter (see, *e.g.* [108–113]) other sources of non-additivity can be readily present in real-world self-assembling systems. Particles that interact via softer interactions (due to charge, dipolar interactions, ligand coatings, etc.), may, depending on the overall packing fraction, favour configurations where the favoured distance between different pairs of particles behaves non-additively. Non-additive interactions have been shown to significantly impact the phase behaviour of mixtures of particles [114–118], and hence are likely to be an important factor in predicting the self-assembly of hard-disk mixtures.

.7 Outline

The phase behaviour of binary mixtures of binary (additive) hard disks at infinite pressure has been studied by Likos and Henley in the 90's [74]. They showed that even at infinite pressure, such mixtures can form a dodecagonal quasicrystalline phase, and suggested non-additivity as a natural extension of their work. In the first chapter of this thesis, we follow their tracks and explore the infinite pressure phase behaviour of non-additive hard-disk mixtures. Improving the sampling of candidate phases allows us to find new stable phases that were not considered earlier and we show that non-additivity indeed promotes quasicrystal stability.

In the second chapter, we relax the infinite pressure constraint and perform direct self-assembly simulations at finite pressure. This study confirms that the dodecagonal quasicrystal predicted at infinite pressure can self-assemble under realistic conditions. We also report the self-assembly of a new octagonal quasicrystal with interesting properties.

In the third chapter, we take a deeper look at the stability of the self-assembled dodecagonal quasicrystal by performing numerical free-energy calculations. This allows us to draw an essentially exact phase diagram for our system, and to prove that the dodecagonal quasicrystal is thermodynamically stable. Using accurate free-energy calculations, we quantitatively assess the validity of the random tiling hypothesis for our system, that we use before on several occasions.

Chapter I

Infinite pressure

In the final discussion of a paper published 1993, Likos and Henley suggested that non-additivity in hard disks mixtures could help stabilising quasicrystals by providing finer control over the length scales involved in the system [74]. In this Chapter, we explore this hypothesis in detail, and demonstrate that this intuition was indeed very fruitful.

We start our investigation by reproducing their results and look at the infinite pressure phase behaviour of additive hard disks. In this study, one challenge is to identify the best packing structures, as well as their optimal deformations when the size ratio of the disks is varied. Using a method based on Monte Carlo simulations, we improve the sampling of candidate crystal structures. This allows us to find several new crystal structures that, for specific size ratios, improve on the optimal packings proposed by Likos and Henley. In addition, we identify three new random tiling quasicrystals stable in the infinite pressure limit.

We then extend the analysis to binary mixtures of non-additive hard disks and show that indeed, non-additivity enhances the stability region of the main square-triangle random tiling quasicrystal.

I.1 A packing problem

Consider a binary mixture of hard disks containing N particles with a number fraction of small disks x_S . At fixed pressure p and temperature T , we wish to find the stable crystal structures. The stable phase is the one that minimises the (Gibbs) free-energy $G = U - TS + pV$ with U the internal potential energy of the system, S its entropy, and V its volume. Since we consider hard interactions, all accessible configurations contain no overlaps and hence have zero potential energy. The kinetic energy is linked to the temperature in a trivial way. Hence $U = 0$. Moreover in the infinite pressure limit, the term pV dominates the

term TS , which can therefore be neglected¹. As a result, in the limit of infinite pressures,

$$\frac{\beta G}{N} = \beta p \frac{V}{N} = \beta p v \quad (\text{I.1})$$

Hence, the stable arrangement of disks minimises the volume per particle v , *i.e.* achieves the most efficient packing for a given size ratio q , non-additivity parameter Δ and mixture composition x_S . Such arrangement might be a single homogeneous phase, or a coexistence of two different structures.

For $\Delta = 0$, finding the stable arrangement at infinite pressure reduces to the long standing mathematical problem of optimal disk packing in the 2D plane. In a system containing only one type of disks, Lagrange proved in 1773 that the hexagonal close packing realise the highest density of all periodic arrangements. A proof in full generality (not restricted to periodic arrangements) was given by Tóth in 1942 [119].

With binary mixtures, the problem of proving the best packing arrangements is still open, and the topic of active research. Beyond a size ratio $q \approx 0.74$, it is proven that no arrangement packs better than a phase separation of hexagonal close packings of large disks on the one hand, and small disks on the other hand [120]. For 9 specific size ratios, it is possible to construct so-called compact packings, whose contact graph contains only triangles. These packings have been proven to realise the highest possible density at their specific size ratios. [121, 122]. Figure I.1 reproduced from Reference [123] summarises state of the art upper and lower bounds on the maximum packing fraction $\phi = \pi(N_L\sigma_L^2 + N_S\sigma_S^2)/4V$ (*i.e.* area fraction covered by the disks) as a function of size ratio. Note that the composition of the structures realising the best packing in Figure I.1 are not constrained. In this Chapter, we explore the best packing structures for a wide range of fixed size ratios *and* compositions.

Instead of trying to prove optimal packings rigorously here, we will employ numerical simulations to sample dense candidates structures, and build a phase diagram from there.

I.2 Phase diagram construction

To construct a phase diagram, we first need to know the phases that compete for stability, *i.e.* candidate packings of disks with a given size ratio q , non-additivity Δ and composition x_S . Once the candidate structures are known, a graphical method called *common tangent construction* is used to build the infinite-pressure phase diagram.

I.2.1 Obtaining candidate crystal structures

In their pioneering work [74], Likos and Henley explicitly constructed dense candidate structures phase using clever heuristics. However, it is extremely

¹This term can no longer be neglected in the free-energy difference of two phases that pack equally well in the infinite pressure limit. This case is addressed in section I.3.1.

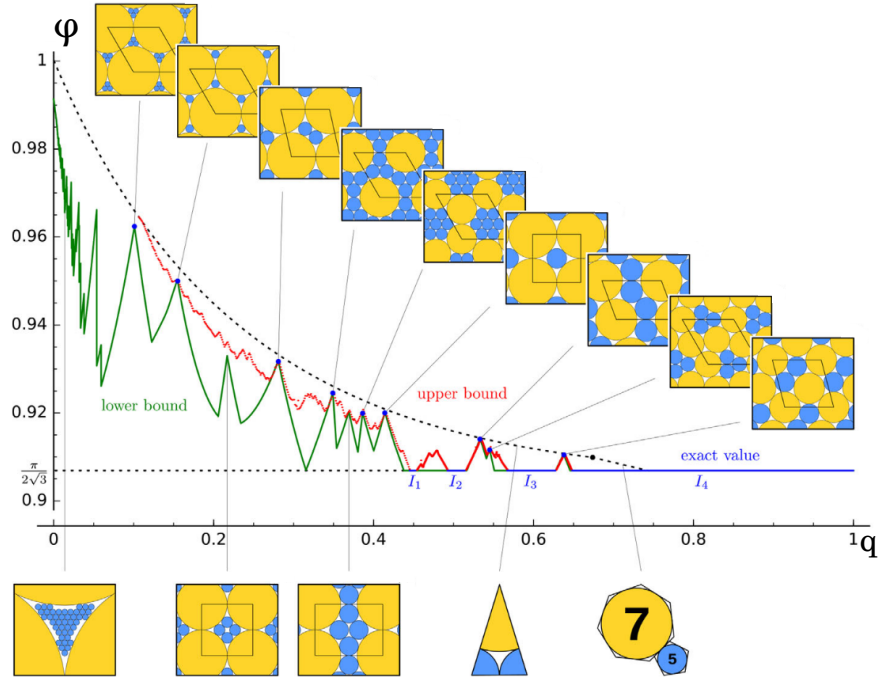


Figure I.1: Summary of the upper (red line) and lower (green line) bounds on the maximal packing fraction ϕ for binary mixtures of hard disks at size ratio q . The 9 blue points correspond to the magic ratios at which compact packings, depicted in the above squares, realise the proven maximum density. Blue line segments highlight size ratios intervals for which no arrangement of disks can pack better than a phase separation of hexagonal close packings of large and small disks. Courtesy of T. Fernique, taken from [123] with the kind authorisation of the author.

hard, and in fact essentially impossible, to make sure that all relevant structures have been considered.

In order to generate candidate crystal structures more systematically, we use the so-called *Floppy-Box Monte Carlo* simulation method [124, 125]. In this method, we simulate a small number of particles (up to 12) in a periodic unit cell and slowly compress them until a dense packing is reached. To accommodate all unit-cell shapes, Monte Carlo moves are included which deform the (rhomboidal) simulation box. At the end of the simulation, a quench to infinite pressure is performed to freeze the configuration, which is then taken as a candidate structure. The implementation of the algorithm is thoroughly described in Reference 125.

In our simulations, we considered all possible compositions with up to 12 disks in the simulation box and at least one large and one small disk. For larger numbers of particles, the method becomes less reliable, as the number of possible arrangements increases very rapidly with the number of particles and the systems tend to get kinetically arrested in jammed, rather low density arrangements. Nonetheless, even if it cannot guarantee that all relevant structures have been found, the Floppy-Box method has proven to be effective for systematically finding unit-cells of complex crystal structures in a large variety of systems [125–132], as long as the unit cell is not too large. Since the number of particles in the box is small, simulations are fast, allowing us to produce at least 50 candidate structures for each composition and size ratio we investigated. The most efficiently packed crystal structures are typically found multiple times in these 50 independent runs.

After the quench to infinite pressure, the systems are jammed and particles cannot move because they are trapped by their neighbours, or rattle in the cage of formed by their fixed neighbours. Since the quench is performed at a finite rate, the particles jam in locations that are close to, but not necessarily exactly the ones that realise the best packing. Therefore, in a second step, we individually look at all dense candidates, and construct for each of them a corresponding ideal structure, based on the contacts between pairs of particles.

Using this procedure, in the additive case, we recover all the structures that were previously considered by Likos and Henley [74] with their explicit construction method. In addition, the Floppy-Box simulations identified new crystal candidates that were not considered earlier. Structures relevant to the phase diagram in the additive case are summarised in Figure I.2. Each structure is named according to the same scheme as the one used in Ref. 74, extended where necessary. The new structures S3 and S4 have a rhombic unit cell containing 5 and 7 small particles respectively. The structure that we call Sh1 contains 3 small and 3 large disks in its unit cell, arranged in a shield motif.

The phases drawn in Figure I.2 depict the structures at “magic ratios” where they are highly symmetric, with a large number of contacts between the disks. When the size ratio q deviates from those values, the structures are deformed and the bond network as well as the overall symmetry change. Just like guessing and explicitly constructing all relevant dense candidate structures is hard, finding the optimal deformations as the small particles are inflated or shrunk is very

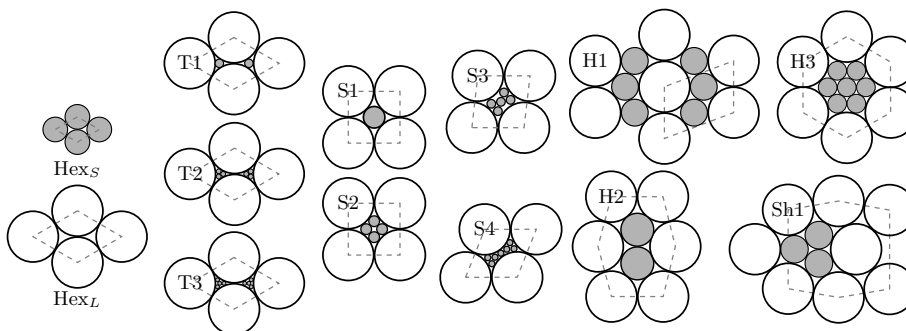


Figure I.2: Stable structures that appear in the additive phase diagram. The structures are shown at their respective “magic ratios”. Dashed grey lines outline the repeating unit of each lattice. The Sh1, S3 and S4 phases were identified in the output of Floppy-Box simulations and were not considered in earlier works. Complete deformation paths are reported in the Appendix A.

challenging. Luckily, here again, Floppy-Box simulations turn out to be of great help. By looking at the structures produced by the simulations slightly off the magic ratios, we can identify the preferred deformation paths and use them to construct ideal structures for all size ratios in-between magic ratios.

In Appendix A, we report the magic ratios for the identified structures and present the deformation paths for the phases that appear in the phase diagrams. Using Floppy-Box simulations to identify deformation paths allowed discovery of transformations with higher densities than those previously known.

Guided by Floppy-Box simulations, we identify ideal deformations and compute analytically the volume per particle of the phases along the deformation paths. As the number of particles in the unit cell increases, the complexity of the analytical expressions for the position of each particle, as a function of size ratio q and non-additivity Δ quickly becomes overwhelming. Thus once a set of constraints (particles contacts and symmetries) for an ideal structure is identified from the Floppy-Box outputs, we resort to **sympy** [133], a Python symbolic computation package to obtain the analytical expressions. Details on this procedure can be found in Appendix A.4.

At the end of this process, we obtain analytical expressions for the volume per particle of each of the candidate structures as a function of q and Δ , albeit typically highly cumbersome ones! We then use them to construct the infinite pressure phase diagram.

I.2.2 Common tangent construction

Equipped with a set of candidate structures, we use a graphical approach analogous to a *common tangent construction* to determine the relative stability of the corresponding phases.

For a given size ratio q , we plot each obtained candidate structure as a point

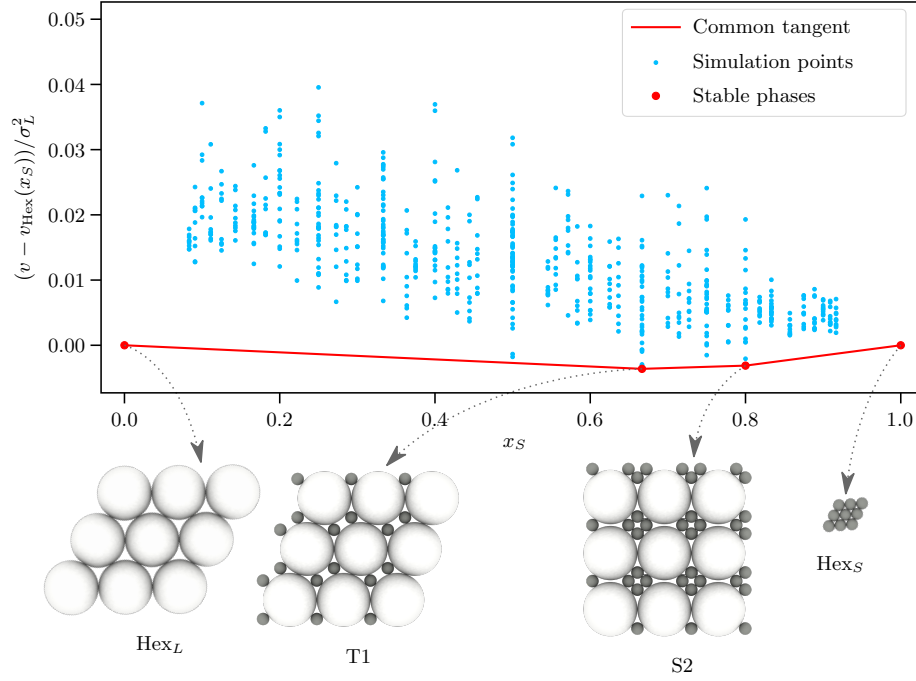


Figure I.3: Common tangent construction at size ratio $q = 0.23$. For clarity, the volume per particle of the coexisting hexagonal phases $v_{\text{Hex}}(x_S) = x_S v_{\text{Hex}_S} + (1 - x_S) v_{\text{Hex}_L}$ has been subtracted on the vertical axis. Blue dots represent candidate crystal structures found by 50 Floppy-Box simulations for each of the 66 compositions $LiSj$ with $i, j \geq 1$ and $i + j \leq 12$. Red dots correspond to stable ideal crystals and arrows point to snapshots of the Floppy-Box output (unit cells are repeated 9 times). The red line indicates, for all intermediate fraction of small disks, the volume per particle of the stable coexistence.

in the $(x_S - v)$ -plane, where v is the volume per particle of the structure. At any x_S , the stable state is the crystal phase, or coexistence of two crystal phases², which has the lowest volume per particle. For a coexistence of two phases α and β , involving a fraction n_α and $n_\beta = 1 - n_\alpha$ of all particles respectively, the overall fraction of small disks is $x_S = n_\alpha x_{S,\alpha} + n_\beta x_{S,\beta}$. The volume per particle v of the coexistence is also linear in the number fraction of particles involved in each of the phases. Therefore, in the $(x_S - v)$ -plane, points corresponding to pure crystal phases can be joined by straight lines which give the volume per particle of their coexistences.

Then, finding the set of stable phases for a given size ratio, reduces to a graphical common tangent construction as illustrated in Figure I.3 for $q = 0.23$. For monodisperse disks, the best packing is proven to be the hexagonal close packing [119], so at $x_S = 0$ and $x_S = 1$ the stable phase is a hexagonal packing of large and small disks respectively. For $x_S = 2/3$, the T1 phase achieves the best packing. The straight line that joins T1 and Hex_L points gives the volume per particle of their coexistence for all compositions $x_S \in]0, 2/3[$. This coexistence is stable because no point or other line joining two points is found below it. As x_S is increased, S2 is found to be stable for $x_S = 4/5$. S2 coexists with T1 for $x_S \in]2/3, 4/5[$, and with Hex_S for $x_S \in]4/5, 1[$. For clarity, the volume per particle of the coexisting hexagonal phases $v_{\text{Hex}}(x_S) = x_S v_{\text{Hex}_S} + (1 - x_S) v_{\text{Hex}_L}$ has been subtracted on the vertical axis of Figure I.3.

By repeating this construction on a grid of q , the approximate size ratio of phase boundaries can be determined for the composition of each crystal phase. Finally, the exact location of the phase boundary is obtained by numerical root finding for the two competing phases or coexistence, using the analytical expressions for the volume per particle of each phase. This allows us to construct the *exact* infinite-pressure phase diagram of binary hard disk mixtures, provided that all relevant candidate structures have been included.

I.3 Infinite pressure phase diagram of hard disks mixtures

We performed the analysis outlined above for additive hard disks with size ratios between 0.05 and 1, with a step size of 0.01. The best packed structures at each size ratio and composition are summarised in the infinite-pressure phase diagram shown in Figure I.4.

Horizontal lines correspond to the stability ranges of pure crystal phases, which only exist at one fixed composition each. Points outside of those line correspond to coexistence regions of the two phases that lie directly above and below the point (q, x_S) . We have only investigated size ratios $q \geq 0.05$, and compositions below $x_S \leq 11/12 \simeq 0.917$. This likely leads to some missed

²The existence of stable 2-phases coexistences at infinite pressure for our binary mixtures is clear from the geometrical argument described here. It can also be understood on more thermodynamic grounds from the Gibbs rule, as discussed in section III.1.1.

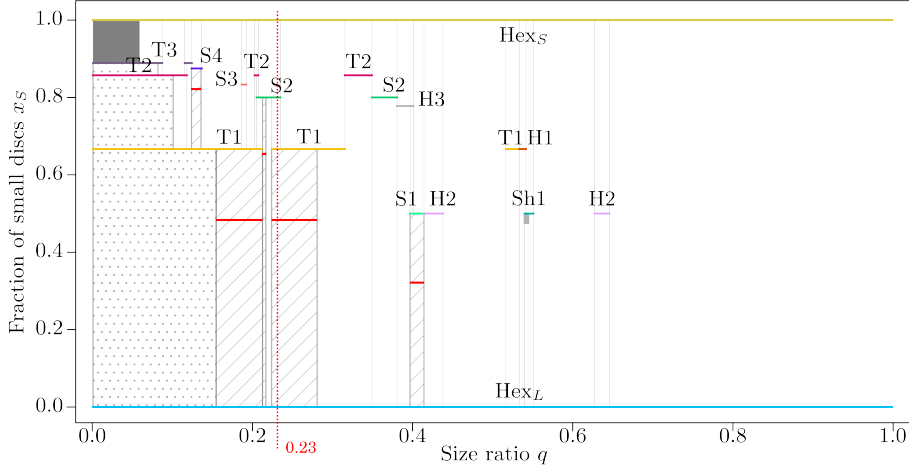


Figure I.4: Infinite pressure phase diagram of binary additive hard-disk mixtures. Horizontal lines represent stability ranges of pure crystal phases. For state points outside of those lines, the stable phase is a coexistence of the two pure crystal phases that lie immediately above and below the point. The vertical dotted line at $q = 0.23$ corresponds to the common tangent construction presented in Figure I.3. The upper left corner of the phase diagram (dark rectangle) was excluded from the analysis. The grey rectangle under Sh1 corresponds to a region where an infinite family of periodic structures is found, with the same volume per particle as the Sh1- Hex_L coexistence. Dotted and hashed rectangles depict random lattice gas and random tiling regions respectively. In the latter, the horizontal red lines highlight random-tiling quasicrystals. Their compositions are $\sqrt{3}/(2+2\sqrt{3}) \approx 0.317$, $2\sqrt{3}/(2+3\sqrt{3}) \approx 0.481$, $4\sqrt{3}/(2+5\sqrt{3}) \approx 0.650$ and $(4+7\sqrt{3})/(6+8\sqrt{3}) \approx 0.812$ for S1- Hex_L , T1- Hex_L , S2- Hex_L and S4-T1 random tiling quasicrystal respectively.

structures in the top left corner of the phase diagram. In this regime, we expect that the phase diagram gets more and more complicated for more extreme size ratios and large fractions of small disks [134]. Moreover, exploring this is computationally expensive (due to large unit cells), and not necessarily likely to include interesting results. As such, we have avoided this regime of the phase diagram.

The dotted vertical line at $q = 0.23$ corresponds to the common tangent construction illustrated in Figure I.3. Going from $x_S = 0$ to $x_S = 1$, we indeed find stable Hex_L, S1, T1 and Hex_S, with coexistences in-between.

As expected [120], no stable phase other than the coexistence of two hexagonal compact packing is found for size ratios above 0.74. For smaller size ratios, a wealth of crystal structures are obtained. The main features of Likos and Henley's phase diagram [74] are reproduced, but new stable phases (S3, S4, Sh1) are found among the candidates generated by Floppy-Box simulations.

I.3.1 Special regions

In some regions of the phase diagram, several distinct arrangements of disks can be found that pack equally well. In those cases, one needs to go beyond the simple expression given in equation I.1 to understand the equilibrium behaviour of the system. Indeed, in the free-energy difference between two competing packings with the same volume per particle in the infinite pressure limit, the pv terms cancel and the previously neglected entropy difference term $T\Delta S$ dictates the stability.

Two sources of entropy must be taken into account. First, at finite pressures, particles vibrate around their equilibrium lattice site which provides a *vibrational entropy* difference term ΔS_{vib} . In the limit of infinite pressure, this vibrational entropy difference tends to a value $\Delta S_{\text{vib}}^\infty$ which is a-priori non-zero³. For instance, 3D hard spheres can be packed with the same density in either face-centred-cubic (FCC) or hexagonal-close-packed (HCP) structures. Yet, there is a small but finite entropy difference of about $10^{-3} k_B$ per particle in the infinite pressure limit, making the FCC structure slightly more stable than HCP [135, 136]. In addition, in some structures, choices can be made for the arrangement of some sub-units (*e.g.* particle clusters). This brings a *configurational entropy* contribution ΔS_{conf} to the global free-energy difference. Overall, the free-energy difference between two competing disk arrangements which pack equally well in the infinite pressure limit reads

$$\Delta G = -T\Delta S_{\text{vib}}^\infty - T\Delta S_{\text{conf}} \quad (\text{I.2})$$

At – not in the limit of – infinite pressure, all particles are strictly immobile or rattling in a fixed cage. Then, the only contribution to $\Delta S_{\text{vib}}^\infty$ comes for the

³The vibrational entropy of the individual phases diverge in the infinite pressure limit, but their difference remains finite. At infinite pressure, particles are strictly immobile, the phase space contains a single microstate and the entropy is strictly 0. The divergence stems from the inappropriate classical counting of microstates in a regime where a discrete quantum treatment would be necessary.

rattling particles, which should be extremely small given the tiny size of the rattler's cages. Therefore, at infinite pressure, we neglect the vibrational entropy. In our system, the configurational entropy stemming from the competition of disks arrangement that pack equally well gives rise to several regions of peculiar equilibrium properties.

The repeating unit of the Sh1 lattice can be decomposed into a shield tile (hence the Sh label), containing the 3 small disks, and 2 Hex_L triangular tiles, as shown in Figure I.5. As long as the size ratio is smaller than a magic ratio for which the deformed shield loses contacts between large disks, shields can be combined with Hex_L triangles without volume-per-particle cost. Periodic structures can be constructed, that have the same volume per particle as the Sh1- Hex_L coexistence [137]. Examples of such structures are shown in the Appendix A.3. As far as packing is concerned, these phases are all equally stable as the coexistence between Sh1 and Hex_L at infinite pressure. However, it is likely that vibrational entropy $\Delta S_{\text{vib}}^\infty$ breaks this stalemate in favour of one specific crystal structure. We make no strong claims about the exact phase to be expected in this region (the very small area shaded grey in Figure I.4), except that it will consist of shields and triangles.

At small size ratios, large disks form a hexagonal compact packing (Hex_L) whose interstices can host small disks. The T1, T2 and T3 phases all consist of this same hexagonal packing, in which *all* interstices are filled with 1, 3 and 4 particles respectively. In principle, more of these types of structures exist with more small particles in each hole [134], but we have not investigated such extremely asymmetric size ratios and compositions.

Where these phases coexist, it is often possible to randomly fill the interstices with a fluctuating number of particles, such that the overall composition requirement is satisfied. As this random distribution is entropically favoured, such a homogeneous *random lattice gas* state is expected to be stable over a purely phase separated regime [74]. Figure I.6 illustrates a lattice gas formed by the coexistence of the T1 and T2 phases. We indicate lattice gases as dotted regions in the phase diagram. Note that when the size ratio becomes too large to accommodate the small particles without deforming the hexagonal lattice, this lattice gas phase is no longer optimal in terms of packing and loses stability. This can be seen on the right edge of the lattice gas regions connecting T1 and T2, or T2 and T3.

Usually, creating a boundary between two coexisting phases carries a volume cost. This normally limits mixing of phases in the infinite pressure limit. Indeed,

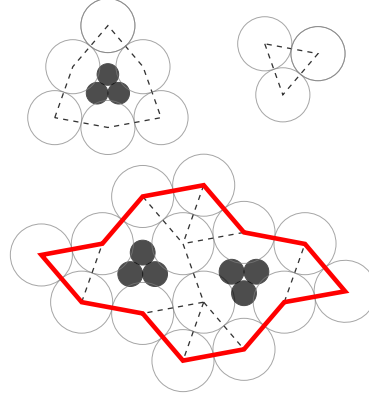


Figure I.5: The Sh structure is formed of shield (upper left) and triangle (upper right) tiles which can be combined into larger unit cells (bottom).

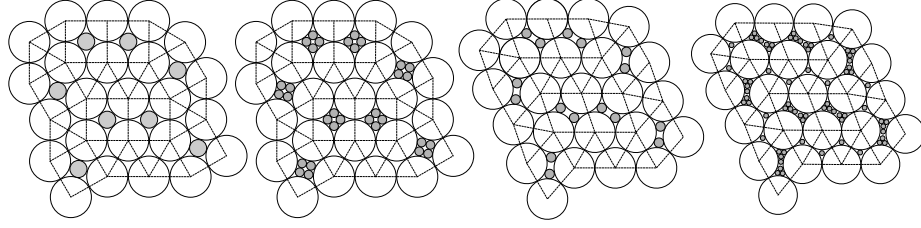


Figure I.7: S1 or S2 squares and Hex_L triangles can be joined without volume-per-particle cost. Moreover, squares and triangles tile the plane, so S1- Hex_L and S2- Hex_L coexistences result in a square-triangle random tiling (left). Random tilings can also be obtained by mixing rhombi with triangles (see for example T1- Hex_L and S4-T1 random tilings (right)).

in order for the boundary cost to vanish in the thermodynamic limit, phase boundaries must remain 1D objects in a 2D system, hence resulting in a true phase separation.

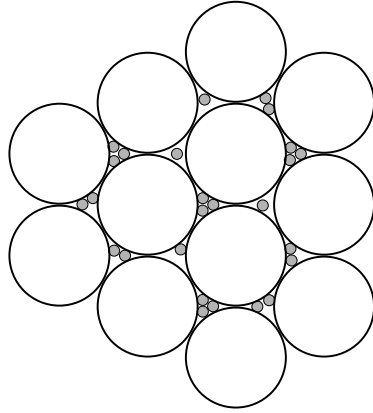


Figure I.6: Coexistences of T1 and T2 can form a lattice gas, where the interstices of a hexagonal lattice of large particles or randomly filled with 1, 2 or 3 small particles.

equally well, however the former has a finite configurational entropy per disk [61, 62, 138]. Moreover, previous results for 3D hard spheres [135, 136], as well as numerical evidence for non-additive hard disks presented in Chapter III of this thesis, suggest that the vibrational entropy contribution is much smaller than the configurational entropy contribution at large pressures. Therefore, wherever possible, random tiling regions, depicted as hashed rectangles in the

However, some structures have matching unit-cell edges, and can be stitched together without a volume cost. If, moreover, the structural motifs of the two phases together can tile the plane without gaps or overlaps, the two phases in coexistence can dissolve into one another and form a *random tiling* phase. For example, as illustrated in Figure I.7, there is no volume-per-particle cost for creating a boundary between S1 squares and Hex_L equilateral triangles (half a Hex_L unit cell). In addition, one can tile the plane with squares and equilateral triangles. Hence a random tiling of squares and triangles is possible. Likewise, it is possible to construct random tilings of rhombi and equilateral triangles. In fact, square-triangle random tilings can be continuously deformed into rhombus-triangle random tilings. For example, all random tiling pieces displayed in Fig. I.7 are isomorphic.

Random tiling and fully phase separated mixtures at the same composition x_S pack

phase diagram, should be preferred, on thermodynamic grounds, compared with phase separated coexistences at infinite pressure.

I.4 Random tiling quasicrystals

Because Floppy-Box Monte Carlo simulations use periodic boundary conditions to simulate crystal unit-cells, they are unable to directly provide quasicrystalline candidate phase, which, by definition, have no such thing as a unit-cell. However, quasicrystals can be found, hidden in the random tiling regions.

A random tiling is an ensemble of tilings that cover a space with a set of tiles, without gaps or overlaps. In the square-triangle random tiling of the 2D plane, as the proportion of small disks x_S varies, the ratio of the number of squares N_{sq} and triangles N_{tr} changes. When $N_{sq}/N_{tr} = \sqrt{3}/4$, the random tiling ensemble reaches a maximum entropy meaning that the number of tilings in the ensemble, or equivalently the number of possible configurations for the squares and triangles, is the highest. At this point, the random tiling ensemble forms a so-called *random-tiling quasicrystal* of 12-fold symmetry [61, 62, 138–140]. Typical tilings in this ensemble exhibit quasi-long-range order with algebraically decaying diffraction peaks at the positions of the 12-fold symmetric Bragg peaks of a dodecagonal quasicrystal, along with some diffuse scattering [74].

Hence, in our phase diagram, random tiling quasicrystals can be found at the specific composition that gives the right numbers of squares and triangles in the random tiling regions. The quasicrystal compositions have been marked in red in Fig. I.4 for each random tiling region.

The random tilings in Fig. I.4 are only square-triangle tilings when the size ratio q exactly corresponds to the magic ratio for either S2 or S1. In all other cases, the squares are deformed into rhombi. The resulting random tiling is a continuous deformation of a square-triangle tiling, but no longer possesses its 12-fold symmetry.

The coexistence of the newly identified S4 and T1 yields a rhombus-triangle random tiling, with an associated quasicrystal. The Floppy-Box simulations also revealed more optimally packed deformation paths for T2, T3 and S2 phases, that modify the extent of the stability regions in their vicinity. This causes the coexistence of the new S2 deformation with Hex_L to be more stable than T1 at $x_S = 2/3$, revealing a narrow rhombus-triangle random tiling region and hence a quasicrystal. In total, we find 4 different types of random tiling quasicrystal regions, obtained from S1-Hex_L, T1-Hex_L, S2-Hex_L and S4-T1 coexistences, at compositions $\sqrt{3}/(2+2\sqrt{3}) \approx 0.317$, $2\sqrt{3}/(2+3\sqrt{3}) \approx 0.481$, $4\sqrt{3}/(2+5\sqrt{3}) \approx 0.650$ and $(4+7\sqrt{3})/(6+8\sqrt{3}) \approx 0.812$ respectively.

I.4.1 Entropic quasicrystal locking

Neglecting the vibrational entropy contribution $\Delta S_{\text{vib}}^\infty$, in the limit of infinite pressure, the free-energy difference between the phase separated coexistence of

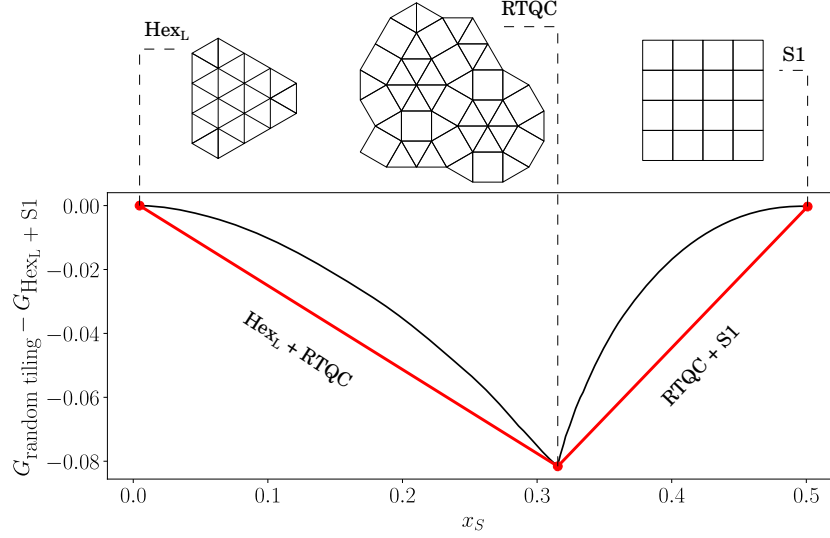


Figure I.8: Common tangent construction for additive hard disks at $q = \sqrt{2}-1$, considering the relative stability of the Hex_L , S1 and quasicrystalline phases, as well as the random tiling (black line). Because the tiling entropy is not concave, coexistences of the quasicrystal with either Hex_L or S1 are entropically favoured over a fully random tiling involving all particles.

Hex_L and the random tiling of squares and triangles is simply

$$\Delta G = -TS_{\text{conf}},$$

with S_{conf} the configurational entropy of the tiling, *i.e.*, up to a multiplicative Boltzmann constant factor, the number of ways one can randomly arrange squares and triangles in the tiling. This entropy was first estimated with transfer matrix [138, 141] and numerical [59] approaches, before exact analytical expressions were obtained with a Bethe ansatz [61, 62].

In Figure I.8, we plot the free-energy difference per particle $\Delta G/N$ at $q = \sqrt{2}-1$ for compositions between $x_S = 0$ (only large disks, pure Hex_L phase) and $x_S = 0.5$ (only squares, pure S1 phase), using data from Ref. 62. Strikingly, the free-energy difference is not convex. Hence, when performing a common tangent construction as described in section I.2.2, we find that the stable phase for $x_S \in]0, \sqrt{3}/(2 + 2\sqrt{3})[$ is a coexistence of a hexagonal close packing of large disks with the random tiling quasicrystal, and a coexistence of the random tiling quasicrystal with S1 for $x_S \in]\sqrt{3}/(2 + 2\sqrt{3}), 0.5[$. The system can achieve a greater configurational entropy by forming a highly entropic random tiling quasicrystal, and expelling the excess tiles (Hex_L triangles or S1 squares) in zero-entropy coexisting crystal phases rather than by completely mixing all available squares and triangles⁴. Therefore, at least at infinite pressure, the quasicrystal

⁴Interestingly, although one can tile the entire plane with squares and triangles, it is not

is a proper, well defined phase, with first-order purely entropic phase transitions to other phases[61, 62, 141].

Since rhombus-triangle tilings are isomorphic to square-triangle tilings, they have the same configurational entropy. Hence, this arguments holds similarly for random tilings regions identified in the phase diagram of Figure I.4.

I.5 Effects of non-additivity

We now turn our attention to non-additive binary hard-disk mixtures, focusing on non-additivity parameters $\Delta = -0.03, -0.05$ and -0.1 . The corresponding phase diagrams are presented in Figure I.9.

In addition to the non-additive versions of the phases in Figure I.2, using Floppy-Box Monte Carlo simulations, we find three new candidate structures depicted in Figure I.10 that are not stable with additive disks.

One of the most immediate effects of non-additivity occurs on the right-hand side of the phase diagram. While for additive disks, this region is dominated by a phase separation between large disks and small disks hexagonal crystals, non-additivity allows denser packings for high size ratios. One of these phases, H4, was not observed at all in the additive case. The repeating unit of this lattice is presented in Figure I.10-right. The others can be seen as variations of the H1 and H2 phases, deformed such that the lattice is approximately a hexagonal crystal of small disks with part of the particles replaced by large disks. At the exact size ratio where the contact distance between a large and a small disk $((1 + \Delta)(\sigma_S + \sigma_L)/2)$ is equal to σ_S , the large spheres can be placed randomly inside the hexagonal crystal of small spheres with no additional volume cost, leading to another region of lattice gas. However, for values of q slightly away from this magic ratio, deformations of the hexagonal lattice make this random placement unfavourable and the best-packed crystal remains periodic.

In addition to the changes at high values of q , two new phases, T4 and S5, are found stable at smaller size ratios. These structures are depicted in Figure I.10. T4 and H4 cannot exist without non-additivity, while S5 can, but turns out to not pack efficiently enough to be stable in the additive case.

In Figure I.9, two global trends are observed as Δ is increased. First, most phases can be seen as small disks enclosed into shells of large ones (see Fig. I.2). These phases quickly become unstable as q increases beyond the point where

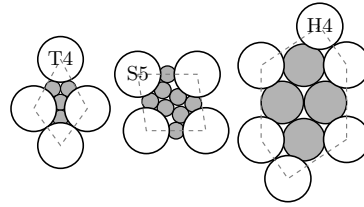


Figure I.10: Repeating units of the T4, S5 and H4 phases at $(q = 0.344, \Delta = -0.1)$, $(q = 0.337, \Delta = -0.1)$ and $(q = 0.905, \Delta = -0.05)$ respectively. These structures are only stable for non-additive hard disks.

possible to have these coexistences without a volume cost (gaps) at the boundary [140].

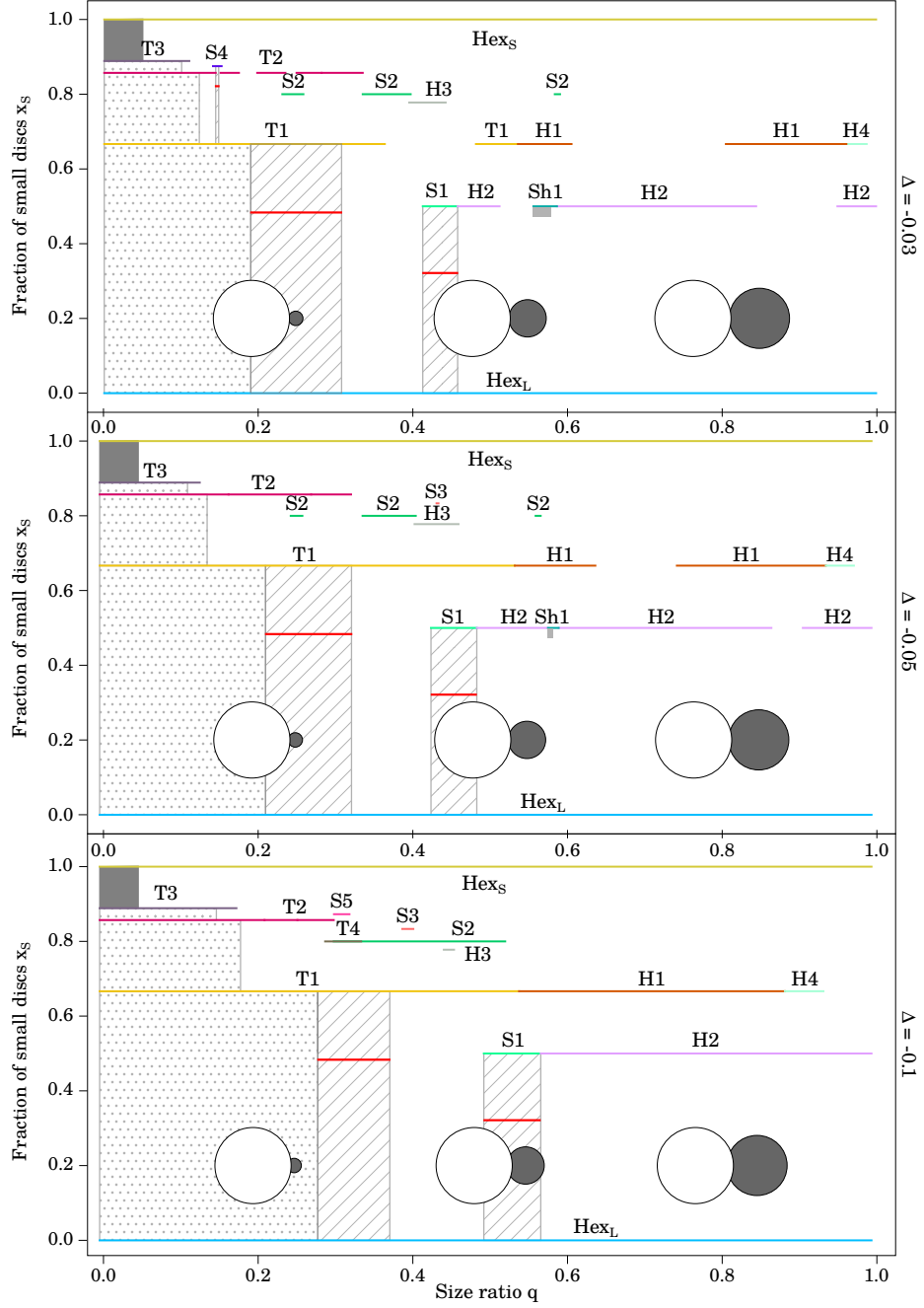


Figure I.9: Infinite pressure phase diagrams of binary non-additive hard disks mixtures for $\Delta = -0.03$ (top), $\Delta = -0.05$ (middle) and $\Delta = -0.1$ (bottom). The overlap between large and small disks allowed by the non-additivity is represented in each case for $q = 0.2, 0.5$ and 0.8 .

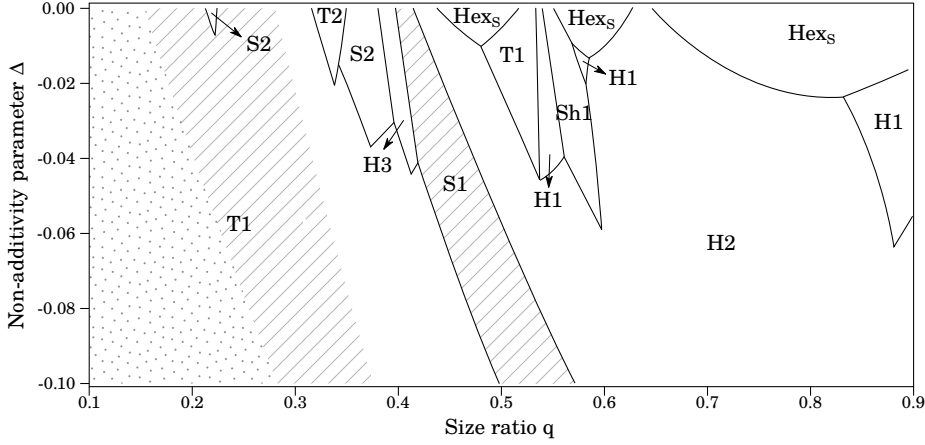


Figure I.11: Evolution of the phase diagram as a function of the non-additivity parameter $\Delta \in [-0.1, 0]$ at fixed composition $x_S = \sqrt{3}/(2 + 2\sqrt{3}) \approx 0.317$ where the S1-Hex_L quasicrystal is stable. At this composition, no pure periodic phase is stable, and the phase diagram consists of coexistences between Hex_L and other phases. For clarity, we only display the name of the pure phase in coexistence with Hex_L in the labels. As in previous diagrams, the dotted region highlights the random lattice gas and random tiling regions are hashed.

the (cluster of) small spheres fit into the holes left by the large ones. Non-additivity mitigates the inflation of the small disk clusters as q grows, which causes an overall shift of the phase diagram towards larger size ratios. Second, non-additivity favours phases with a large number of contacts between large and small disks, such as T1, S1, S2, H1 and H2. Those phases gradually take over larger and larger portions of the phase diagram.

Another interesting effect of non-additivity is the tendency to promote random lattice gas and random tiling regions. In Figure I.11, we plot the evolution of the phase diagram with Δ at a fixed composition $x_S = \sqrt{3}/(2 + 2\sqrt{3}) \approx 0.317$ equal to the composition where the pure Hex_L-S1 quasicrystal is stable. In this way, we can, for example, follow the expansion of the S1-Hex_L quasicrystalline region. As Δ decreases, S1 is one of the few remaining stable phases, along with T1 and H2. This results in a significant enhancement of the range of size ratios over which the S1-Hex_L quasicrystal is stable. In contrast, as seen in Fig. I.9, the random tiling regions involving S4 and T1, and S2 and Hex_L vanish for these values of Δ .

Despite our systematic search for candidate crystal structures, it is impossible to exclude the possibility that additional, better packing crystal structures are possible in these systems. As we limit ourselves here to unit cells containing

at most 12 particles, we miss all possibly densest structures with more complex unit cells.

Nevertheless, this study shows that simple packing considerations combined with configurational entropy are sufficient to stabilise quasiperiodic order in random tilings in the infinite pressure limit. 3D effects occurring in experimental self-assembly at interfaces, modelled here with non-additivity, enhance the stability region of the S1-Hex_L dodecagonal quasicrystal. The results of this Chapter are summarised in Reference 142.

The phase diagrams presented here are obtained in the infinite pressure limit. At finite pressures, particles can vibrate around their equilibrium position. This provides an extra source of entropy, which should simplify the phase diagram considerably, as some structures are expected to rapidly lose stability to other phases favoured by entropic considerations. On the other hand, numerical measurements of entropy are challenging and require quite advanced simulation techniques. Before diving into this topic in Chapter III, we will explore the finite pressure phase behaviour of the non-additive hard disk mixtures with direct self-assembly simulations in the next Chapter.

I.6 Acknowledgements

We thank Thomas Fernique for many interesting discussions and inputs on the state of the art of disks packing in mathematics.

Chapter II

Finite pressure self-assembly

In Chapter I, we showed that binary mixtures of non-additive hard disks exhibit a remarkably rich phase behaviour in the limit of infinite pressure. In particular several quasicrystalline phases are stable in this limit.

In practice however, self-assembly always takes place at finite pressures, when particles can diffuse to reach their equilibrium position. In this chapter, we want to look at the self-assembly of binary mixtures of non-additive hard disks, at finite pressure. To this end, we simulate large systems and directly study their self-assembly. In these numerical experiments, we focus on the special values of the non-additivity parameter Δ that correspond to an equivalent 3D geometry of spheres lying on a planar substrate.

As the mixture parameters are varied, we observe the direct self-assembly of several solid structures already observed in the infinite pressure limit. In particular, the dodecagonal random tiling quasicrystal of S1 squares and Hex_L triangles turns out to self-assemble spontaneously at finite pressures, for a range of size ratios and compositions. Finally, we report the self-assembly of an unexpected octagonal random tiling quasicrystal that was not foreseen in the infinite pressure exploration. This quasicrystal with eight-fold symmetry can self-assemble in a wide range of compositions by continuously adapting the relative concentration of tiles in its underlying random tiling. We use the high-dimensional representation of quasicrystals to study this new structure.

II.1 Numerical experiments

II.1.1 Spheres on a plane

At infinite pressures (see Chapter I), binary mixtures of non-additive hard disks in the thermodynamic limit were fully described by the size ratio of the disks q , the number fraction of small disks in the mixture x_S , and the non-additivity

parameter Δ . Here, the pressure (or packing fraction) becomes an additional relevant parameter, and it is no longer tractable to study the systems as all four parameters are independently varied.

Instead, we focus on the specific case of hard spheres of two different sizes constrained to lie on a flat plane. This geometry is motivated by self-assembly experiments of colloids on a substrate [106, 107], and might even provide valuable insights into the phase behaviour of out-of-equilibrium quasi-2D granular systems [143, 144]. As illustrated in Figure II.1 and already discussed in Section .6.2, binary mixtures of hard spheres on a plane can be mapped onto an equivalent 2D system by looking at the projection of the system on the plane, where spheres become disks. As the particles are constrained to move in only two dimensions, the disks corresponding to spheres of equal size cannot overlap, and hence interact simply as hard disks. However, for spheres of different sizes, a small amount of overlap of the 2D projections of the particles is allowed. Specifically, in the 2D projection, the distance of closest approach between a large particle of diameter σ_L and a small particle of diameter σ_S lying on the same plane is given by the geometric mean of their diameters $\sigma_{LS} = \sqrt{\sigma_L \sigma_S}$.

Focusing on the configuration of spheres lying on a plane amounts to imposing the relation (II.1) between the size ratio q and the non-additivity parameter Δ defined in Section .6.2.

$$\Delta = \Delta_{\text{plan}}(q) = \frac{2\sqrt{q}}{1+q} - 1 \quad (\text{II.1})$$

Then, the phase behaviour of a mixture of N_L large spheres and N_S small spheres confined to a substrate of area A is controlled by only three parameters: the size ratio $q = \sigma_S/\sigma_L$, the composition parametrised by the fraction of small spheres $x_S = N_S/(N_L + N_S)$, and the packing fraction $\eta = (N_S\sigma_S^2 + N_L\sigma_L^2)\pi/4A$, which corresponds to the area fraction occupied by the equivalent 2D disks. Since some overlap is allowed between different species in the 2D projection, the total packing fraction may exceed 1 in some cases.

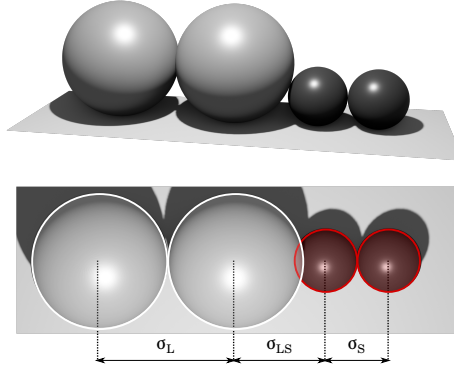


Figure II.1: Schematic depiction of the model. 3D hard spheres lying on a flat surface (top) can be interpreted as an equivalent 2D system of non-additive hard disks (bottom). Spheres of the same type behave like standard hard disks (their projections cannot overlap), while the closest projected distance between particles of different types σ_{LS} is smaller than the sum of the radii.

II.1.2 Event-driven molecular dynamics

To study the self-assembly of the mixtures, we perform event-driven molecular dynamics (EDMD) simulations in the canonical ensemble, *i.e.* at constant

number of particles N , volume V , and temperature T . In traditional molecular dynamics simulations, one specifies the interaction potential between the particles and computes the force acting on every particle in the system at each time steps. The equations of motion are then numerically integrated using a carefully chosen finite difference scheme to advance the system to a new configuration a small time step further [145, 146].

For systems with hard interactions however, the forces are singular: the particles feel no force at all until they collide. This breaks the standard molecular dynamics approach, but allows for a very efficient alternative simulation method called event-driven molecular dynamics (EDMD). Indeed, between two collisions, the particles move along straight lines at constant velocity and it is easy to compute the exact time of future collisions. The event-driven algorithm is the following:

1. Prepare a system with initial positions and velocities.
2. Predict the time of the collisions that will occur in the future.
3. Jump straight to the time of the earliest collision, and update the velocities of the colliding particles using conservations of energy and momentum.
4. Repeat from 2.

The method is named *event-driven* because time progresses by jumps of variable size from a collision event to the next, rather than by small fixed time increments. Several optimisations can be made to store the event list in an efficient data structure, or predict only the relevant collisions [147–151]. For hard-sphere systems, event-driven molecular dynamics simulations are extremely efficient and typically much faster than simple Monte Carlo schemes, especially at the relatively large densities relevant to the study of solids [152].

The simulation code used is a variant of the simulation code provided in Reference 151, which was adapted to non-additive hard disks in two dimensions. Initial configurations are obtained by starting in a dilute state at the desired composition, and then performing an EDMD simulation in which the particle diameters grow until the desired packing fraction is reached [151].

II.2 Self-assembly results

II.2.1 Infinite pressure

Even for simple binary mixtures in 2D, the number of different ordered structures that can emerge can be quite large and difficult to enumerate. To obtain an impression of the structures we might expect to find, we first compute the phase diagram of the system in the limit of infinite pressure using the procedure presented in Chapter I. Instead of a fixed non-additivity parameter Δ , we use the size ratio dependant Δ_{plan} of equation (II.1). The resulting phase diagram is shown in Figure II.2.

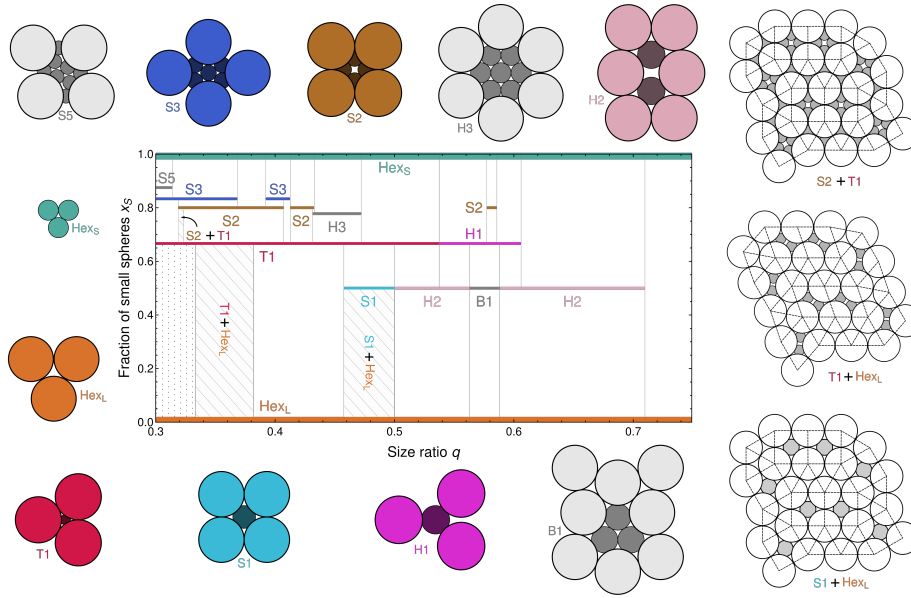


Figure II.2: Infinite-pressure phase behaviour of binary mixtures of spheres on a flat plane, as a function of the size ratio q and fraction of small particles x_s . Phases are labelled following the naming scheme of References 142 and 74. The white regions correspond to coexistences between the phases directly above and below. The hashed and dotted areas indicate regions where these two phases can form random tilings or a lattice gas, respectively. Examples of finite patches of the three possible random tilings, corresponding to the hashed regions in the diagram, are displayed on the right.

For each binary phase in Figure II.2 we also depict the repeating unit that can be used to construct the crystal phase. We obtain again lattice gas and random tiling regions discussed in Section I.3.1. The dodecagonal random tiling quasicrystal described in section I.4 made of S1 squares and Hex_L triangles is still stable for the geometry of spheres on a plane, at its composition $x_S = (3 - \sqrt{3})/4 \simeq 0.317$ [59, 74, 140, 142]. Two closely related tilings, also illustrated in Figure II.2 are found at lower size ratios. As a result, one intriguing prediction from Figure II.2 is the possibility of a 12-fold quasicrystal self-assembling from simple binary mixtures of hard colloidal spheres on a substrate at infinite pressure.

II.2.2 Finite pressure self-assembly

In practice, the infinite-pressure phase behaviour is not a reliable indication for the phases one might find in a real self-assembly experiment. Self-assembly in a colloidal system takes place at finite pressure, where contributions from the vibrational entropy to the free energy of different solid¹ phases can fundamentally change the phase behaviour. Moreover, dynamical arrest or competition with other candidate phases can prevent the reliable formation of a structure even if it is thermodynamically stable.

Hence, for a more realistic look at the self-assembly, we perform event-driven molecular dynamics simulations in the canonical ensemble, *i.e.* at constant number of particles N , volume V , and temperature T on an extensive grid of state points spanning size ratios $0.25 \leq q \leq 0.75$ in steps of 0.05, compositions $0.05 \leq x_S \leq 0.95$ in steps of 0.05. The packing fraction η ranged from 0.7 to up to 1.0 in steps of 0.01, where we only considered state points where the growing-particle simulations were able to rapidly reach the desired packing fraction without jamming. In other words, we assume that at packing fractions where jamming occurs during our initial compression, the system would likely be too densely packed to observe self-assembly on a reasonable time scale. The initial configurations contain $N_L + N_S = 2000$ particles. Each self-assembly simulation is allowed to run for at least $10^6 \tau_{\text{MD}}$, with $\tau_{\text{MD}} = \sqrt{m\sigma_L^2/k_B T}$ our simulation time unit, m the mass of a particle², σ_L the large-particle diameter, and k_B Boltzmann's constant. Subsequently, longer simulations were performed for state points where self-assembly was considered likely to occur on a reason-

¹The Mermin-Wagner theorem forbids the existence of long-range translational order in 2D at finite pressure[153]. The proof given in Ref. 153 requires some assumptions on the interaction potential which are quite general but nonetheless excludes hard interactions. However, long wavelength density fluctuations caused by the Mermin-Wagner instability have been measured both in colloidal self-assembly experiments and hard disks simulations [154]. Hence, strictly speaking, there are no *crystals* at finite pressure and we instead name the self-assembled structures *solids* which can have quasi-long-range translational order and long-range orientational order. Interestingly, while for hard condensed matter systems, samples of cosmological size would be required to detect the very weak effects of the Mermin-Wagner instability [155, 156], it becomes measurable in the dynamics of only a few thousands of particles in soft matter systems [154].

²Since the equilibrium phase behaviour of the system does not depend on the mass of the particles, we chose them equal for both species.

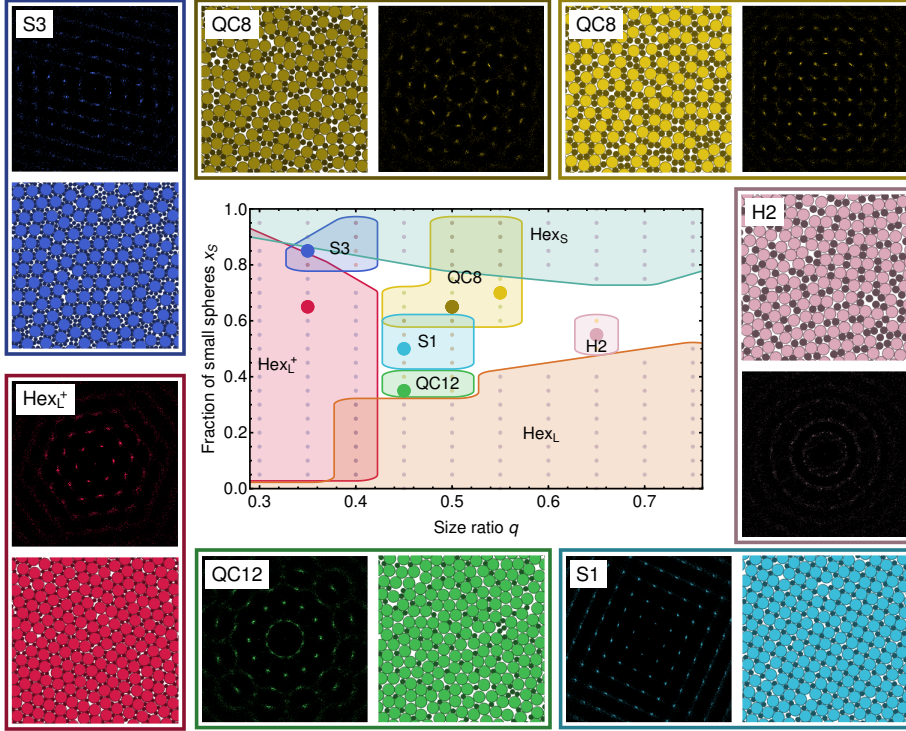


Figure II.3: Self-assembly summary for binary mixtures of spheres on a flat plane, as a function of the size ratio q and fraction of small particles x_S . For each combination of q and x_S , we perform simulations at a range of different packing fractions, and report the observed phases. A coloured point in the phase diagram indicates the self-assembly of the corresponding phase. At state points where no point is shown, no crystallization was detected. For each binary crystal phase, we include a typical snapshot and the scattering pattern that results from a Fourier transform of the positions of the large spheres. For the QC8 phase, we include two snapshots: one containing a large concentration of S1 squares (top middle) and one containing a large concentration of S2 squares (top right). Hex_L and Hex_S are hexagonal crystals consisting of only large or small spheres, respectively, and are not depicted.

able time-scale based on the final configurations of the first simulations. For each simulation, we measure the two-dimensional structure factor of the final configuration by computing

$$S(\mathbf{k}) = \frac{1}{N} \left| \sum_{n=1}^N \exp(i\mathbf{k} \cdot \mathbf{r}_n) \right|^2. \quad (\text{II.2})$$

where \mathbf{k} is an allowed wave vector in the periodic simulation box, and \mathbf{r}_n is the position of particle n . Up to a multiplicative factor, the static structure factor is identical to the diffraction pattern that would be obtained in a diffraction experiment for instance. Hence, it is very useful for detecting crystallisation, which manifests itself by the appearance of sharp peaks in the diffraction pattern. Disordered structures exhibit only ring, liquid-like structure factors.

The self-assembly results are summarized in Fig. II.3. The central diagram reports for each investigated combination of q and x_S what ordered phases were observed. We consider a structure to have self-assembled for a given combination of q and x_S when we find significant clusters of the structure in the simulation box for at least one packing fraction. At state points without an indicated crystal phase, no crystallization was observed at any of the investigated packing fractions. For the quasicrystals, local crystalline order is typically hard to see by eye, and we instead rely on the symmetry of the scattering pattern for our classification.

The simulations show that a number of the best-packed phases predicted in Figure II.2 indeed spontaneously self-assemble. Naturally, this includes the trivial hexagonal solids of the large and small spheres (Hex_L and Hex_S) that can be found at compositions close to $x_S = 0$ and 1, respectively. Additionally, we observe large-scale self-assembly into the S1 and S3 phases close to the regions expected from Figure II.2. We also observe the more complex H2 phase, albeit only in finite clusters – a closer inspection of the systems where these form show a very low overall mobility of the system, suggesting that crystallization of this phase is hindered by slow dynamics. For sufficiently low q , the system nearly always forms a hexagonal lattice of large spheres, with the small spheres interspersed between them (labelled Hex_S^+). Depending on the composition, this may look similar to the T1 phase (as depicted in the sample snapshot in Figure II.3), but the number of small spheres per triangular cavity in the lattice of large spheres appears to continuously depend on the composition x_S . For $x_S < 2/3$, this simply means that a random selection of the triangular holes are empty, resulting in a lattice gas or interstitial solid solution [74, 142]. For larger x_S , progressively more small particles are included between the large spheres, but we observe no clear structural transition between these regimes. Hence, we choose to collectively indicate this region as Hex_S^+ .

Most intriguingly, in addition to these periodic phases, we also observe the self-assembly of two distinct quasicrystals, both at size ratios between $q = 0.45$ and $q = 0.55$. The dodecagonal quasicrystal (QC12) that appears at low fractions of small spheres is indeed the square-triangle tiling [59, 74, 140, 142] expected from the infinite-pressure diagram. It is made of regular squares and

triangles (S1 and Hex_L tiles). This quasicrystal is analogous to a number of quasicrystals observed in soft matter systems, including binary Lennard-Jones mixtures [157], patchy particles with attractive patches [94–96], hard disks with a square-shoulder repulsion [87, 88], binary mixtures of nanoparticles [50], block copolymers [49, 85], and soft repulsive colloids [82, 84]. Additionally, various 3D systems have been shown to form quasicrystals consisting of layers of a square-triangle tiling [38, 91, 158, 159].

II.3 A new octagonal quasicrystal

The second quasicrystal (QC8) has octagonal symmetry and is also a random tiling quasicrystal. It consists of a mixture of three tiles: isosceles triangles, small squares, and larger squares. Octagonal quasicrystals are notably rarer than dodecagonal ones in soft matter, and to our knowledge, this specific quasicrystal with three types of tiles has never been studied before. In this Section, we examine this new quasicrystal in detail. After verifying that the identified tiles indeed define a good random tiling model, we propose a lifting to a hyperspace of four dimensions for the structure. We then use the lift to derive a prediction for the tiles concentrations in the perfect octagonal random tiling quasicrystal and compare it to the values measured in the self-assembled systems. Finally, we show that the stability of the QC8 can be understood by simple geometric arguments.

II.3.1 Random tiling reconstruction

The quasicrystalline phases can be rationalised as tilings of the plane by decorated tiles. We find that the structures are predominantly formed of a mixture of three tiles: the isosceles triangles that appear in the H1 phase, the squares from the S1 lattice, and the larger squares from the S2 lattice. To identify the underlying tiling from simulation snapshots, we first create bonds between all large particles that are closer than $1.7\sigma_{LL}$. Since this cut-off distance is larger than $\sqrt{2}\sigma_{LL}$, crossing bonds are formed inside small S1 squares. We remove these crossing bonds before further analysis.

The bond network is characterised by the bonds length and angle distributions, as shown in Figure II.4 for a typical quasicrystal configuration resulting from self-assembly. In the vicinity of the QC8 region, the bonds length distribution is clearly bimodal. A cut-off is set at the minimum of the distribution in-between the two peaks, which discriminates between long and short bonds. Since the cut-off value can vary slightly with the composition and packing fraction of the system, it is determined separately for each simulation snapshot. The bond angle distribution exhibits 16 sharp peaks. Correlating the orientation with the bond length shows that short and long bonds each follow a distinct set of 8 orientations, offset by $\pi/8$. Tiles are then reconstructed from cycles, and sorted by shape and orientation. Two examples of reconstructed tilings are shown in Figure II.5.

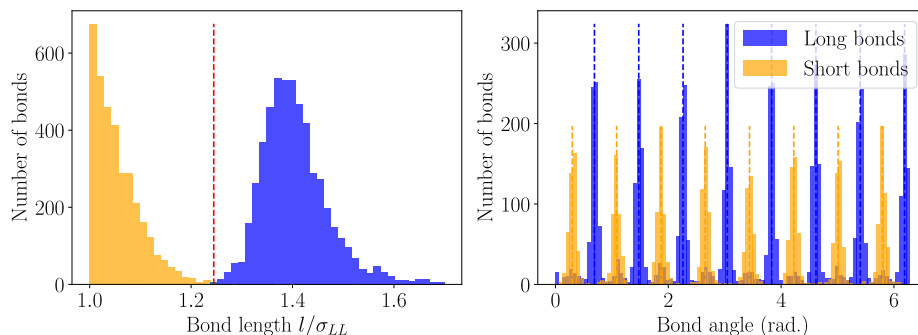


Figure II.4: Neighbour bonds characterisation in a system of 10^4 non-additive hard disks, with size ratio $q = 0.5$, composition $x_S = 0.675$ and packing fraction $\eta = 0.86$. This system forms an octagonal random tiling quasicrystal. (Left) Bonds length distribution showing a clear distinction between short and long populations. The vertical red line highlights the cut-off value obtained as the minimum in the dip. (Right) Bonds angle distribution. The 16 peaks correspond to the possible edge orientations in the tiling underlying the reported octagonal quasicrystal. Short (orange) and long (blue) bonds follow two distinct set of 8 orientations, offset by $\pi/8$. Bond angles are relative to the horizontal.

II.3.2 A random tiling model

Before going further in the analysis of the self-assembled structures, we want to explore the properties of the perfect³ tiling formed by the identified set of prototiles. By looking at the reconstructed tilings, we identify 12 prototiles of 3 distinct shapes: small squares (2 orientations), large squares (2 orientations) and isosceles triangles (8 orientations). The two long edges of the isosceles triangles match the edges of the large squares while the edges of the small squares attach to the short edge of the triangles. Since the opening angle of the triangles is $\pi/4$, for a long edge length a , the short edges have length $\sqrt{2 - \sqrt{2}}a \approx 0.765a$. The prototiles are depicted in Table II.1.

We want to make sure that the identified set of prototiles defines a proper random tiling model. In his textbook chapter on random tiling models for quasicrystals [30], Henley defines a random tiling as a set of prototiles and packing rules that defines an ensemble of allowed configurations with the following two properties:

1. Structurally distinct tiling configurations are possible. More specifically, several configurations with different global perpendicular strains are possible (see section II.3.3 for a discussion of perpendicular strain).

³We call *perfect* a tiling configuration that covers the plane without gaps or overlaps, with undeformed tiles. The tilings underlying the self-assembled structures contain a lot of defects and are thus not perfect. In a random tiling ensemble, as defined in Section I.4, all configurations are perfect.

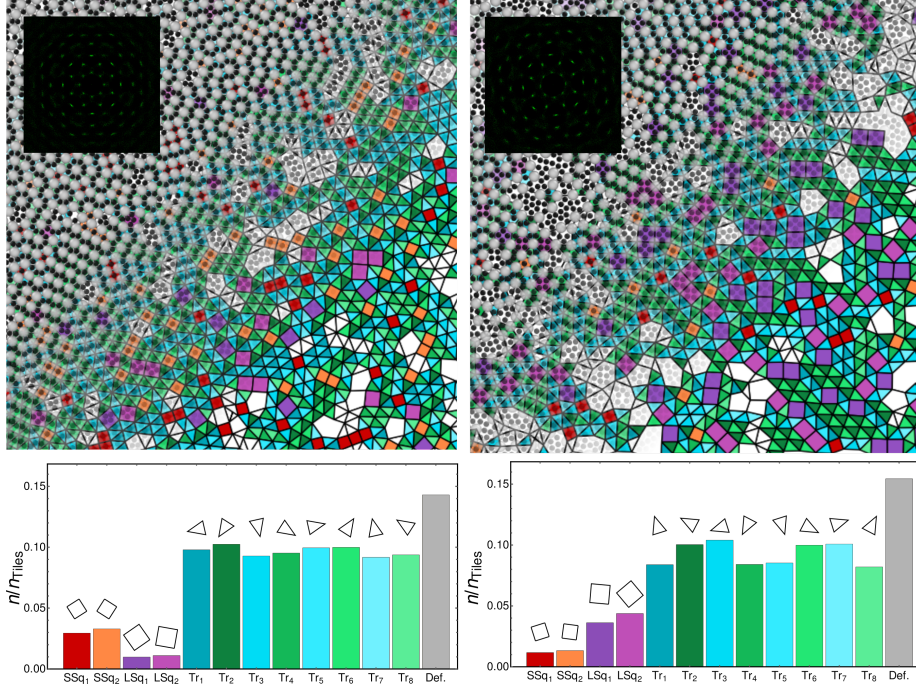


Figure II.5: Self-assembled octagonal random-tiling quasicrystals in mixtures of 10^4 spheres on a flat plane, at state points corresponding to the QC8 phase with different concentrations of large and small squares. The underlying tilings are highlighted and tiles coloured according to shape and orientation. The insets show the diffraction patterns, signalling the global 8-fold symmetry. Tile distributions show that all tile orientations of the same shape appear with similar frequencies. The bar labelled “Def.” denotes all tiles that could not be classified as either small square, large square or triangle. The state points are: (Left) $q = 0.5$, $x_S = 0.675$ and $\eta = 0.86$. (Right) $q = 0.55$, $x_S = 0.715$ and $\eta = 0.84$.

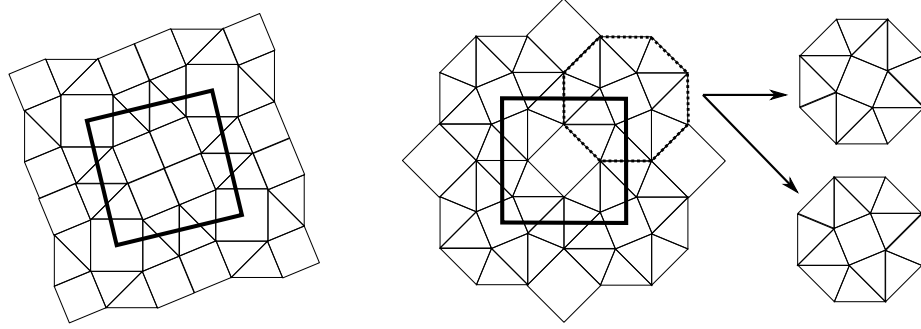


Figure II.6: Examples of two structurally distinct periodic tilings formed by the identified prototiles. Thick black lines highlight the unit-cells. The second tiling contains a finite concentration of octagonal clusters that can appear in two different orientations.

2. The number of allowed configurations grows exponentially with the size of the tiling.

The first condition can be checked by constructing two distinct periodic tilings with the provided set of prototiles. Two such structures are presented in Figure II.6 for the three-tiles tiling of interest here.

For the second condition, we note that the second example tiling in Figure II.6 contains a finite concentration of octagonal clusters formed of one small square and 12 triangles. These cluster can adopt two different orientations without disrupting the surrounding tiles. In a finite patch of tiling containing N of these clusters, 2^N distinct configurations are possible. If the size of the tiling patch is doubled, the number of possible configurations grows exponentially to 2^{2N} , which verifies the second condition for a random tiling model. Note that since the entropy is the logarithm of the number of configurations, condition 2 amounts to having a finite configurational entropy per vertex in the random tiling ensemble. Therefore, our set of three tiles defines a proper random tiling ensemble.

II.3.3 Lift to four dimensions

As discussed in Section .1, the vertices of a periodic lattice in dimension d can be indexed with a set of d integers. In contrast, one usually needs more than d integers to uniquely index all the vertices of a quasicrystal. This suggests that quasicrystals are linked to periodic lattices in higher dimensions. Indeed, in general, quasicrystal vertices can be seen as a projection of a higher-dimensional periodic hyperlattice onto a lower dimensional space [9, 37]. Although this representation can appear rather artificial at first, it in fact proves very powerful to analyse quasicrystals, and provides valuable physical insights. Here, we show how to construct a 4-dimensional lattice that captures the structures of the octagonal tiling following the procedure outlined in Reference 30.

The process of linking the vertices of quasicrystal to a set of points in the lattice of dimension $D > d$ is called *lifting* [31, 32]. The higher-dimensional space E (or *lift space*) can be decomposed into a so-called *parallel* or *physical* subspace E^\parallel of dimension d , and its supplement E^\perp of dimension $D - d = d^\perp$ call *perpendicular* subspace.

$$E = E^\parallel \oplus E^\perp \quad (\text{II.3})$$

A vector in the basis $\{\mathbf{e}_i\}_{i=1}^D$ of E can be written as $\mathbf{e}_i = (\mathbf{e}_i^\parallel, \mathbf{e}_i^\perp)$ with $\mathbf{e}_i^\parallel \in E^\parallel$ and $\mathbf{e}_i^\perp \in E^\perp$. The quasiperiodic tiling is then the projection of points of the D -dimensional lattice on the parallel space.

We start by constructing the parallel components $\{\mathbf{e}_i^\parallel\}_{i=1}^D$ of the lift-basis as the largest⁴ set of vectors allowing a unique (up to a choice of origin) indexing of every vertex in the tiling, *i.e.* such that for every vertex of the tiling with coordinates \mathbf{x}^\parallel ,

$$\mathbf{x}^\parallel = \sum_{i=1}^D n_i \mathbf{e}_i^\parallel, \quad n_i \in \mathbb{Z} \quad (\text{II.4})$$

In the octagonal tiling, each long edge can only lie along one of 4 different orientations \mathbf{e}_1^\parallel through \mathbf{e}_4^\parallel , illustrated in Figure II.7-top. Short edges can then be constructed by taking the difference between two of these vectors (e.g. $\mathbf{e}_2^\parallel - \mathbf{e}_1^\parallel$). As a result, each vertex in the tiling can be written as a linear combination of an integer number of the four vectors \mathbf{e}_i^\parallel , and hence can be seen as a point on a lattice in dimension $D = 4$. It is easily checked that the sum of \mathbf{e}_i^\parallel along any closed path in the tiling is 0, which ensures that this set of vectors allows to index all vertices in a unique way, up to a choice of origin [30].

We now construct the perpendicular components $\{\mathbf{e}_i^\perp\}_{i=1}^D$ of the lift-basis. We use the action of transformations on the tiling to constrain the choices of the perpendicular components. Under a rotation of $\pi/4$, the parallel projections realise the following permutation:

$$\begin{aligned} \mathbf{e}_1^\parallel &\rightarrow \mathbf{e}_2^\parallel \\ \mathbf{e}_2^\parallel &\rightarrow \mathbf{e}_3^\parallel \\ \mathbf{e}_3^\parallel &\rightarrow \mathbf{e}_4^\parallel \\ \mathbf{e}_4^\parallel &\rightarrow -\mathbf{e}_1^\parallel \end{aligned} \quad (\text{II.5})$$

The rotation by $\pi/4$ in the parallel subspace E^\parallel corresponds to a more general transformation in the 4-dimensional lift space E , that permutes the basis vectors \mathbf{e}_i according to (II.5) without the \parallel superscripts. Hence, the action of the 4D transformation on the perpendicular subspace E^\perp should again realise the same

⁴It might happen that all vertices of a tiling can be uniquely indexed by n or $m > n$ integers. In that case, m should be used. See Ref. [30] for details.

permutation. Without loss of generality, we fix $\mathbf{e}_1^\perp = (1, 0)$. Then, we look for a transformation that will generate the other perpendicular vectors and satisfy the permutation (II.5) with \parallel superscripts replaced by \perp . Using a rotation by $\pi/4$ again obviously satisfies the permutation requirement, but results in a trivial E in which the projections of the 4D lattice on E^\parallel and E^\perp give the same tiling, and nothing more is learnt. Therefore, we need to find a different transformation. Restricting ourselves to rotations, we find that a rotation of $3\pi/4$ satisfies the permutation⁵. Hence, by applying successive rotations, we generate the projections of the four basis vectors on the perpendicular space depicted in Figure II.7-bottom.

Using this procedure, we recover the vectors that are traditionally used to lift quasicrystals of the Ammann-Beenker family [32, 82], to which the QC8 presented here is indeed related as discussed in the next subsection.

For any tiling made from the prototiles of the QC8 tiling, we can now use the lifting vectors in Figure II.7 to associate each vertex with a point of the 4D lattice. Each tile is lifted to the facet of a corrugated hypersurface in 4D (a generalisation of the 1D “surface” that represented the Fibonacci sequence in Section .1), as illustrated in Figure II.8, whose projection on the parallel space is the tiling. The perpendicular space is the orthogonal supplement to E^\parallel in E . In the 3D representation of Figure II.8, E^\perp reduces to the 1D vector space in the ϕ vertical direction.

A tiling is *globally uniform* when the corrugated hypersurface is essentially flat, *i.e.* it follows a hyperplane in E [140, 160]. In practice this means that the tiling looks homogeneous in E^\parallel . In this case, there is a well-defined average hyperslope between the corrugated surface and the parallel subspace, which is called the *global perpendicular strain*. For a tiling in dimension d lifted to a space of dimension D , the hyperslope is a $d \times (D - d)$ matrix that encodes how much displacement \mathbf{x}^\perp in E^\perp is caused by a displacement \mathbf{x}^\parallel in E^\parallel .

Periodic tilings are globally uniform with non-zero perpendicular strain. Quasicrystals however have zero global perpendicular strain, which means that their corrugated hypersurface is essentially parallel to E^\parallel . As a consequence, the hypersurface is orthogonal to E^\perp , and the lifted vertices projections form a dense set in a finite region of the perpendicular subspace, called the *acceptance region*.

The lifted representation of tilings encodes the extra phasonic degrees of

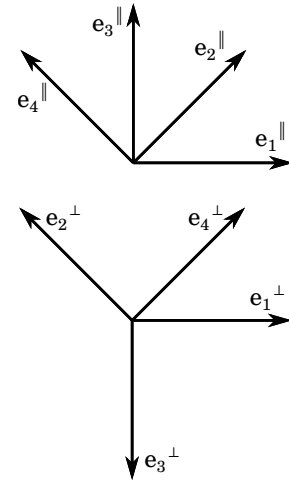


Figure II.7: Projections of the 4D lift vectors on the parallel (top) and perpendicular (bottom) sub-spaces.

⁵A rotation of $5\pi/4$ would result in an equally valid set of perpendicular vectors mirrored about the \mathbf{e}_1^\perp direction.

freedom that are specific to quasicrystals. It is also very useful to analyse them. In particular, in globally uniform tilings, the global perpendicular strain is directly linked to the concentration of the various types of tiles.

II.3.4 Tile concentrations

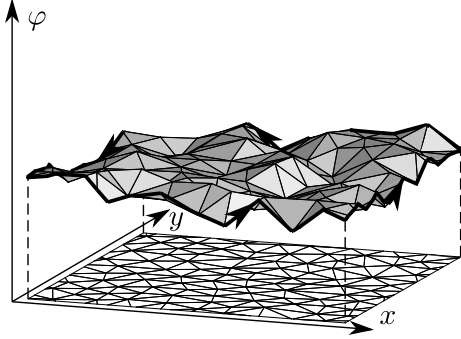


Figure II.8: Schematic representation of a lifted tiling. The bottom flat plane is the parallel space E^{\parallel} in which the tiling lives. The lifted vertices form a hypersurface in the lift space, here of dimension $D = 3$ to allow representation. Courtesy of P. Kalugin and A. Katz, from [160].

In Figure II.5, we show portions of the final state of two simulated mixtures of 10^4 particles, at different state points. The left one is dominated by small squares, while the right one, which contains more small particles, predominantly contains large squares. Both systems possess global octagonal symmetry as indicated by the diffraction patterns. The analysis of the tile orientations shows that for a given shape – small squares, large squares and isosceles triangles – all possible orientations appear roughly with the same frequency, which is a common feature of random-tiling quasicrystals [140]. Random tilings with the same number of tiles in all orientations are called *maximally symmetric* tilings.

As illustrated in Figure II.5, the relative concentrations of the different tiles in the QC8 phase vary drastically as a function of the fraction of small spheres in the system. Since the S2 squares contain 4 small particles each, while the S1 squares only contain a single small sphere, higher compositions x_S favour a larger concentration of S2 squares. For high x_S , the QC8 tiling consists almost purely of large S2 squares and H1 triangles, with the triangles joined in pairs that form a thin rhombus. In this limit, the tiling can be seen as a mixture of just two types of tiles – square and rhombic – that are identical to the tiles that form e.g. the Ammann-Beenker [23, 26] and Watanabe-Ito-Soma [24] octagonal aperiodic tilings. The same tiling – with different decorations of the tiles with particles – was previously observed in simulations of soft colloids [82], particles with an oscillating interaction potential [79, 84], and patchy particles [97]. However, to our knowledge, no octagonal quasicrystal has yet been observed to spontaneously self-assemble in soft-matter experiments.

On the other hand, at low x_S the quasicrystal approaches a tiling of only H1 triangles and small S1 squares. This can be seen as a separate two-tiles random-tiling quasicrystal which, to our knowledge, has not previously been observed in soft matter systems. Interestingly, however, a closely related tiling, where the isosceles triangles are slightly deformed, was recently conjectured to

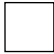
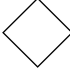






Name	Tile	Area A_{X_i}	Hyperslope B_{X_i}	$\det B_{X_i}$
S_1		a^2	$\begin{pmatrix} 1 & 0 \\ 0 & -1 \end{pmatrix}$	-1
S_2		a^2	$\begin{pmatrix} -1 & 0 \\ 0 & 1 \end{pmatrix}$	-1
s_1		$(2 - \sqrt{2})a^2$	$(1 + \sqrt{2}) \begin{pmatrix} 0 & -1 \\ -1 & 0 \end{pmatrix}$	$-3 - 2\sqrt{2}$
s_2		$(2 - \sqrt{2})a^2$	$(1 + \sqrt{2}) \begin{pmatrix} 0 & 1 \\ 1 & 0 \end{pmatrix}$	$-3 - 2\sqrt{2}$
$T_{1,5}$		$\frac{1}{2\sqrt{2}}a^2$	$\begin{pmatrix} 1 & -2 \\ 0 & 1 \end{pmatrix}$	1
$T_{2,6}$		$\frac{1}{2\sqrt{2}}a^2$	$\begin{pmatrix} -1 & 0 \\ 2 & -1 \end{pmatrix}$	1
$T_{3,7}$		$\frac{1}{2\sqrt{2}}a^2$	$\begin{pmatrix} -1 & 0 \\ -2 & -1 \end{pmatrix}$	1
$T_{4,8}$		$\frac{1}{2\sqrt{2}}a^2$	$\begin{pmatrix} 1 & 2 \\ 0 & 1 \end{pmatrix}$	1

Table II.1: Summary of the 12 different prototiles comprising the QC8 tiling. The third column reports the area of each tile, assuming that large squares have edges of length a . The fourth column contains the constant hyperslope of each tile, *i.e.* the 2x2 matrix that maps points inside that tile in the original tiling to the perpendicular space. The last column displays the determinant of the hyperslope for each tile, which is used to obtain Eq II.11.

be the densest-packed structure for a ternary mixture of hard disks [161].

It is interesting to consider under what conditions the QC8 tiling observed here can exhibit true 8-fold symmetry. As developed in Reference 140, we use the lifted representation of the tilings to 4D in order to determine constraints on the relative concentrations of the different tiles.

For the square-triangle tiling associated with the QC12 phase, it is well known that global twelve-fold symmetry only occurs under the condition that the two area fractions of the tiling covered by squares and triangles are the same and equal to 1/2 [59, 62, 140]. Here, we determine under what conditions the QC8 phase can exhibit 8-fold symmetry. To this end, we consider a QC8 tiling consisting of large squares S , small squares s , and triangles T , with long edge length a . Counting the different orientations, this results in a total of 12 different prototiles: two orientations of both types of squares, and 8 orientations of the triangles. These are listed in Table II.1. We then consider an infinite, globally uniform tiling consisting of a mixture of these tiles, with the area fraction covered by each tile type denoted as Σ_i for the large squares, σ_i for the small squares, and τ_i for the triangles, where i denotes the orientation of the tile.

The first obvious constraint on our tiling is that it should cover the entire plane. Hence, the area fractions must satisfy

$$\Sigma + \sigma + \tau = 1, \quad (\text{II.6})$$

where $\Sigma = \sum_i \Sigma_i$, $\sigma = \sum_i \sigma_i$, and $\tau = \sum_i \tau_i$.

One set of constraints on these tile concentrations follows from the simple observation that each edge must have an opposing partner. Considering, for example, the short edge in triangle T_1 , this leads to the constraint that

$$n_{T_1} + n_{s_1} = n_{T_5} + n_{s_1}, \quad (\text{II.7})$$

with n_{X_i} denotes the number of tiles of type X_i . This trivially implies that $\tau_1 = \tau_5 = \tau_{15}/2$, and likewise it can be shown that $\tau_2 = \tau_6 = \tau_{26}/2$, $\tau_3 = \tau_7 = \tau_{37}/2$, and $\tau_4 = \tau_8 = \tau_{48}/2$.

Another constraint on the various tile concentrations can be obtained by lifting the tiling to four-dimensional space. For this, we follow the procedure outlined in e.g. [32, 59, 140].

Using the lifting basis constructed in the previous subsection II.3.3 we consider a mapping $\phi(\mathbf{r})$ that maps each vertex in our original tiling to its corresponding point in the perpendicular space. Within each tile, $\phi(\mathbf{r})$ is a linear interpolation between the mapped vertices of that tile. Hence, ϕ is a continuous, piecewise linear function, with a constant hyperslope within each tile. The hyperslope within one tile is completely determined by the vectors that form it. Hence, tiles of the same type and orientation have the same hyperslope. Specifically, within a tile X_i , the hyperslope B_{X_i} is given by:

$$B_{X_i} = \begin{pmatrix} \frac{\partial \phi_x}{\partial x} & \frac{\partial \phi_x}{\partial y} \\ \frac{\partial \phi_y}{\partial x} & \frac{\partial \phi_y}{\partial y} \end{pmatrix}. \quad (\text{II.8})$$

In Table II.1, we report the hyperslope for each of the 12 tiles in the QC8 tiling.

In a globally uniform tiling, over long distances \mathbf{r} , $\phi(\mathbf{r})$ has a well-defined average hyperslope B (also known as the global perpendicular strain), which can be written as the weighted sum of the hyperslopes of the individual tiles [140]:

$$B = \sum_{i=1}^2 \Sigma_i B_{S_i} + \sum_{i=1}^2 \sigma_i B_{s_i} + \sum_{i=1}^8 \tau_i B_{T_i}. \quad (\text{II.9})$$

Following Ref. 140, uniformity of the tiling then imposes that

$$\sum_{i=1}^2 \Sigma_i \det B_{S_i} + \sum_{i=1}^2 \sigma_i \det B_{s_i} + \sum_{i=1}^8 \tau_i \det B_{T_i} = \det B. \quad (\text{II.10})$$

Using the matrices listed in Table II.1, this leads to the following constraint:

$$\begin{aligned} \Sigma + (3 + 2\sqrt{2})\sigma - \tau &= (\Sigma_1 - \Sigma_2)^2 + (3 + 2\sqrt{2})(\sigma_1 - \sigma_2)^2 - \tau^2 \\ &\quad + (2 + 2\sqrt{2})(\tau_{15} - \tau_{26} + \tau_{37} - \tau_{48})(\sigma_1 - \sigma_2) \\ &\quad + 8(\tau_{15}\tau_{37} + \tau_{26}\tau_{48}). \end{aligned} \quad (\text{II.11})$$

This constraint can be regarded as the equivalent of the Nienhuis relation [139] for the QC12 square-triangle tiling, but for the QC8 tiling.

Assuming that the octagonal tiling is maximally symmetric:

$$\Sigma_1 = \Sigma_2 = \frac{\Sigma}{2} \quad (\text{II.12})$$

$$\sigma_1 = \sigma_2 = \frac{\sigma}{2} \quad (\text{II.13})$$

$$\tau_{15} = \tau_{26} = \tau_{37} = \tau_{48} = \frac{\tau}{4}. \quad (\text{II.14})$$

When we impose this, the average hyperslope B vanishes (zero perpendicular strain), and as a result the right-hand side of Eq. II.11 similarly becomes zero, yielding:

$$\Sigma + (3 + 2\sqrt{2})\sigma - \tau = 0. \quad (\text{II.15})$$

Finally, we can express the area fractions Σ , σ and τ in terms of the particle composition x_S by using the known composition of each tile, combined with equations II.6 and II.15.

$$\Sigma = \frac{2(4 + 3\sqrt{2})x_S - 4\sqrt{2} - 5}{6 - 4x_S} \quad (\text{II.16})$$

$$\sigma = \frac{-(4 + \sqrt{2})x_S + 4}{6 - 4x_S} \quad (\text{II.17})$$

$$\tau = \frac{-(8 + 5\sqrt{2})x_S + 4\sqrt{2} + 7}{6 - 4x_S} \quad (\text{II.18})$$

In Figure II.9, we draw this prediction together with the measured tile concentrations in our self-assembled configurations of 10^4 particles. In the analysis of the simulation data, we consider only the portion of the system covered by the three valid types of tiles and omit all defects. We find that the observed tile concentrations are essentially independent of size ratio and packing fractions within the investigated regime. Considering the fact that the analysed configurations were the result of spontaneous self-assembly, and hence contain significant number of defects, the agreement is excellent, demonstrating that the system indeed favours tile compositions that correspond to an eight-fold quasicrystalline symmetry. This suggest that a locking mechanism similar to the one described in section I.4.1 might also exist for the octagonal quasicrystal. The locking of the QC8 as a proper thermodynamic phase is bolstered by the observation of a fluid-QC8 coexistence in some simulations.

II.3.5 Perpendicular space analysis

As explained in subsection II.3.1, we reconstruct the tilings of the self-assembled system from the large particles bond network. The tiles obtained by joining the centres of large particles are subject to thermal fluctuation and slightly deformed. From the reconstructed noisy tiling, we then build an idealised tiling

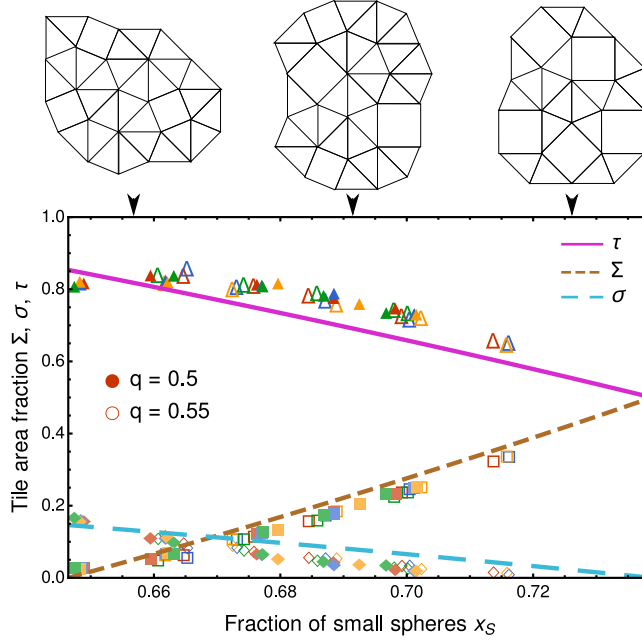


Figure II.9: Area fractions of the three different tiles in the QC8 tiling, Σ , σ , and τ , corresponding to the large squares, small squares, and triangles, respectively. The lines indicate the theoretical prediction on the assumption of a maximally symmetric and globally uniform eight-fold tiling with no defects. Points correspond to simulation results at size ratios $q = 0.5$ (full symbols) and $q = 0.55$ (open symbols). Different colours of points correspond to different packing fractions, with $0.855 \leq \eta \leq 0.87$ for $q = 0.5$ and $0.835 \leq \eta \leq 0.85$ for $q = 0.55$. For the simulation data, we only consider the area covered by non-defect tiles when calculating the composition x_S and the tile area fractions. At the top, three patches illustrate the evolution of the tilings with the composition. From left to right: primarily small squares, mixture of small and large squares and primarily large squares.

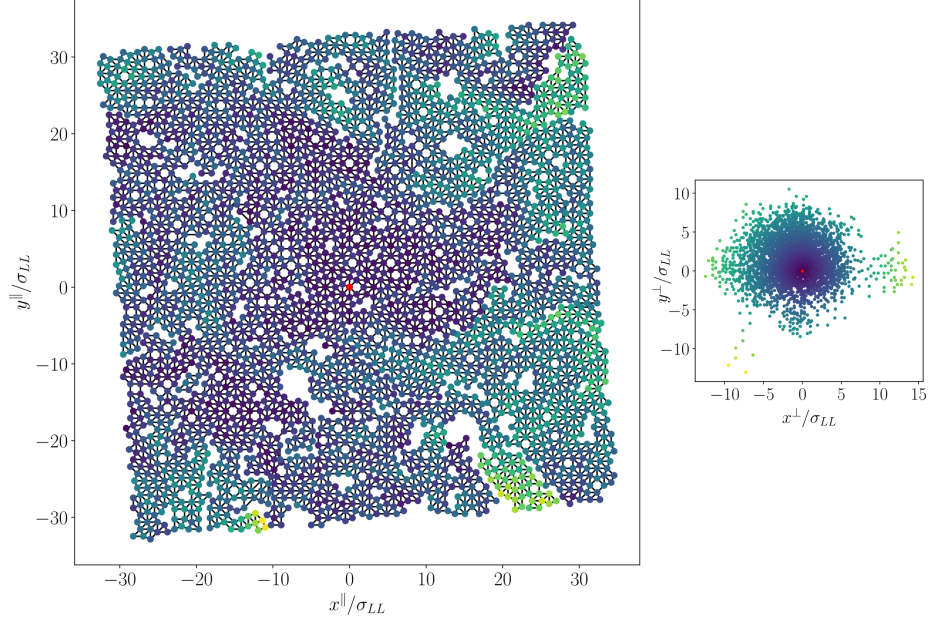


Figure II.10: Parallel (left) and perpendicular (right) projections of the lifted tiling reconstructed from the last configuration of a mixture of 10^4 non-additive hard disks with $q = 0.5$, $x_S = 0.675$, $\eta = 0.86$ and $\Delta = \Delta_{\text{plan}}$. The vertices are coloured according to their distance to the origin in the perpendicular subspace.

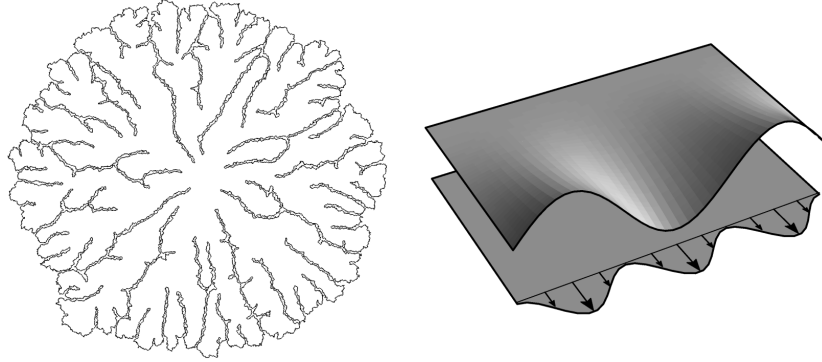


Figure II.11: (Top) Tears defects formed in a simple growth model for the QC12. (Bottom) Schematic representation of the bending of the representative hypersurface linked to the tear defects. Courtesy of Joseph and Elser, taken from Ref. 162.

where the tiles are drawn with their perfect shape, as depicted in Figure II.10-left.

The idealised tilings contain small defects that are local and do not disrupt the tiling further away, as well as long defect lines that nucleate at topological tiling defects and separate islands of tiling. Interestingly these “tears” defects were previously observed by Joseph and Elser in a simple growth model for the QC12 tiling of squares and triangles [162] (see Figure II.11-left). They interpret the tears as bending of the representative hypersurface that eventually forms several “sheets” as illustrated in Figure II.11-right.

Choosing an arbitrary origin point, every vertex in the idealised tiling can be indexed by recursively following all links and mapping them to one of the four vectors of the lift basis of subsection II.3.3. Then, the perpendicular projection of the self-assembled tiling can be obtained as shown in Figure II.10-right. In Figure II.10, we colour the vertices of the tiling according to their distance to the origin in perpendicular space. The vertices form a dense cloud around the origin in perpendicular space, which is a strong indication of the quasicrystalline nature of the system. In the parallel projection, larger distance in perpendicular space correspond to localised tiling islands, separated from the main tiling chunk by narrow bridges between two tears. This is consistent with Joseph and Elser’s interpretation of a flaky hypersurface.

The tiling in Figure II.10 was obtained after $5 \times 10^6 \tau_{\text{MD}}$ molecular dynamics time units of equilibration. Other tilings at the same state points were obtained after only $1 \times 10^6 \tau_{\text{MD}}$ time units. Although a QC8 tiling can be found in each of them, it seems that the number of defects slowly decreases, and the projection in perpendicular space gradually becomes denser as the simulation time increases. Even though we simulated our systems for long times, the high density of solid phases combined with the inherent slow dynamics of the tiling rearrangements mean that we probably did not reach the equilibrium state.

This suggests that the quasicrystal formation follows a two-step process, where first a highly defective tiling rapidly self-assembles, which then slowly anneals toward a zero-perp strain quasicrystal. This scenario was proposed by Steurer [56] for the growth of atomic quasicrystals. He suggests that the slow annealing step is energetically driven (by electron interactions in atomic quasicrystals) towards an ideal quasicrystalline ground state. However, in our purely entropic systems, there is no energy to play that role. Alternatively, Joseph and Elser suggest that bulk annealing might not be necessary if the growth of the quasicrystal is sufficiently slow [52, 162]: numerous attachment and detachment events may be sufficient for entropy to ensure a defect-free growth. Since local matching rules cannot enforce defect-free growth in two-dimensional quasicrystals [55], information transfer from the whole quasicrystal to the growing boundary is necessary. This requires an infinitely slow growth for a macroscopic quasicrystal, which does not correspond to the rapid self-assembly conditions observed which are required to observe spontaneous quasicrystal formation in our simulations. An intermediate picture, where a metastable three-dimensional dodecahedral quasicrystal grows by incorporating icosahedral clusters that pre-exist in the fluid phase close to the growing boundary was proposed in Reference

163, blurring the distinction between the first and second steps of Steurer’s scenario. We did not look specifically at the growth dynamics of self-assembling quasicrystals and thus cannot report on the possible pre-existence of stable elementary tiling units in the fluid. We note that this seems rather unlikely without energetic interactions though, as there is no cohesive force holding tiles together. Hence, our simulations seem to follow a scenario similar to the one proposed by Steurer [56], but where the defects are annealed out by entropy alone. Whether entropy favours random quasicrystal configurations or a specific ground state is unclear. This point will be addressed more precisely in Chapter III.

Moreover, since the interactions are purely repulsive, our systems must be compressed to high density to reach the solid phase. Since we use periodic boundary conditions for the simulation boxes, the self-assembled quasicrystals are frustrated. This might explain the relatively high number of defects found in the self-assembled quasicrystals. Systems with net-attractive potentials can form solid nuclei in a fluid with a free boundary, upon simple decrease of the temperature in a low density initial configuration. Quasicrystals of high quality with few defects are typically formed in this case [78, 99].

II.3.6 Simple geometrical constraints

An intriguing question remains – is there a way to understand why these octagonal quasicrystals appear in this highly simple system? As stated, the three prototiles that comprise the tiling are the small S1 square, the large S2 square, and the H1 triangle. In order to form the observed tilings, these shapes must have compatible edge lengths on their shared edges. In particular, the shared edges in the observed tilings are between the large square and the long edge of the H1 triangle, and the small square and the short edge of the H1 triangle. As shown in Figure II.12, the long edge of the triangle matches up almost exactly with the edge of a large square for size ratios between 0.5 and 0.6, in the region where we observe the self-assembly of this phase. Similarly, the short edge of the triangle and the small square match exactly for size ratios below $q = 2 - \sqrt{2} \simeq 0.59$. The fact that a QC8 with mainly small squares is not observed at size ratios below $q = 0.45$ can be understood from a packing argument. As shown in the inset of Figure II.12, when q is decreased below $1/2$, the packing fraction of the triangle tile, which makes up the majority of the QC8 phase, decreases rapidly and drops below that of competing phases, such as the simple hexagonal lattice.

We also examine here the geometrical constraints in mixtures of *additive* hard disks, which cannot overlap (i.e., the non-additivity parameter is $\Delta = 0$). The 3D equivalent of this system would consist of spheres whose centres are constrained to lie in the same plane. Figure II.13 shows the short and long edge lengths of the square and triangle tiles that can be formed with additive hard disks. While edge lengths could match for size ratios around $q = 0.6$, the inset graph shows that in this regime, the packing fraction of the tiles is systematically lower than that of hexagonal packing of large and small disks suggesting that the tiles are not dense enough to be stable in this system.

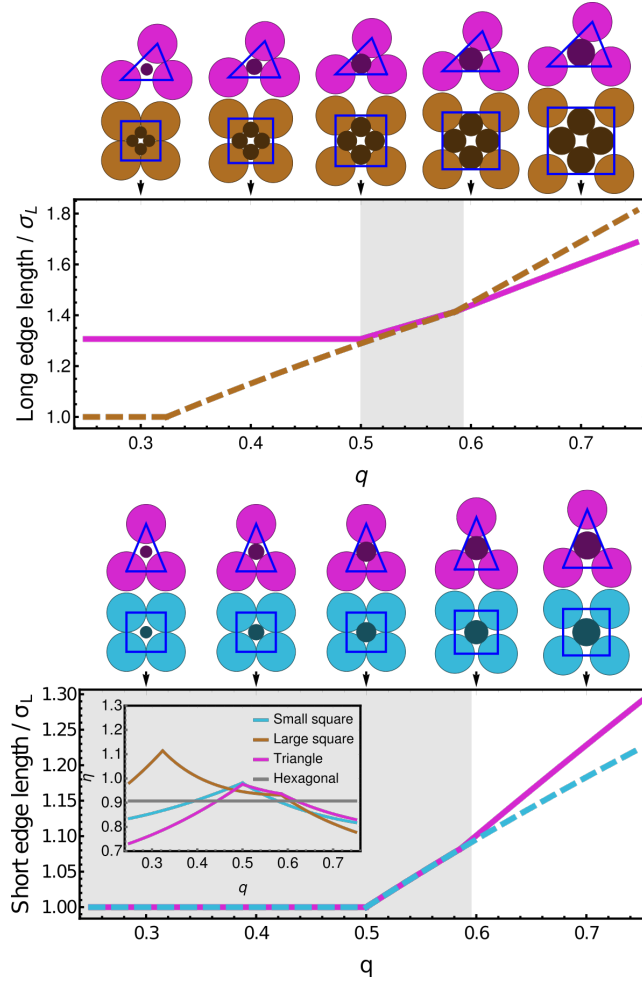


Figure II.12: Evolution of the possible long (top) and short (bottom) edge lengths as a function of size ratio. Matching regions are highlighted with a darker background. For size ratios between 0.5 and 0.6, long edges of the triangle and large square tiles on one hand, and short edges of triangle and small square tiles on the other hand match, thus allowing for the tiles that comprise the octagonal tiling to mix. The inset of the bottom graph displays the packing fraction of the three individual tiles, along with that of a coexistence of hexagonal packings of large and small particles. Self-assembly of QC8 is indeed observed for these values of the size ratio where edge lengths match and tiles pack better than Hex phases.

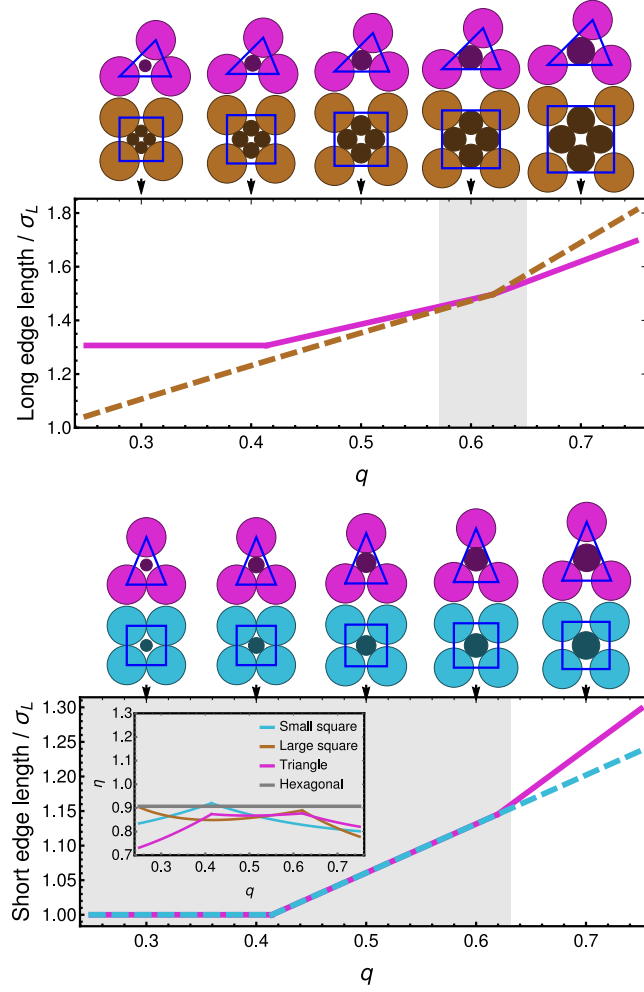


Figure II.13: Comparison of the long (top) and short (bottom) edge length of the tiles expected to form an octagonal quasicrystal in binary mixtures of *additive* hard disks. Size ratio intervals for which long or short edges match are highlighted with a darker background. The inset in the bottom graph displays the packing fraction of the various tiles as a function of size ratio, along with that of hexagonal packings.

This observation was confirmed by simulating binary additive hard disk mixtures for size ratios between $q = 0.4$ and $q = 0.6$ in steps of 0.05, packing fractions between $\eta = 0.7$ and 0.9 in steps of 0.02, and compositions ranging from $x_S = 0.6$ to 0.9 in steps of 0.05. Quasicrystal self-assembly was observed in none of these simulations, although we cannot exclude the possibility of QC8 formation in longer simulations or different parameter regimes. As suggested by the above packing argument, many of the systems instead had a tendency to demix into separate large and small hexagonal domains. This is also consistent with the sparsity of stable binary crystal structures found at infinite pressure for additive hard disks in this regime [74, 142].

II.4 Perspectives

In this Chapter, we have explored the self-assembly of binary mixtures of hard spheres on a flat plane. In addition to a variety of periodic crystals, we found that this very simple system is capable of forming two different quasicrystal structures: one dodecagonal, commonly observed in soft matter systems, and one octagonal which, to our knowledge, is described here for the first time. The octagonal quasicrystal consists of three distinct tiles, whose relative concentration can be continuously tuned by manipulating the number fraction of small spheres in the mixture, while maintaining the octagonal symmetry. Both observed quasicrystals self-assemble rapidly and reliably over a significant region of parameter space. The tiles proportions in the self-assembled octagonal quasicrystals are in remarkable agreement with theoretical predictions and their stability can be readily understood from geometrical arguments.

In contrast to most other numerical models that have been shown to form 2D quasicrystals, hard spheres on a flat plane can be easily realized experimentally on the colloidal scale, to the point of quantitative agreement between the experimental hard spheres and their ideal counterparts [106, 107].

The simplicity of the model allows us to identify minimal ingredients for quasicrystal self-assembly: dense tiles with matching edges and entropy alone are sufficient to induce the formation of quasicrystals of different symmetries. Since many colloidal particles include a repulsive spherical core, these simple ingredients might explain quasicrystal formation in a broad range of soft matter systems, beyond hard-sphere colloids alone. This identifies hard spheres on a plane as a perfect candidate system for tackling fundamental open questions on quasicrystals, such as the dynamics of their nucleation, growth and annealing, the role of their unique phason excitations or the dynamics of defects, both theoretically and in colloidal experiments on the micron scale.

The present work could be extended in several directions. First, further simple analysis could be performed on the self-assembled quasicrystals. In particular, since we already have the lifted tilings, their global perpendicular strain could easily be calculated, and would give an measure of the quality of the quasicrystalline order on large scales. Since the quasicrystals are frustrated in periodic boxes though, some residual perpendicular strain may persist, which

should decrease with the system size. Simple tiling analysis, similar to the one performed in Ref. 157 could be used to locate precisely disclinations. While we focused on the surprising QC8 in this study, similar investigation could be performed on the QC12.

For the QC12 state, Stampfli [27] and Schlottmann tilings provide ideal reference points. These quasiperiodic tilings can be generated from *inflation rules* which prescribe a scheme to replace each tile by inflated versions made of smaller tiles [28, 140, 164]. The ideal, inflated tilings have the same composition and similar local environments as the randomised version that are typically found in self-assembled tilings, but usually exhibit additional self-similarity symmetries. For the QC8, Ammann-Beenker [23, 25] and Watanabe-Ito-Soma [24] tilings are related to the extreme composition where the QC8 contains no more small squares. Preliminary results not reported here suggest that inflation schemes could be designed to generate octagonal tilings with intermediate compositions, which could serve as useful reference states to study the properties of the quasicrystal.

The entropy of the QC12 tiling – the number of configurations in the random tiling ensemble – has been both calculated from simulations, and derived exactly. As discussed in subsection I.4.1, it allows to understand the locking mechanism of the quasicrystal phase. Ergodic tiling rearrangements for the QC8 could be designed to measure the entropy of the tiling numerically, following the method developed in Reference 59. It would be interesting to see if the entropy has a cusp similar to that observed in the dodecagonal [61, 62] and another octagonal tilings [165], and explore the role of the tiling composition.

As discussed in subsection II.3.5, a satisfactory scenario for the nucleation and growth of quasicrystals driven solely by entropy is still lacking. Melting in two dimensions is notoriously tricky. For instance, Kosterlitz, Thouless, Halperin, Nelson and Young (KTHNY) have proposed a special 2D melting scenario involving two continuous transitions with an intermediate *hexatic* phase in-between the solid and the fluid [166–168]. This scenario has been partially verified for the melting transition of hard disks [107, 152, 169, 170], but it was also shown that addition of $\sim 1\%$ of a second species of disks with a different size kills the hexatic phase in favour of a first order phase transition between fluid and solid [171]. In our self-assembly simulations, we observe coexistences between a fluid and the quasicrystal, so the transition appears to be first order here.

The QC8 appears as a good candidate to study defects in quasicrystals. It exhibits disclinations whose dynamics could be followed in the reconstructed tiling. Moreover, the possibility of continuously changing the tiling composition by changing the mixture composition brings new puzzles: should a tile that appears with very small concentration be considered a defect, or a valid tile of the tiling⁶?

⁶The question also arises for the shield “defects” that are commonly observed in QC12.

The spontaneous self-assembly of dodecagonal and octagonal random tiling quasicrystals in the simple mixtures of non-additive hard disks shows that these structures are kinetically accessible. Although it is also a strong indication of their thermodynamic stability, full free-energy calculations are required to prove it. This –rather technical– endeavour will be carried out in the next Chapter.

II.5 Acknowledgements

The work presented in this Chapter benefited from fruitful discussions with Marianne Impérator-Clerc, Pavel Kalugin and Laura Filion. The main results are accessible on the ArXiv [172], and will soon be published in a peer-reviewed journal.

Chapter III

Thermodynamic stability of the dodecagonal quasicrystal

Direct self-assembly simulations provide strong indications about the phases that are kinetically accessible. However, the self-assembled phases can be metastable, in which case the system will eventually relax into its equilibrium stable phase¹. The determination of equilibrium phase diagrams requires free-energy calculations for all phases in competition.

This Chapter presents free-energy calculations for binary mixtures of hard disks, focusing on the region where the dodecagonal quasicrystal is expected. Numerical free-energy calculations are rather technical, and very often, the devil hides in the details. Therefore we tend to include more technical details than in the previous Chapters, including brief reports of failed attempts, with the aim of saving some time to future investigators.

We first discuss a mean-field cell approximation that allows us to draw a first phase diagram. Then, we resort to the more elaborate Frenkel-Ladd method to compute an essentially exact phase diagram. Finally, we use this very powerful method to investigate free-energy differences between ideal and random tiling quasicrystals, which provides a quantitative assessment of the random tiling hypothesis.

¹This might take a very long time. Anecdotally, transition from a metastable crystalline form into an other, more stable one, caused the withdrawal of Ritonavir, a medicine that was produced in one crystalline form for two years before a more stable, but less kinetically favoured one took over the production lines. See https://en.wikipedia.org/wiki/Ritonavir#Polymorphism_and_temporary_market_withdrawal.

III.1 General strategy

The general strategy for free-energy calculations in general is similar to that described in the Section I.2 of Chapter I for infinite pressure. One first identifies the relevant competing phases, then compute their free-energy, and finally uses a common tangent construction to obtain the stable phases and coexistences. At finite pressure however, two complications emerge.

First, in addition to solid structures, a fluid phase enters the arena. In a mixture, the fluid phase may exist at all compositions, which complexifies the common tangent construction, as described in this Section. The calculation of the fluid free-energy is explained in Section III.2.

Second, in addition to packing constraints which completely dictate the phase behaviour at infinite pressure, particles in a finite pressure system can move. This provides an entropy contribution that must be accounted for in the free-energy. The cell approximation, a mean-field treatment of the entropy is presented in Section III.3. Then, the essentially exact, more involved Frenkel-Ladd method is used to compute the free-energy of the solid phases in Section III.4.

III.1.1 Common tangent construction with fluid

In a system described by pressure/volume, temperature and composition, the Gibbs rule states that there can be at most P phases in coexistence with

$$P = C - F + 2, \quad (\text{III.1})$$

with C the number of components in the system and F the number of intensive variables fixed in the chosen thermodynamic ensemble. For our binary mixtures in the isobaric-isothermal (NpT) ensemble, $C = 2$ and $F = 2$, so there can be at most only $P = 2$ phases in coexistence.

In addition to the solid structures, a fluid phase can also exist at finite pressure, whose composition can vary continuously. The common tangent construction described in Section I.2.2 of Chapter I for the special case of solid phases only can be adapted to deal with the fluid. As depicted in Figure III.1, in the composition-free-energy plane at a given pressure, the solid phases are represented by points while the fluid free-energy draws a continuous line. To find the stable phases at all composition, one simply needs to draw the set of coexistence straight lines that minimises the free-energy per particle. Doing so, coexistence lines with the fluid always end-up tangent to the fluid curve.

III.1.2 State point choice

Free-energy calculations are computationally demanding. Hence we focus on binary mixtures of non-additive hard disks that correspond to the equivalent 3D geometry of spheres on a plane, with size ratio $q = 0.46$ and non-additivity parameter $\Delta \approx -0.0709$. As shown in Figure III.2, at this point, the system lies close to the low- q limit of the random tiling region at infinite pressure, where the

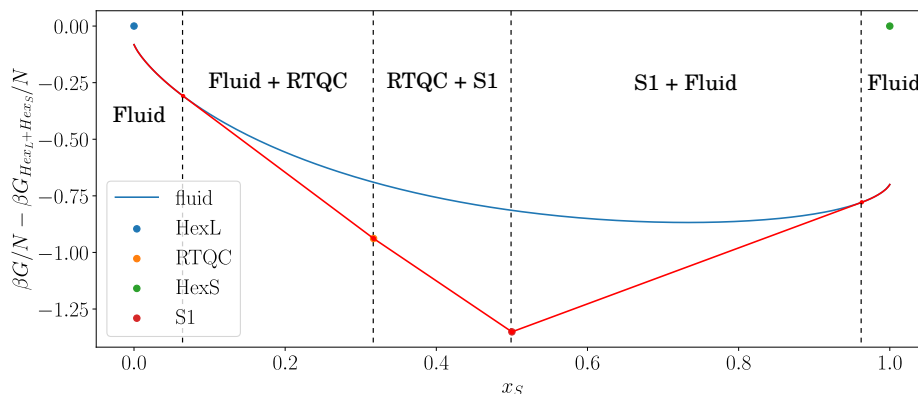


Figure III.1: Common tangent construction (red line) for a mixture of non-additive hard disks at pressure $11 k_B T \sigma^{-2}$. Solid phases are represented by single points at their composition while the fluid can exist for the full range of compositions. The free-energy of the $\text{Hex}_L + \text{Hex}_S$ coexistence has been subtracted on the y-axis for clarity. The black labels signal the stable phase or coexistence for each composition. Solids and fluid free-energies are obtained from the cell approximation and thermodynamic integration of Santos [173] equation of state respectively (see next Sections).

dodecagonal random tiling quasicrystal is expected (see Chapter I). We expect that keeping small particles as small as possible might help them escape the S1 squares centre, which should ease tiles rearrangement and speed-up the random tiling dynamics.

The chosen state point lies within the region where the dodecagonal quasicrystal is found to spontaneously self-assemble in simulations as was shown in Figure II.3. We limit the free-energy investigation to the region relevant to this quasicrystal which is related to quasicrystals observed in many other soft matter systems [38, 49, 50, 82, 84, 85, 87, 88, 91, 94–96, 157–159], and leave aside for now the more complicated and exotic octagonal quasicrystal. Hence, we will only consider mixtures with small particle concentrations $x_S \leq 1/2$.

We draw relevant competing phases for the phase diagram construction from the results of our infinite pressure and self-assembly studies presented in the previous Chapters. In addition to the fluid, we consider the hexagonal close packings of large and small spheres Hex_L and Hex_S , the S1 square phase, the quasicrystal and its first periodic approximant called the sigma-phase.

III.2 Fluid free energy

The standard method to compute the free-energy of fluids is the so-called *thermodynamic integration* of an equation of state.

III.2.1 Thermodynamic integration

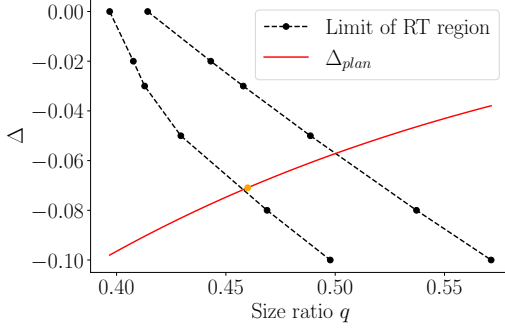


Figure III.2: Non-additivity parameters that correspond to spheres-on-plane geometry (red line). The orange point highlights the size ratio chosen for free-energy calculations, at the low- q boundary of the *infinite pressure* random tiling region (dashed lines).

In the canonical ensemble, the pressure p is related to the Helmholtz free energy F by

$$\left(\frac{\partial \beta F / N}{\partial \rho} \right)_{N,T} = \frac{\beta p}{\rho^2}, \quad (\text{III.2})$$

with $\rho \doteq N/V$ the particles density, $\beta \doteq (k_B T)^{-1}$, k_B the Boltzmann constant and T the temperature.

The general idea of thermodynamic integration is to integrate equation III.2 to obtain the free-energy difference between the system at a reference density where the free-energy is known and the density of interest [174]. This assumes that no first-order phase transition takes place along the integration path. In

general, for fluid states, the ideal gas provides a good reference state in the limit $\rho \rightarrow 0$.

Applying equation III.2 to the excess free energy (free-energy difference with the ideal gas) of a binary mixture gives

$$\frac{\partial \beta(F - F^{\text{id}})/N}{\partial \rho} = \frac{\beta(p - p^{\text{id}})}{\rho^2}, \quad (\text{III.3})$$

where $\beta F^{\text{id}}/N = \ln(\rho \Lambda_T^2) - 1 + x_S \ln(x_S) + (1 - x_S) \ln(1 - x_S)$ is the free energy of the binary ideal gas mixture. $\Lambda_T \doteq \sqrt{2\pi \hbar^2 \beta m^{-1}}$ is the thermal wavelength with \hbar the reduced Plank's constant and m the mass of the particles, taken equal for both species without loss of generality for the equilibrium properties. Then we integrate up to target density ρ . The boundary term at $\rho = 0$ of the left-hand-side vanishes since in this limit, the mixture of hard disks becomes an ideal gas:

$$\begin{aligned} \frac{\beta F(\rho)}{N} - \frac{\beta F^{\text{id}}(\rho)}{N} &= \int_0^\rho d\rho' \beta \frac{p - p^{\text{id}}}{\rho'^2} \\ \frac{\beta F(\rho)}{N} &= \ln(\rho \Lambda_T^2) - 1 + x_S \ln(x_S) + (1 - x_S) \ln(1 - x_S) \\ &\quad + \int_0^\rho \frac{d\rho'}{\rho'} \left(\frac{\beta p}{\rho'} - 1 \right). \end{aligned} \quad (\text{III.4})$$

The first four terms on the right-hand-side correspond to the free-energy of the two-components perfect gas at density ρ and composition x_S , including the mixing entropy term². In the following, we set $\Lambda_T = \sigma_L$ which amounts to fixing the particle mass. Since the particle mass has no impact on the equilibrium phase behaviour, this arbitrary choice does not affect the generality of the calculations.

The Gibbs free-energy G is obtained from the Helmholtz free-energy F by simply adding a pressure term where $\rho(p)$ is the inverted equation of state:

$$\frac{\beta G(N, p, T)}{N} = \frac{\beta F(N, V, T)}{N} + \frac{\beta p}{\rho(p)}. \quad (\text{III.5})$$

To compute the integrand in the last term of equation III.4 one needs an equation of state $p(\rho)$. It can be obtained from an approximate analytical expression, or directly measured in computer simulations.

III.2.2 Obtaining an equation of state

Approximate analytical expression

For many systems, analytical expressions for the equation of state in the fluid range have been determined. They are usually easily integrated with simple numerical schemes and computationally cheap to evaluate. The main drawback is that analytical equations of state are almost always approximate, and usually do not perform well at high densities close to freezing.

An approximate analytical equation of state for mixtures of non-additive hard spheres in dimension d has been derived by Santos, de Haro and Yuste (SHY) [173]. We report here the closed expression for the specific case of binary mixtures in dimension 2 which is not completely trivial to obtain from the general expressions:

$$\begin{aligned} \frac{\beta p^{\text{SHY}}}{\rho} = 1 + \frac{\eta}{1 - \eta} \frac{b_3 \langle \sigma^2 \rangle \bar{B}_2 - b_2 \bar{B}_3}{(b_3 - b_2) \langle \sigma^2 \rangle^2} \\ + (Z_{\text{pure}}(\eta) - 1) \frac{\bar{B}_3 - \langle \sigma^2 \rangle \bar{B}_2}{(b_3 - b_2) \langle \sigma^2 \rangle^2}. \end{aligned} \quad (\text{III.6})$$

with $\langle \sigma^2 \rangle \doteq x_S \sigma_S^2 + (1 - x_S) \sigma_L^2$ and $\eta \doteq \pi \rho \langle \sigma^2 \rangle / 4$ the packing fraction. $b_2 \doteq 2$ and $b_3 \doteq 16/3 - 4\sqrt{3}/\pi$ are the second and third reduced virial coefficients of the one-component hard-disk fluid. $\bar{B}_n \doteq (4/\pi)^{n-1} B_n$ with B_n the n^{th} virial coefficient of the non-additive binary mixture. The second and third virial

²The mixing entropy term has infinite derivatives at $x_S = 0$ or 1. This turns out to be very important for common tangent constructions near those extreme values.

coefficients of the mixture are given by

$$\begin{aligned} B_2 &= \frac{\pi}{2} [\sigma_{LL}^2(1-x_S)^2 + 2\sigma_{LS}^2x_S(1-x_S) + \sigma_{SS}^2x_S^2] \\ B_3 &= \left(\frac{\pi}{4}\right)^2 [\bar{B}_{LLL}(1-x_S)^3 + 3\bar{B}_{LSS}x_S^2(1-x_S) \\ &\quad + 3\bar{B}_{LLS}x_S(1-x_S)^2 + \bar{B}_{SSS}x_S^3], \end{aligned} \quad (\text{III.7})$$

with

$$\bar{B}_{iii} = b_3\sigma_i^4 \quad (\text{III.8})$$

$$\bar{B}_{ij} = b_3\sigma_i^4 \mathcal{B}\left(\frac{\sigma_{ij}}{\sigma_{ii}}\right) \quad (\text{III.9})$$

$$\mathcal{B}(s) = \frac{4}{3\pi b_3} \left[4\pi s^4 - 8s^2(s-1) \arccos\left(\frac{1}{2s}\right) - (2s^2+1)\sqrt{4s^2-1} \right] \quad \text{for } s \geq \frac{1}{2}. \quad (\text{III.10})$$

Note that the condition $s \geq \frac{1}{2}$ is always satisfied in our system. Finally, $Z_{\text{pure}}(\eta)$ is the compressibility factor of a one-component hard disk fluid at the same packing fraction as the mixture. Here, we use Henderson's equation of state [175], given by

$$Z_{\text{pure}}(\eta) = \frac{1 + \eta^2/8}{(1 - \eta)^2}, \quad (\text{III.11})$$

which is quite accurate for monodisperse hard disks. The SHY equation of state for $x_S = 0.3$ is depicted in Figure III.3-Left as a continuous blue line. The Gibbs free-energy obtained after thermodynamic integration is plotted in Figure III.3-Right as dotted lines for three different pressures.

Simulated equation of state

Alternatively, the equation of state can be directly measured in simulations. This approach is much more computationally demanding, but yields essentially exact results (up to finite size and simulation length effects).

We measure the equation of state in isobaric-isothermal (NpT) Monte Carlo simulations [145, 146] with a total of $N = 2000$ particles. The simulations are run in two steps. First the system is randomly initialised at low density, and 5×10^5 MC sweeps are performed at the target pressure, while MC moves amplitudes are adapted every 500 MC sweeps to match target rejection rates³. This results in a rapid compression. Then, the moves amplitudes are frozen, and 5×10^5 MC sweeps are performed, during which the density is measured.

For each composition between compositions $x_S = 0$ and $x_S = 1$ with step size $\delta x_S = 100/2000 = 0.05$, we sample the equation of state in at

³We target a rejection rate of 0.7 for particles translation moves and 0.8 for box scaling moves. In hard particles systems, any overlap results in rejection. This makes rejection computationally cheap, and the optimal rejection rate is therefore typically larger than the generally assumed value of 0.5 [176]. Preliminary benchmark simulations are used to determine good rejection rates.

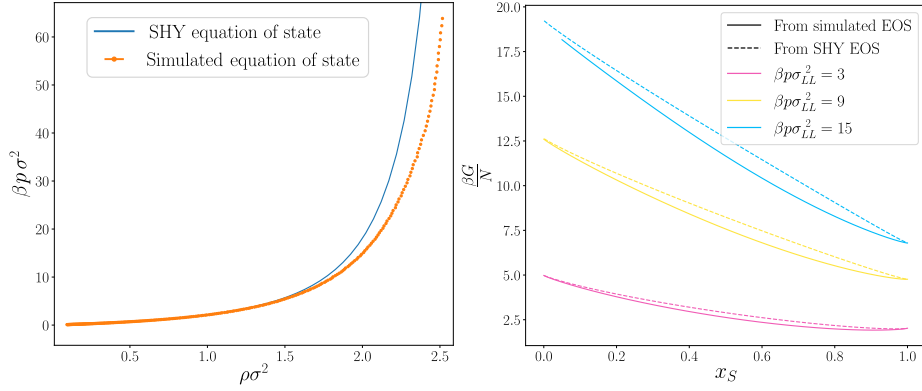


Figure III.3: (Left) Equation of state of a binary mixture of non-additive hard disks at $q = 0.46$, $\Delta = -0.0709$ and $x_S = 0.3$. The continuous line is the SHY approximate analytical expression derived in Ref. 173, while the orange points are direct measurements in NpT Monte Carlo simulation of 2000 particles. (Right) Gibbs free-energy at three different pressures obtained from thermodynamic integration of simulated and SHY equations of state (solid and dashed lines respectively).

least 250 pressures logarithmically distributed between $p_{\min} = 0.1 k_B T \sigma_{LL}^{-2}$ and p_{\max} . Monodisperse hard disks crystallise at a pressure of about $9 k_B T \sigma_{LL}^{-2}$ [177, 178]. Hence our systems will freeze at $p \sim 9 k_B T \sigma_{LL}^{-2}$ when $x_S = 0$ and at $p \sim 9 k_B T \sigma_{SS}^{-2} = 9 q^{-2} k_B T \sigma_{LL}^{-2} \sim 45 k_B T \sigma_{LL}^{-2}$ when $x_S = 1$. At intermediate compositions, the freezing pressure is unknown, so we set the maximum pressure at $\beta p_{\max} \sigma_{LL}^2 = 35 x_S + 15$ which linearly interpolates between two points located above the monodisperse freezing pressures. At some compositions, extra points at larger pressures were sampled. In total, 5770 simulations were performed.

The integrand of equation III.4 can be rewritten as a virial expansion

$$I(\rho) = \frac{1}{\rho} \left(\frac{\beta p}{\rho} - 1 \right) = \sum_{k=2}^{\infty} B_k \rho^{k-2} \quad (\text{III.12})$$

The integrand is computed from the simulated equations of state at each composition and fitted with a polynomial of degree 8 to 12 depending on the composition. After numerical integration we obtain the Gibbs free-energy of the fluid as a function of pressure for each sampled composition. Finally, to perform the common tangent construction a fixed pressure, we compute the Gibbs free-energy using the fitted expressions at each composition and fit again to obtain a smooth free-energy as a function of composition for a given pressure.

The fitting of the integrand is quite critical and requires some care. Because the pressure increases very quickly with density, a linear sampling in pressure tends to result in a very dense sampling of high densities, which leads to a poor fit with oscillations in the low density regime. We find that a logarithmic

sampling of pressures is much better. To further improve fitting at low density, we compute the exact second and third Virial coefficients in equation III.12 using expressions III.7 from Ref. 173.

The measured average density at each pressure comes with a statistical uncertainty owing to the finite length of the simulations. Hence, we have error bars on both ρ and $I(\rho)$. However, least squares fitting by construction can only take into account y-error bars. We observed that better fits were obtained by using orthogonal distance regression instead, which can weight the contribution of each fitted point according to both y and x error bars.

To assess the magnitude of finite size effects, we repeated the thermodynamic integration at composition $x_S = 0.5$ using equations of state measured in systems of $N = 250, 500$ and 1000 particles. We estimate that the finite size error on the final Gibbs free-energy for the fluid is at most of the order of $10^{-2}k_B T/N$.

Likewise, we assess the error coming from the choice of the order of the fitting polynomial by repeating the procedure with larger and smaller values, and estimate an error of the order of $10^{-3}k_B T/N$.

At each composition, some of the sampled pressures lie beyond the freezing point. Because of the fast compression, we observe no crystallisation, but instead end-up in a glassy, super-compressed metastable fluid. The very slow dynamics in this regime combined with the finite duration of our simulations cause additional errors which we estimate by repeating again the procedure with 10 times as long production runs for the equation of state sampling. We find that the resulting error is again of the order of $10^{-3}k_B T/N$. Hence, overall, finite size effects appear to dominate the error on the calculated Gibbs free-energy, which is at most of the order of $10^{-2}k_B T/N$.

In Figure III.3-Right, we compare the fluid Gibbs free-energies computed from the approximate SHY (dashed lines) and simulated (solid lines) equations of state. Both yield similar values close to the extreme regimes $x_S = 0$ or 1 where the system is almost monodisperse. For intermediate compositions however, using the analytical equation of state overestimates the free-energy. The discrepancy increases with pressure, which is expected since the SHY equation of state becomes less accurate at larger densities.

III.3 Cell approximation

While very useful for fluids, thermodynamic integration alone does not usually work for solids because there is no equivalent of the perfect gas reference state from which to integrate without crossing a phase transition.

In this Section, we use a mean-field approach called the *cell approximation* to compute the free energy of solids [179–181]. It allows us to map out a first approximate phase diagram of our system. A similar approach has been used by Wheatley to compute the phase diagram of binary mixtures of additive hard disks [182].

III.3.1 General setting

Consider a 2D solid of N particles occupying n types of non-equivalent sites. Let N_i be the number of particles occupying a site of type i . We assume that each particle is trapped in a cage formed by its nearest neighbours sitting at their ideal lattice sites. This is a mean-field approximation: all sites of a given type are equivalent and thus the partition function can be factorised:

$$\begin{aligned} Z &\approx \frac{1}{\Lambda_T^{2N}} \prod_{j=1}^n \left(\int d\vec{r} e^{-\beta U_j(\vec{r})} \right)^{N_j} \\ &= \frac{1}{\Lambda_T^{2N}} \prod_{j=1}^n A_j^{N_j}, \\ \text{with } A_j &\doteq \int d\vec{r} e^{-\beta U_j(\vec{r})}. \end{aligned} \quad (\text{III.13})$$

U_j is the potential felt by the central particle rattling around a site of type j , caged by its nearest neighbours. Then the free energy reads

$$\begin{aligned} -\beta F &= \ln Z \\ &= -2N \ln \Lambda_T + \sum_{j=1}^n N_j \ln A_j. \end{aligned} \quad (\text{III.14})$$

Let $\phi_j = \lim_{N \rightarrow \infty, N_j \rightarrow \infty} N_j/N$ be the fraction of sites of type j in the solid. Then

$$\frac{\beta F}{N} \approx \sum_{j=1}^n \phi_j \ln \left(\frac{\Lambda^2}{A_j} \right). \quad (\text{III.15})$$

And the pressure is given by

$$\frac{\beta p}{\rho} = \rho \frac{\partial \beta F/N}{\partial \rho} = -\rho \sum_{j=1}^n \frac{\phi_j}{A_j} \frac{\partial A_j}{\partial \rho}. \quad (\text{III.16})$$

As a –surprising– sanity check we can consider a perfect gas, for which there is only one type of site with $A(\rho) = 1/\rho$. Then, $\beta p/\rho = 1$ as expected. In fact, as discussed in Ref. 179 the perfect gas is the case for which the cell approximation is the worst. Indeed, equation III.15 yields a Helmholtz free-energy per particle of $\ln(\rho \Lambda_T^2)$ instead of $\ln(\rho \Lambda_T^2) - 1$ so the error on the total free energy scales with N and diverges in the thermodynamic limit. However, this huge error does not depend on the volume and therefore the equation of state is not affected.

In the special case of hard disks, A_j is simply the accessible volume for the central particle in site j . The cell approximation is obviously no longer valid when the spacing between particles of the cage becomes large enough to let the central particle escape.

III.3.2 Application to our solid phases

Hexagonal solid

There is only one type of site in the hexagonal solid, as depicted in Figure III.4. Let L be the lattice parameter and σ the particles diameter. Then

$$\rho \doteq \frac{N}{V} = \frac{2}{L^2\sqrt{3}}, \quad \text{so} \quad L = \sqrt{\frac{2}{\sqrt{3}\rho}}. \quad (\text{III.17})$$

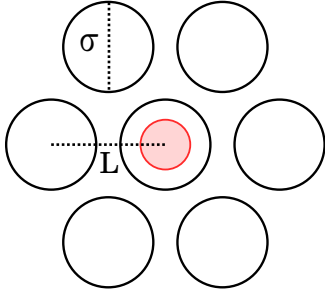


Figure III.4: The one and only type of site in the hexagonal solid. We approximate the volume accessible to the central particle by the pink disk.

We approximate the accessible volume for the central particle A_{hex} by a disk. It then reads

$$A_{\text{hex}}(\rho) \approx \pi(L - \sigma)^2 = \pi \left(\sqrt{\frac{2}{\sqrt{3}\rho}} - \sigma \right)^2. \quad (\text{III.18})$$

The maximum density is achieved when all disks are in contact, *ie.* $L = \sigma$, so $\rho_{\text{max}} = 2/(\sigma^2\sqrt{3})$. When $L = 2\sigma$, the spacing between particles is large enough to let the central particle escape and the cell approximation is no longer valid. Therefore $\rho_{\text{min}} = 1/(2\sqrt{3}\sigma^2)$. For densities ρ between ρ_{min} and ρ_{max} , the cell approximation yields the following approximate Helmholtz free energy.

$$\frac{\beta F(\rho)}{N} \approx \ln \left(\frac{\Lambda_T^2}{A_{\text{hex}}(\rho)} \right) = 2 \ln \left(\frac{\Lambda_T}{\sqrt{\frac{2}{\sqrt{3}\rho}} - \sigma} \right) - \ln \pi \quad (\text{III.19})$$

Then, adding the pressure term obtained from equation III.16, we can compute the Gibbs free energy.

$$\frac{\beta G_{\text{Hex}}}{N} = 2 \ln \left(\frac{\Lambda_T}{\sqrt{\frac{2}{\sqrt{3}\rho}} - \sigma} \right) - \ln \pi + \frac{1}{1 - \sqrt{\frac{\sqrt{3}\rho}{2}}\sigma} \quad (\text{III.20})$$

It can be expressed in terms of p by solving for ρ in equation III.16 and replacing. In our binary systems, since we measure lengths in large disk diameters, we take $\sigma = \sigma_{LL}$ for hexagonal solid of large particles and $\sigma = q\sigma_{LL}$ for hexagonal solid of small ones. To compute actual values, without loss of generality, we set $\Lambda_T = \sigma_{LL}$ which fixes particles mass. This does not affect the equilibrium phase behaviour.

S1 solid

There are two types of sites in the S1 crystal as depicted in Figure III.5. They both appear with the same frequency $\phi_1 = \phi_2 = 0.5$.

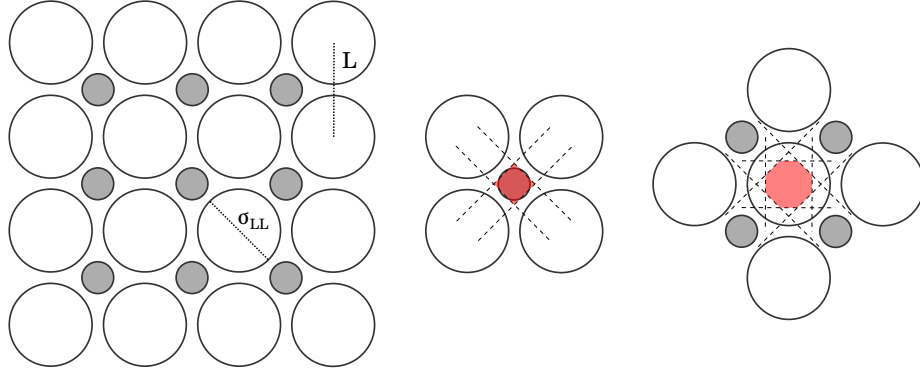


Figure III.5: The two types of site of the S1 solid. The volume accessible to the central particle is approximated by the Voronoi cell highlighted in pink.

Let L be the lattice parameter. $\rho = 2/L^2$ so $L = \sqrt{2/\rho}$. The minimum density is achieved when the small disk can escape the cage of large ones, *ie.* $L = (1+q)(1+\Delta)\sigma_{LL}$. So $\rho_{\min} = 2/((1+q)(1+\Delta)\sigma_{LL})^2$. The maximum density is achieved when $L = \sigma_{LL}$ (large disks in contact) or $L = (1+q)(1+\Delta)\sigma_{LL}/\sqrt{2}$ (large and small disks touching along the square diagonal). The first case occurs for $q < \sqrt{2}/(1+\Delta) - 1$ and the second for larger q 's. The discriminating value corresponds to a magic ratio of S1. The maximum densities read respectively $\rho_{\max} = 2/\sigma_{LL}^2$ or $\rho_{\max} = 4/((1+q)(1+\Delta)\sigma_{LL})^2$.

We now need to compute the contribution to the free energy and pressure contributions of both sites. For this, we approximate the accessible volume to the central large disk by its Voronoi cell.

For type 1 sites occupied by small particles, the accessible volume is given by

$$\rho A_1(\rho) = ((1+\Delta)\sqrt{\rho}\sigma(q+1) - 2)^2 \quad (\text{III.21})$$

which yields the Gibbs free-energy contribution of type 1 sites

$$\frac{\beta G_1}{N} = \frac{0.5 \left((1+\Delta)\sqrt{\rho}\sigma(q+1) - 2 \right) \ln \left(\frac{\Lambda^2 \rho}{((1+\Delta)\sqrt{\rho}\sigma(q+1) - 2)^2} \right) - 1}{(1+\Delta)\sqrt{\rho}\sigma(q+1) - 2}. \quad (\text{III.22})$$

For type 2 sites, occupied by large particles, two shapes are possible for the accessible volume. When the closest neighbour is a large disk, the accessible volume is a square of area

$$\rho A_2^{(LL)}(\rho) = 4(\sqrt{\rho}\sigma - \sqrt{2})^2. \quad (\text{III.23})$$

When a small disk is encountered before a large one, the Voronoi cell has the shape depicted in Figure III.5-Right and its volume reads

$$\begin{aligned} \rho A_2^{(LS)}(\rho) = & 4(\sqrt{\rho}\sigma - \sqrt{2})^2 \\ & - [2 + 2\sqrt{2}(\sqrt{\rho}\sigma - \sqrt{2}) - (1+\Delta)\sqrt{\rho}\sigma(q+1)]^2. \end{aligned} \quad (\text{III.24})$$

The two corresponding curves cross at $\rho_c \sigma^2 = 8/(\sqrt{2}(1 + \Delta)(1 + q) - 4)^2$. As can be seen in Figure III.6, the accessible volumes in both regimes have the same derivatives at the crossing point. Earlier attempts with cruder approximations for the accessible volumes did not have this property and resulted in an unphysical jump of the pressure between the two regimes.

The resulting Gibbs free-energy of the type 2 sites is easily derived from the volume expressions above. Finally, the total Gibbs free-energy of the S1 solid is obtained as $\beta G_{S1}/N = 0.5\beta G_1/N + 0.5\beta G_2/N$.

Dodecagonal quasicrystal

In the QC12 tiling, large particles can occupy four types of sites (up to different orientations, see Figure III.7) while small particles always occupy the same S1 square sites. Instead of computing the free energy of each site with the cell approximation, we rely on the random tiling hypothesis which assumes that all realisations of the random tiling are essentially equally likely. We can then obtain the free energy of the random tiling quasicrystal as the free energy of any one tiling configuration in the ensemble with an extra term accounting for the tiling entropy.

$$\frac{\beta G_{RTQC}}{N} = \frac{\beta G_{\text{conf}}}{N} - \frac{S_{RT}}{k_B N}. \quad (\text{III.25})$$

From the free energies of the hexagonal and S1 solids, we can easily obtain the free energy of their coexistence and use the coexistence at the quasicrystal composition as our reference tiling configuration:

$$\frac{\beta G_{\text{Hex}_L + \text{S1}}(x_S)}{N} = 2 \frac{\beta(G_{\text{S1}} - G_{\text{Hex}_L})}{N} x_S + \frac{\beta G_{\text{Hex}_L}}{N}. \quad (\text{III.26})$$

As discussed in Section I.4 of Chapter I, the square-triangle tiling entropy has been determined exactly [62]. It reaches a maximum value of $[\ln(108) - 2\sqrt{3} \ln(2 + \sqrt{3})](1 - x_S^{\text{RTQC}}) \approx 0.082 k_B$ per particle at the quasicrystal composition $x_S^{\text{RTQC}} = \sqrt{3}/(2 + 2\sqrt{3}) \approx 0.317$.

We see right away that the random tiling hypothesis cannot be fully correct here. Indeed, not all configurations in the random tiling ensemble have the same proportion of each types of site. In particular, the $\text{Hex}_L + \text{S1}$ coexistence does not have any of the last two sites depicted in Figure III.7.

Moreover, as already noted in Section I.4, it is not possible to realise a phase-separated coexistence of Hex_L and S1 without a defective grain boundary [140].

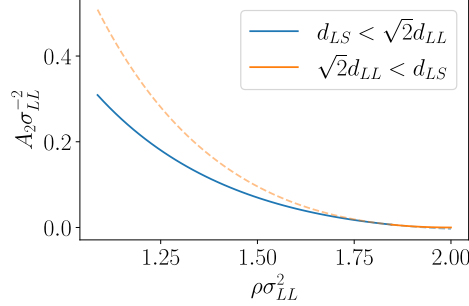


Figure III.6: Accessible volume for type 2 sites of the S1 solid for $q = 0.46$ and $\Delta = -0.709$. The crossover between two regimes has a continuous derivative.

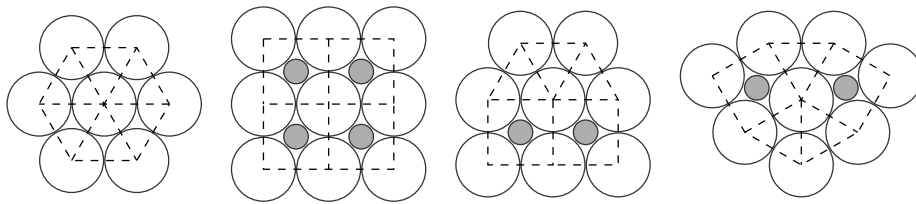


Figure III.7: The four types of sites for the large particles in the random tiling of squares and triangles.

Thus, strictly speaking, the $\text{Hex}_L + \text{S1}$ reference configuration we chose does not even belong in the random tiling ensemble.

However, as we will see later in Section III.5, the random tiling hypothesis is a good approximation in our system. The cell approach developed here is itself a quite strong and uncontrolled approximation. Therefore, we assume that in spite of these caveat, this cell approach is good enough to give a first rough idea of the phase behaviour of our system.

III.3.3 Approximate phase diagram

We now have all the ingredients to compute a first phase diagram for our binary mixtures of non-additive hard disks with $q = 0.46$ and $\Delta = -0.0709$. We perform common tangent constructions as explained in Section III.1.1 for hundreds of pressures using the Gibbs free energy obtained from SHY equation of state for the fluid, and cell approximation for the hexagonal, S1 and random tiling quasicrystal solids. The resulting phase diagram is displayed in Figure III.8.

We first note that for compositions above $x_S = 0.5$, this phase diagram is not reliable. Indeed, we know from the infinite pressure study that the H3 phase (see Figure II.2) as well as the octagonal quasicrystal described in Section II.3 should be considered but were ignored here to focus on the dodecagonal quasicrystal. Moreover, the (composition dependent) tiling entropy of the octagonal quasicrystal is not known. Hence, an accurate determination of the phase diagram for $x_S > 0.5$ would require significant additional work.

In the relevant range of compositions, we find that all candidate phases are stable, including the random tiling quasicrystal. At high pressures, we recover the infinite pressure limit behaviour and at smaller pressures, various coexistences with the fluid appear. In particular, below the quasicrystal composition, we find a region of coexistence between the fluid and the quasicrystal. In this region, the high mobility of the fluid could help equilibrating the quasicrystal and annealing out the tiling's defects. However, in self-assembly simulations, we instead typically observe that the quasicrystal coexists with a fluid and anneals better with a higher concentration of small disks.

Experience suggests that the cell approximation is rather reliable when comparing solid free energies, but performs quite badly when predicting coexistence with a fluid. Hence the present phase diagram should be taken with a grain of

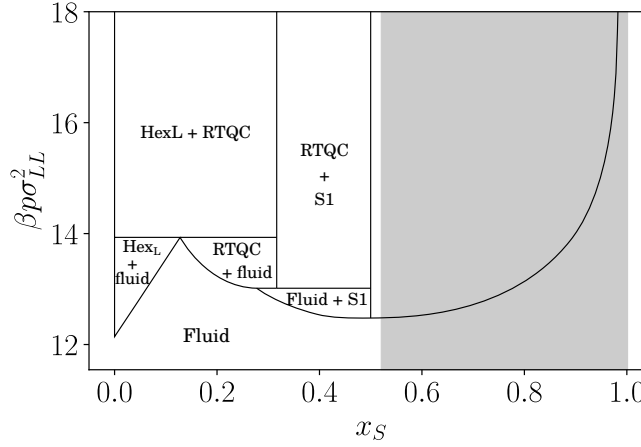


Figure III.8: Phase diagram determined from the cell approximation for a binary mixture of non-additive hard disks with $q = 0.46$ and $\Delta = -0.709$. Missing phases make the phase diagram unreliable for compositions larger than $x_S = 0.5$. The random tiling quasicrystal, labelled as RTQC, is found stable among the other periodic solid phases.

salt in the freezing regions. In particular, at $x_S = 0$, the one-component fluid of hard disks is predicted to freeze at a pressure of about $12.5 k_B T \sigma_{LL}^{-2}$ which is quite far from the value of $9.18 k_B T \sigma_{LL}^{-2}$ known from hard disks simulations [177, 178]⁴.

Yet, this first rough phase diagram shows that we can expect the dodecagonal quasicrystal to be thermodynamically stable at finite pressures. For a more precise investigation, we need a more reliable determination of the free energies.

III.4 Frenkel-Ladd method

In 1984, Frenkel and Ladd proposed a method that is now considered the Rolls Royce of free-energy calculation methods [183]. Indeed, it allows to compute the free energy of solids (ordered or not) to an accuracy only limited by the amount of computing power one is willing to invest. The so-called Frenkel-Ladd method has been used in a huge variety of systems and has become de-facto standard for precise free-energy calculations. In particular, it was used to establish that the FCC crystal of hard spheres is more stable than the competing HCP stacking in the close packed limit by a tiny free-energy difference of $0.001164(8) N k_B T$ per particle [136]⁵.

⁴We note however that at $x_S = 1$ the monodisperse fluid of small disks is predicted to freeze at a pressure of about $58 k_B T \sigma_{LL}^{-2} \approx 12.3 k_B T \sigma_{SS}^{-2}$. The one-component fluids on both ends of the phase diagram freeze at the same reduced pressure which is a good sanity check.

⁵In fact, the development of the method was partly motivated by this question. Hard spheres are taken as an example for the method in the original paper by Frenkel and Ladd

The power of the method comes at the price of some technicality. Thus, in this Section, we describe the method in details and present some critical aspects of our implementation. Then, we use it to map out an essentially exact phase diagram of our non-additive binary hard disk mixtures.

III.4.1 The method

The general idea is to start from a reference system whose free energy is known, and then gradually transform it into the system of interest by a combination of explicit free-energy differences calculations and Hamiltonian integration. In contrast to thermodynamic integration discussed in Section III.2.1, the parameters of the Hamiltonian are varied along the transformation path instead of the thermodynamic parameters. This allows for a wider variety of integration paths. Note that in order for the free-energy calculation to be accurate, the chosen integration path should not cross any first-order phase boundaries.

Since its original description [183], several variants of the Frenkel-Ladd method have been developed, using different reference states or integration methods [174, 184–187]. Here we use the so-called *Einstein molecule* approach developed by Vega and Noya [186]. It is simpler than the original approach and an excellent review can be found in Ref. 174. We report here the main steps for the specific case of binary non-additive hard disk mixtures.

The reference system is the *ideal Einstein molecule* in which all particles but one are tight to their lattice site by harmonic springs. The particle that is not attached to a spring (say particle 1, without loss of generality) is called the carrier and defines the lattice. The potential energy of the system is then

$$U_{\text{ein-mol-id}}(\vec{r}_1, \vec{r}_2, \dots, \vec{r}_N) = \gamma \sum_{i=2}^N (\vec{r}_i - \vec{r}_{i_0}(\vec{r}_1))^2. \quad (\text{III.27})$$

Notice that the sum starts at 2, so the carrier can move freely. The lattice site positions are functions of the position of the carrier since the lattice moves with it. γ is the stiffness of the springs.

The ideal Einstein molecule is first transformed into an *interacting Einstein molecule* with the hard repulsion between particles added on top of the springs. Then, the springs are gradually turned off to transform the system into the target hard disk mixture.

Drifts of the whole solid lead to a quasi-divergence of the integrand in the Hamiltonian integration. This can be avoided by fixing the position of one of the particles in the system. In the Einstein molecule, this is easily done by fixing the position of the carrier, which is the reason for choosing such a strange reference system to start with. Fixing a particle's position comes with an extra free-energy contribution that needs to be accounted for, but allows to keep the numerical method stable.

Overall, the transformation path is the following:

[183], but at the time, the available computing resources were not sufficient to settle the competition between FCC and HCP packings.

- Start from an ideal Einstein molecule at the desired packing fraction. Its free energy $F_{\text{ein-mol-id}}$ can be computed analytically.
- Transform it into an ideal Einstein molecule *with one particle fixed*. The free-energy difference due to fixing the carrier can be computed analytically, and turns out to not play a role. In the following, a star superscript indicates that one particle is fixed in the system.
- Add the hard core interaction on top of the springs to get an interacting Einstein molecule. The resulting free energy $F_{\text{ein-sol}}^*$ (the “sol” subscript stands for “solid”) can be obtained from an average calculation in a simulation.
- Gradually turn off the springs and perform a Hamiltonian integration to get the free energy F_{sol}^* of the solid with one particle fixed.
- Free the fixed particle to get the free energy F_{sol} of system of interest.

After this procedure, we get the Helmholtz free-energy of the solid at a given packing fraction. The Gibbs free-energy is computed by adding $\beta p/\rho$ that can be obtained from a simulated equation of state.

In the following, we derive the expressions for the free-energy calculation of a binary mixture with N_1 particles of type 1 and N_2 particles of type 2. We assume that the carrier is a particle of type 1.

Free-energy of the ideal Einstein molecule

The free-energy of the ideal Einstein molecule can be computed analytically. After integration over the momentum degrees of freedom, the partition function of the ideal Einstein molecule reads

$$\begin{aligned} Z_{\text{ein-mol-id}} &= \frac{1}{N_1!} \frac{1}{N_2!} \frac{1}{\Lambda_T^{2N}} \int d\vec{r}_1 \dots d\vec{r}_N e^{-\beta U_{\text{ein-mol-id}}} \\ &= \frac{1}{N_1!} \frac{1}{N_2!} \frac{1}{\Lambda_T^{2N}} V \int d\vec{r}_2 \dots d\vec{r}_N e^{-\beta U_{\text{ein-mol-id}}}. \end{aligned} \quad (\text{III.28})$$

For the remaining configurational integral, one needs to take into account all possible permutations of the particles on the lattice sites:

$$\begin{aligned} Z_{\text{ein-mol-id}} &= \frac{(N_1 - 1)!}{N_1!} \frac{N_2!}{N_2!} \frac{1}{\Lambda_T^{2N}} V \int_{\text{one perm}} d\vec{r}_2 \dots d\vec{r}_N e^{-\beta \gamma \sum_{i=2}^N (\vec{r}_i - \vec{r}_{i_0})^2} \\ &= \frac{1}{\Lambda_T^{2N}} \frac{V}{N_1} \left(\int d\vec{r} e^{-\beta \gamma r^2} \right)^{2(N-1)} = \frac{V}{\Lambda_T^2} \frac{1}{N_1} \left(\frac{\pi}{\beta \gamma \Lambda_T^2} \right)^{N-1}. \end{aligned} \quad (\text{III.29})$$

The corresponding Helmholtz free energy is

$$\begin{aligned} \frac{\beta F_{\text{ein-mol-id}}}{N} &= -\frac{1}{N} \ln(Z_{\text{ein-mol-id}}) \\ &= \frac{1}{N} \ln \left(\frac{\Lambda_T^2 N_1}{V} \right) + \left(1 - \frac{1}{N} \right) \ln \left(\frac{\Lambda_T^2 \beta \gamma}{\pi} \right). \end{aligned} \quad (\text{III.30})$$

Fixing one particle

To avoid quasi-divergence in the Hamiltonian integration, we need to prevent drifts of the whole solid. This can be achieved by fixing the position of one particle in the system.

Consider a general mixture of two types of particles. If the potential energy is invariant under the translation of all the particles, we can write

$$\begin{aligned} Z &= \frac{1}{N_1!} \frac{1}{N_2!} \frac{1}{\Lambda_T^{2N}} \int d\vec{r}_1 \int d\vec{r}_2 \dots d\vec{r}_N e^{-\beta U(\vec{0}, \vec{r}_2 - \vec{r}_1, \dots, \vec{r}_N - \vec{r}_1)} \\ &= \frac{V}{\Lambda_T^2} Z^*, \end{aligned} \quad (\text{III.31})$$

with Z^* the partition function of the system with particle 1 fixed. The free energy can then be written

$$\begin{aligned} \frac{\beta F}{N} &= \frac{1}{N} \ln \frac{\Lambda_T^2}{V} - \frac{1}{N} \ln Z^* \\ &= \frac{1}{N} \ln \frac{\Lambda_T^2}{V} + \frac{\beta F^*}{N}. \end{aligned} \quad (\text{III.32})$$

The free-energy of a system with one particle fixed and the free-energy of the full system only differ by a constant term that is independent of the potential, which corresponds to the entropy associated with the center of mass of the crystal exploring the available volume with no energy penalty.

The above derivation relies on the fact that the potential energy is invariant under a translation of the whole system. This assumption holds for any system whose energy is determined by particles interactions alone, so in particular for a hard disks mixture. It is also valid for the Einstein molecule because the external field applied by the springs is tethered to the carrier. Hence, when the whole system is translated (including the carrier), the lattice sites are translated by the same amount and the potential energy is unchanged.

This means that the free energy term $\frac{1}{N} \ln \frac{\Lambda_T^2}{V}$ coming from fixing the position of the carrier exactly cancels with the term coming from freeing the position of particle 1 in the real solid. Hence, it is enough to add the free-energy difference between the ideal Einstein molecule with one particle fixed and the solid with one particle fixed directly to the free-energy of the ideal Einstein molecule (with no particle fixed) to get the free-energy of the solid (with no particle fixed):

$$F_{\text{sol}} = F_{\text{ein-mol-id}} + \Delta F_1^* + \Delta F_2^*. \quad (\text{III.33})$$

with ΔF_1^* the free-energy difference between the ideal Einstein molecule with one particle fixed and the interacting Einstein molecule with one particle fixed, and ΔF_2^* the free-energy difference between the interacting Einstein molecule with one particle fixed and the solid with one particle fixed.

ΔF_1^*

We want to compute the free-energy difference between the ideal Einstein molecule with one particle fixed and the interacting Einstein molecule with one particle

fixed whose potential energy is given by $U_{\text{ein-sol}}^* = U_{\text{sol}}^* + U_{\text{ein-mol-id}}^*$. Using the partition function for each system, we can write this free-energy difference as

$$\begin{aligned}
\Delta F_1^* &= F_{\text{ein-sol}}^* - F_{\text{ein-mol-id}}^* \\
&= -k_B T \ln \left(\frac{\int d\vec{r}_2 \dots d\vec{r}_N e^{-\beta U_{\text{ein-sol}}^*}}{\int d\vec{r}_2 \dots d\vec{r}_N e^{-\beta U_{\text{ein-mol-id}}^*}} \right) \\
&= -k_B T \ln \left(\frac{\int d\vec{r}_2 \dots d\vec{r}_N e^{-\beta(U_{\text{ein-sol}}^* - U_{\text{ein-mol-id}}^*)} e^{-\beta U_{\text{ein-mol-id}}^*}}{\int d\vec{r}_2 \dots d\vec{r}_N e^{-\beta U_{\text{ein-mol-id}}^*}} \right) \\
&= -k_B T \ln(\langle e^{-\beta(U_{\text{ein-sol}}^* - U_{\text{ein-mol-id}}^*)} \rangle_{\text{ein-mol-id}^*}) \\
&= -k_B T \ln(\langle e^{-\beta U_{\text{sol}}^*} \rangle_{\text{ein-mol-id}^*}). \tag{III.34}
\end{aligned}$$

We measure the expectation value in the logarithm by sampling equilibrium configurations of the ideal Einstein molecule with one particle fixed. Since the particles do not interact with each other, the probability of finding a particle at a position \vec{r}_i is proportional to $\exp(-\beta\gamma(\vec{r}_i - \vec{r}_{i0})^2)$. Hence, for a given spring stiffness γ , an equilibrium configuration of the Einstein molecule can be quickly generated by drawing new positions for all particles (except the carrier) from a Gaussian distribution with standard deviation $(2\beta\gamma)^{-1/2}$.

The exponential term only takes value 0 (when there is at least one overlap in the configuration) or 1 (when the configuration has no overlap). Thus, the average term takes values in $[0, 1]$ and ΔF_1^* is positive. This makes sense since turning on hard core repulsion on top of the harmonic springs reduces the entropy per particle, leading to a higher free-energy.

The value of the spring constant used at this step sets the maximum spring stiffness for the rest of the calculation. If it is chosen too low, then all sampled configurations contain overlap and ΔF_1^* becomes infinite. Using an overly large value compromises the accuracy of the next step of the method, where springs are gradually turned off. We choose a value of γ_{max} such that $\langle \exp(-\beta U_{\text{sol}}) \rangle_{\gamma_{\text{max}}} \simeq 0.9$. We use a bisection search to find γ_{max} within a given accuracy.

ΔF_2^*

The free-energy difference between the interacting Einstein molecule with one particle fixed and the solid of interest with one particle fixed is computed by Hamiltonian integration. This is a generalisation of the thermodynamic integration where the Hamiltonian of the system itself is changed rather than the thermodynamic variables [183].

We consider a system interacting with the potential energy

$$U_\lambda^* = \lambda U_{\text{sol}}^* + (1 - \lambda) U_{\text{ein-sol}}^* = U_{\text{sol}}^* + (1 - \lambda) U_{\text{ein-mol-id}}^*, \tag{III.35}$$

that interpolates between the two systems as λ varies from 0 to 1. The derivative of the free energy of this system reads

$$\frac{\partial F_\lambda^*}{\partial \lambda} = -k_B T \frac{\partial Z_\lambda^*}{\partial \lambda} \frac{1}{Z_\lambda^*}, \tag{III.36}$$

with

$$\frac{\partial Z_\lambda^*}{\partial \lambda} = -\beta \frac{1}{\Lambda_T^{2(N-1)}} \frac{1}{N_1!} \frac{1}{N_2!} \int d\vec{r}_2 \dots d\vec{r}_N (-U_{\text{ein-mol-id}}^*) e^{-\beta U_\lambda^*}. \quad (\text{III.37})$$

Hence

$$\frac{\partial F_\lambda^*}{\partial \lambda} = -\langle U_{\text{ein-mol-id}}^* \rangle_{(1-\lambda)\gamma_{\text{max}}}. \quad (\text{III.38})$$

The expectation value on the right-hand side is an ensemble average for a composite system with one particle fixed, with spring stiffness $(1-\lambda)\gamma_{\text{max}}$ and hard-core repulsion. Then the free-energy difference between the interacting molecule with one particle fixed and the solid with one particle fixed is obtained as

$$\begin{aligned} \Delta F_2^* &= - \int_0^1 d\lambda \langle U_{\text{ein-mol-id}}^* \rangle_{(1-\lambda)\gamma_{\text{max}}} \\ &= - \int_0^{\gamma_{\text{max}}} d\gamma \left\langle \sum_{i=2}^N (r_i - r_{i_0})^2 \right\rangle_\gamma. \end{aligned} \quad (\text{III.39})$$

We compute the integrand for various spring stiffness using Monte Carlo canonical simulations (N , V and T constant). Following Ref. 174, we sample the spring stiffness logarithmically by performing the change of variable

$$\Delta F_2^* = - \int_{\ln(c)}^{\ln(\gamma_{\text{max}}+c)} d[\ln(\gamma+c)] (\gamma+c) \left\langle \sum_{i=1}^N (r_i - r_{i_0})^2 \right\rangle_\gamma. \quad (\text{III.40})$$

Steps are performed in $\ln(\gamma+c)$ which results in a finer sampling at low γ where the integrand varies more quickly. Using benchmark simulations, we concluded that $c = e^1 k_B T \sigma^{-2}$ is nearly optimal for our systems⁶. We typically measure the integrand at 30 spring stiffness between 0 and γ_{max} , and use Simpson rule to compute the integral numerically.

While the Monte Carlo simulations reach equilibrium quickly at large and moderate spring stiffness, the equilibration time increases sharply when $\gamma \rightarrow 0$. In a first equilibration run, we automatically increase simulation length until the equilibrium is reached according to the procedure described in Appendix B. Then, the system is simulated for the same length and averages are measured. Simulations run for at least 10^4 Monte Carlo cycles⁷, but the automatic increase of the simulation length leads to some systems at $\gamma = 0$ being simulated for as much as 10^7 cycles. In practice, we observe that the vast majority of CPU time in the whole Frenkel-Ladd procedure is spend in simulating the one or two systems at the lowest spring stiffness. For our systems of non-additive hard disks, the Monte Carlo simulation at $\gamma = 0$ could be replaced by a faster event-driven molecular dynamics simulation as described in Section II.1.2.

⁶Larger values of c seem to be better in 3D [174].

⁷One Monte Carlo cycle is N trial moves with N the number of particles in the system.

Putting everything together...

The calculation of the solid Helmholtz-free-energy by the Frenkel-Ladd method with the Einstein molecule approach boils down to

$$\begin{aligned} \frac{\beta F_{\text{sol}}}{N} &= \frac{\beta F_{\text{ein-mol-id}}}{N} + \frac{\beta \Delta F_1^*}{N} + \frac{\beta \Delta F_2^*}{N} \\ &= \frac{1}{N} \ln \left(\frac{\Lambda_T^2 N_1}{V} \right) + \left(1 - \frac{1}{N} \right) \ln \left(\frac{\Lambda_T^2 \beta \gamma_{\text{max}}}{\pi} \right) \\ &\quad - \frac{1}{N} \ln(\langle e^{-\beta U_{\text{sol}}^*} \rangle_{\text{ein-mol-id}^*}) - \frac{\beta}{N} \int_0^{\gamma_{\text{max}}} \frac{d\gamma}{\gamma} \langle U^* \rangle_{\gamma}, \end{aligned} \quad (\text{III.41})$$

where each term is either computed analytically or can be obtained to an arbitrary precision from simulations.

III.4.2 Estimating uncertainties

Since we aim for precise free-energy calculations, it is useful to have a way of estimating uncertainties. One can always run the Frenkel-Ladd calculation several times at the same state point and obtain a estimate of the statistical error from the standard deviation of the calculated values, but the computational cost can quickly become prohibitive.

In the Frenkel-Ladd method, the first term $F_{\text{ein-mol-id}}$ is exact, so statistical errors only come from ΔF_1^* and ΔF_2^* . The error on ΔF_1^* stems from the uncertainty on the measured ensemble average. Since all the sampled configurations are uncorrelated, the expected error in ΔF_1^* is simply obtained from the standard deviation of the measurements in each configuration.

For ΔF_2^* , the error again stems from the ensemble averages. This time, the configurations generated by the Monte Carlo simulations are not necessarily uncorrelated, and we use the standard block-average (or Flyvbjerg-Peterson) method to compute the statistical error on the measured mean values [145, 146, 188]. To estimate the propagated error on the integral of these points with error bars, we draw new sets of point from Gaussian distributions centred at the simulated points, with a width equal to the error bar at that point. This provides fake new realisations of the simulated data points, from which ΔF_2^* can be computed. Finally, the standard deviation of the integrals on the fake points is taken as the uncertainty on ΔF_2^* .

To assess the reliability of the method, we computed 100 times the free energy of a S1 solid of 200 particles at density $1.7 \sigma_{LL}^{-2}$, using 30 points logarithmically sampled for the calculation of ΔF_2^* , and compared the standard deviation of these real realisations with the error estimated as described above. The standard deviation measured from fake sets $0.0069 k_B T$ is in excellent agreement with the directly measured one $0.0067 k_B T$.

The simulated points can be seen as obtained after one step of a random walk around the exact curve, with a Gaussian step of width given by the measured error on the points. Creating the fake data sets from the simulated points actually samples the second step of this random walk. For most reasonable

functions, we expect that this will lead to a slight overestimation of the error, which is safe for error bars. Hence, with the fake set method, we can compute an accurate estimate of the statistical error on the free-energy with a single realisation of the Frenkel-Ladd method⁸.

III.4.3 Finite size correction

The Frenkel-Ladd calculations are always performed on finite systems, but we aim to calculate the free-energy of the phases in the thermodynamic limit. In order to correct for finite-size effects, we repeat the Frenkel-Ladd calculation for systems of different sizes. Then, assuming that the leading order of finite size correction scales like $1/N$, we fit the measured free energies as a function of $1/N$ with a linear function and extrapolate to infinite systems.

The error bars on each point are propagated to the fit parameters, which provides an estimate of the error bar on the extrapolated value. An example of a fit is shown in Figure III.10 for the hexagonal solid. We observe that, while the linear scaling is excellent for the monodisperse systems, the free-energy of binary mixtures is typically more noisy, and seem to exhibit a small deviation from the linear scaling (see for instance Figure III.16 for the deviation from linear scaling).

III.4.4 Solids free-energies

For the Frenkel-Ladd method to be accurate, no particle in the solid should escape their lattice site when the springs are turned off. Therefore, instead of using it to compute free-energies at all densities down to the melting transition, where particles start to diffuse, we use the Frenkel-Ladd method to compute the free-energy of each solid at only one high density point where we are guaranteed to have no defect formation. Then, we use this reference point in conjunction with an accurately measured equation of state to obtain the free-energy at all densities by thermodynamic integration (see Section III.2.1).

We measure equations of state with high accuracy for each solid using event-driven molecular dynamics simulations. Since the error bars on the points are tiny, we use cubic splines interpolation rather than fit to obtain continuous expressions for the integration. Finally, the Gibbs free-energy for the solid phases at any pressure is obtained as

$$\frac{\beta G(p)}{N} = \beta \int_{\rho_0}^{\rho(p)} \frac{p(\rho')}{\rho'^2} d\rho' + \frac{\beta F(\rho_0)}{N} + \frac{\beta p}{\rho(p)}. \quad (\text{III.42})$$

Hexagonal solids

The case of the pure hexagonal solid allows us to validate our Frenkel-Ladd implementation. Figure III.9-Left displays the free energy of hard disks for various

⁸We also tried propagating the errors analytically using the expressions of Simpson integration. The resulting –very long– expressions turn out to slightly underestimate the error bars.

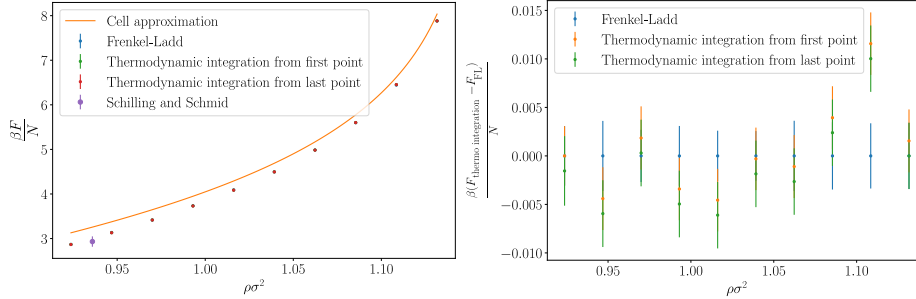


Figure III.9: (Left) Helmholtz free-energy of the hexagonal solid of hard disks computed from Frenkel-Ladd method (blue points), extrapolated from the first and last point with thermodynamic integration (red and green points) or reported by Schilling and Schmid in Ref. 187 purple point. The orange curve is corresponds to the cell approximation. (Right) Free-energy difference between the blue, red and green points that are almost indistinguishable on the left plot.

densities computed with the Frenkel-Ladd method. The green and red points are obtained by thermodynamic integration from the first (or last) Frenkel-Ladd point. The points obtained from direct Frenkel-Ladd calculations or thermodynamic integration are almost indistinguishable in this representation. In Figure III.9-Right, the free-energy difference between the thermodynamic integrations and direct Frenkel-Ladd simulations is shown. Error bars correspond to one standard error. The points are all consistent within 2 standard errors, which confirms that our implementation of the Frenkel-Ladd method yields accurate free-energy *differences*.

To validate the absolute value of the computed free-energies, we show on Figure III.9-Left the free-energy obtained from the cell approximation (orange curve). At large densities, when the cell approximation becomes good, the curve converges to the value computed with the Frenkel-Ladd method. In addition, the purple point corresponds to the free-energy value reported in Schilling and Schmid [187] for a solid of 100 hard disks at pressure $10 k_B T \sigma^{-2}$. The corresponding density is obtained from the simulated equation of state. The resulting value is compatible with our Frenkel-Ladd calculations within the error bars. The reported system is much smaller than the one we use, so finite size effects are also expected. These observations give us confidence that our implementation of the Frenkel-Ladd method is working correctly.

For the phase diagram construction, we choose as a reference point a hexagonal solid of monodisperse hard disks at density $\rho_0 \sigma_{LL}^2 = 1.11$. Using the Frenkel-Ladd method we calculate the Helmholtz free-energy for systems containing $N = 418$ to 10864 particles. The free-energy in the thermodynamic limit is obtained by linear extrapolation as depicted in Figure III.10, which yields a final value of $\beta F(\rho_0)/N = 6.5253 \pm 0.0001$. For both Frenkel-Ladd calculation and equation of state measurement, we simulate the system in a rectangular box as close as possible to a square that accommodates the periodic structure.

The free-energy of the hexagonal solid of small disks is obtained from the one of large disks by noting that both should have the same reduced free-energy at the same reduced pressure.

$$\frac{\beta G_{\text{hex}}^{\text{S}}(p)}{N} = \frac{\beta G_{\text{hex}}^{\text{L}}(pq^2)}{N} - \ln(q^2). \quad (\text{III.43})$$

The logarithm term comes from the rescaling of the thermal wavelength Λ_T in the Frenkel-Ladd expression (Equation III.41).

S1 solid

We use a system of 1024 particles of each type to compute the equation of state of the S1 solid. At a reference density of $1.9 \sigma_{LL}^{-2}$, the Helmholtz free energy obtained from the Frenkel-Ladd method extrapolated to the thermodynamic limit is $5.1554 \pm 0.0002 k_B T/N$. We use systems of size ranging from $N = 450$ to $N = 20000$ for the extrapolation.

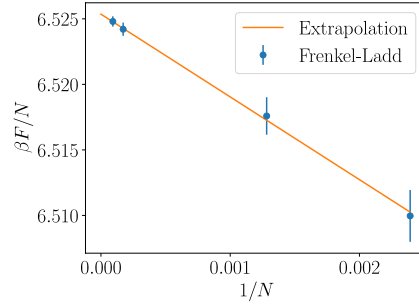


Figure III.10: Extrapolation of the free-energy of the hexagonal solid to infinite system sizes, at density $\rho_{0.5} = 1.11$.

Sigma solid

In addition to the hexagonal and S1 solids, we consider the sigma solid as a candidate phase. It did not show up in the infinite pressure study nor in the self-assembly simulations, but it is the first approximant of the dodecagonal quasicrystal *ie.* the smallest of an infinite sequence of periodic phases whose local structure converges to that of the quasicrystal. Hence, it is reasonable to compare its stability. The sigma-phase unit-cell is depicted in Figure III.11.

At a reference density of $1.5 \sigma_{LL}^{-2}$, the Frenkel-Ladd calculation gives a Helmholtz free energy of $4.9623 \pm 0.0002 k_B T/N$ in the thermodynamic limit, extrapolating from systems containing up to $N = 14700$ particles.

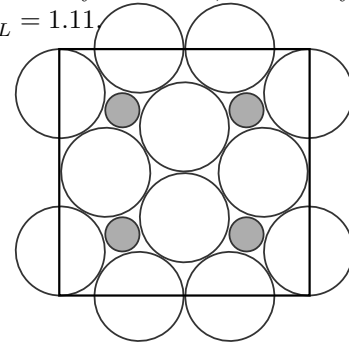


Figure III.11: Unit cell of the Sigma-phase, the first approximant to the square-triangle dodecagonal quasicrystal.

Dodecagonal quasicrystal

Finally to obtain the free-energy of the dodecagonal quasicrystal, we use again the random tiling hypothesis, but rather than using the free-energy of the Hex_L + S1 coexistence as a reference, we compute the free-energy of a real quasicrystal configuration with the Frenkel-Ladd method.

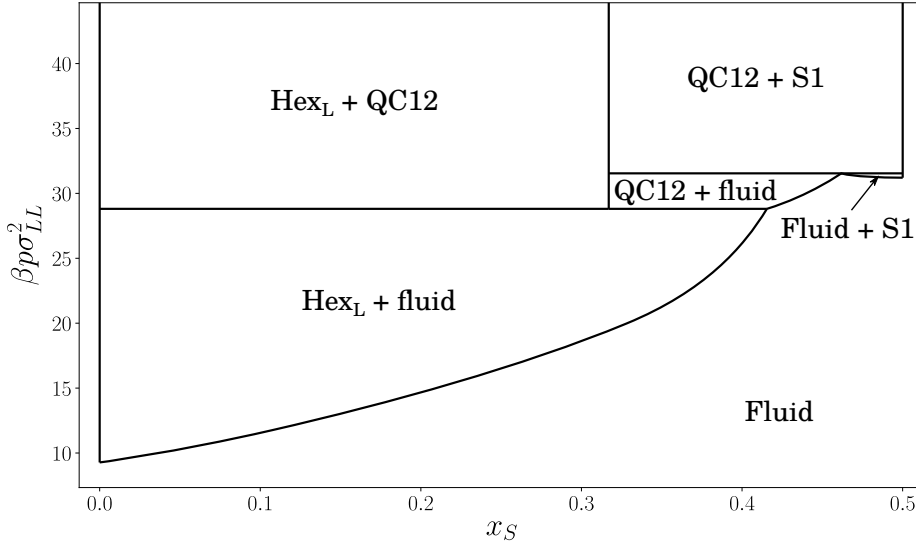


Figure III.12: Phase diagram of binary mixtures of non-additive hard disks with size ratio $q = 0.46$ and non-additivity parameter $\Delta = -0.0709$ corresponding to the equivalent 3D geometry of spheres sedimented on a flat surface. The random tiling dodecagonal quasicrystal is labelled “QC12”. Although considered as a candidate phase, the sigma approximant of the quasicrystal is nowhere stable.

The quasicrystal configuration is constructed from the Schlottmann inflation rule (see later Section III.5.1) applied 4 times to a S1 square seed. The generated patch is then cut to fit in a periodic box. Note that this step destroys the global 12-fold symmetry and frustrates the quasicrystal. Rigorously, the configuration is a very large approximant of the quasicrystal.

The tiling entropy is then added to the free-energy of the configuration like in Equation III.25. Doing so, we obtain a Helmholtz free-energy of $5.550309 \pm 0.00005 k_B T/N$ at the reference density $1.5 \sigma_{LL}^{-2}$ for the random tiling dodecagonal quasicrystal.

III.4.5 Finite pressure phase diagram

We construct the phase diagram by repeating common tangent constructions on a fine grid of pressures, as explained in Section III.1.1. The fluid free-energy is obtained from thermodynamic integration of equations of state measured in simulations as described in Section III.2.2. For the solid phases, the free-energy is calculated from the Frenkel-Ladd method, in conjunction with thermodynamic integration of accurate equations of states measured in simulations.

The resulting phase diagram is shown in Figure III.12. As before, we focus on the region $x_S \leq 0.5$ which is relevant for the dodecagonal quasicrystal.

As for the phase diagram calculated with the cell approximation (see Fig-

ure III.8), we recover the infinite pressure phase behaviour at large pressures. However, the bottom part of the phase diagram is very different. The solidification of the S1 and QC12 phases occurs at much larger pressures than what was predicted in the previous phase diagram. This difference most probably comes from the fluid. Indeed, in the previous phase diagram, the fluid free-energy was obtained from an analytical equation of state that seriously overestimates the pressure at large densities, thus artificially destabilising the fluid. As shown in Figure III.3, the error is the largest at intermediate compositions. Consistently, we observe the largest discrepancy in solidification pressure for the S1 phase between the two phase diagrams. At $x_S = 0$, the monodisperse system of hard disks freezes at pressure $9.2 k_B T \sigma^{-2}$ very close to the value reported in large scale simulations [152, 169].

Even though it was included in the common tangent constructions as a candidate structure, the sigma phase is nowhere found to be stable. The dodecagonal random tiling quasicrystal however is stable for pressures above $28.8 k_B T \sigma_{LL}^{-2}$. It coexists with the fluid for a small range of pressures above the freezing transition, for compositions larger than the ideal quasicrystal compositions. In contrast to what was predicted in the previous phase diagram, this is in line with our observation that the quasicrystal is more easily self-assembled with an excess of small particles. Other authors reported that self-assembly of certain phases may be kinetically facilitated off-stoichiometry [189].

Interestingly, the random tiling entropy is required to stabilise the dodecagonal quasicrystal. In Figure III.13, we compare the free-energies of the dodecagonal quasicrystal and the competing coexistence of Hex_L and S1 at the quasicrystal composition. Without the constant tiling entropy term, the coexistence prevails and the quasicrystal is not stable. In a previous study of hard disks augmented by a repulsive square-shoulder interaction, Pattabhiraman et al. [88] observed a similar dodecagonal quasicrystal based on the square-triangle random tiling. In their case however, free-energy calculations showed that the quasicrystal is stable even without the random tiling entropy. This means that the vibrational entropy alone is sufficient for the quasicrystal to be stable, and although it might still be relevant, the random tiling hypothesis is not crucial there. In contrast, our findings depend rather critically on this hypothesis, which we should

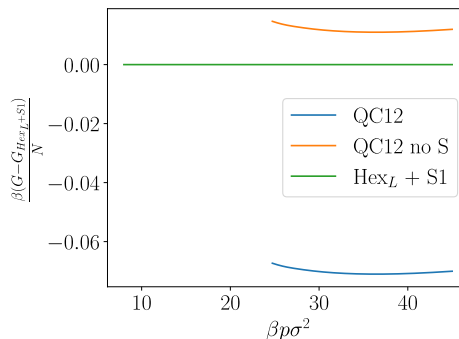


Figure III.13: Free-energy difference between the competing coexistence of $\text{Hex}_L + \text{S1}$ and the quasicrystal at the quasicrystal composition. For the quasicrystal, the orange curve corresponding to the vibrational entropy alone and lies above the coexistence free-energy, while the addition of the constant tiling entropy term in the blue curve stabilises the quasicrystal.

now investigate in more details.

III.5 The random tiling hypothesis

Entropy is the only driving force in our systems with hard interactions. The random tiling quasicrystals that we consider are stabilised by two kinds of entropies: the vibrational entropy of the particles wiggling around their lattice sites on the one hand, and the tiling entropy accounting for all possible realisations of the random tiling on the other hand. The random tiling hypothesis is the assumption that these two entropy contributions can be decoupled. This assumes that all tiling configurations have essentially the same vibrational entropy, thus allowing the whole random tiling ensemble to be considered a degenerate single phase with non-zero configurational entropy.

In this Section, we would like to quantitatively assess the validity of the random tiling hypothesis for the dodecagonal quasicrystal of binary non-additive hard disks. As before, we focus on the size ratio $q = 0.46$ and non-additivity parameter $\Delta = -0.0709$ which corresponds to the equivalent 3D geometry of spheres on a plane.

To assess the validity of the random tiling hypothesis, we perform high-precision calculations of the vibrational entropy of various tiling configurations. In particular, we compare the vibrational entropy of *ideal* quasicrystal configurations obtained by an inflation method, and random tiling configurations.

III.5.1 Inflation rules

Ideal quasicrystal configurations can be generated by so-called inflation methods, in which every tile of a tiling is replaced by a cluster of tiles. By iterating the inflation rules on an initial seed, one generates larger and larger patches of tiling that converge to a quasicrystalline configuration.

Several inflation rules exist for the square-triangle tiling. The most common Stampfli [27] and Schlottmann [28, 190] rules are depicted in Figure III.14. The simpler Stampfli rule generates a quasiperiodic tiling with 6-fold symmetry while the Schlottmann rule produces a dodecagonal tiling. The quasicrystals obtained by decorating these tilings are called *ideal* because the 6 or 12-fold rotational symmetry is exact at the central point. In contrast, random tiling quasicrystals exhibit their n -fold symmetry only on average over the random tiling ensemble. In addition to the rotational symmetry, the inflated tilings possess a self-similarity symmetry which is obvious from the construction process: an infinite sequence of bigger and bigger squares and triangles can be drawn on top of an inflated tiling that form again a square triangle tiling. In the high dimensional representation, ideal tilings corresponds to those with no phason fluctuations, *i.e.* whose representative surface follows the ideal hyperslope as close as possible.

The square-triangle inflation rules can also be realised by the following algorithm [164]:

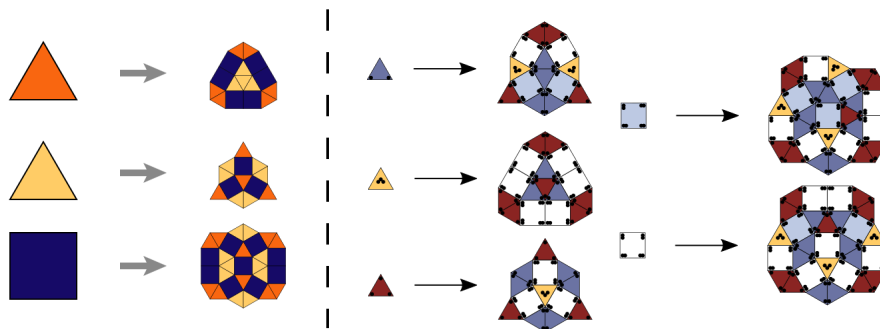


Figure III.14: Stampfli (left) and Schlottmann (right) inflation rules. They respectively generate a hexagonal and dodecagonal quasiperiodic tiling when iterated *ad infinitum*. Note that in both sets of rules, tiles of the same shape can exist with different labels (represented by colors), and that the replacement in the Schlottmann rule additionally depends on the orientation of the tile (represented by the black dots on the tiles). Taken from the Tilings Encyclopedia (<https://tilings.math.uni-bielefeld.de>) maintained by Frettlöh, Harriss and Gähler.

1. Choose a initial seed.
2. Scale up the tiling by a factor $2 + \sqrt{3}$.
3. Replace every vertex by a dodecagonal wheel.
4. Repeat from 2.

The procedure is depicted in Figure III.15. The dodecagonal wheel placed at each vertex can appear in two different orientations (blue and red) that have the same boundary. Different rules for the wheels orientations result in different quasiperiodic tilings, with possibly different symmetries [140]. The hexagonal Stampfli tiling is obtained by picking the same orientation for all wheels. To obtain the Schlottmann dodecagonal tiling, a more complicated rule must be followed. Because of the self-similarity property, the tiling patch at step n can be found again at the centre of the tiling patch obtained at step $n + 1$. The Schlottmann tiling is obtained by orienting each wheel at step $n + 1$ according to the dominant colour of the edges attached to the vertex it came from at step n . Since the majority rule is ambiguous at step n for points at the border of the tiling patch, their local environment is determined by looking at the image of the step n patch at step $n + 1$. Other selection rules for the orientations of the wheels can be invented [140]. For instance, one can pick the orientation uniformly at random for every wheel. This results in random tiling quasicrystal that has average 12-fold symmetry and approximate self-similarity. Note that, while this method is very useful to generate alternative tiling by playing with orientation selection rules, it is not strictly equivalent to the traditional tile-replacement

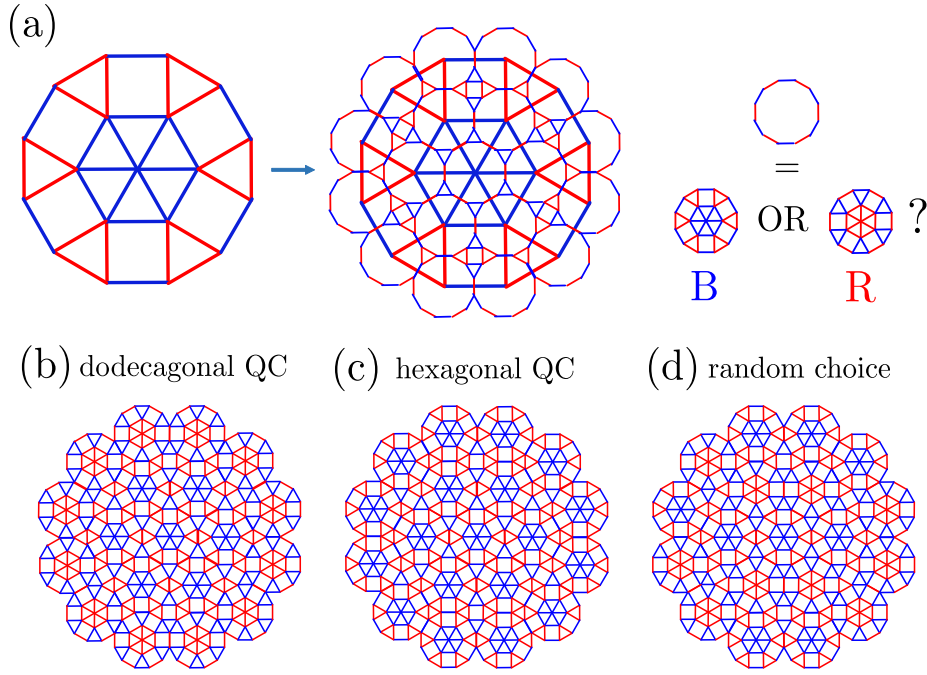


Figure III.15: Illustration of the inflation procedure. At each step, vertices are replaced by dodecagonal wheels which can appear in two orientations. Different selection rules result in different quasiperiodic tilings. Courtesy of Impérator-Clerc et al., taken from Ref. 140.

inflation method. Indeed, for the Schlottmann scheme in particular, it requires that the tiling patch at step n can be recovered at the centre of the patch at step $n + 1$. This can only work with a very limited set of seeds for which the inflation procedure preserves the location and orientation of the central point. No such issue occur with the tile-replacement approach, but designing new rules that enforce alternative symmetries is harder there.

When starting from a square seed with Stampfli or Schlottmann rules, the inflated borders of the initial square allow us to cut out square periodic approximants of the quasicrystal. We use this to generate our configurations. The number of particles in the tiling patch grows exponentially fast in the number of inflation iterations. Starting from a square seed, we used the configurations obtained after $n = 2, 3$ or 4 inflation steps, which corresponds to systems of 306, 4263 and 59362 particles respectively. In addition, we generate Stampfli tiling by applying 2 or 3 inflation steps to a sigma unit cell, which results into systems of 2284 and 31812 particles respectively. Since the orientation of the original sigma seed changes when the inflation rule is applied, our current implementation of the Schlottmann inflation fails in this case, so we only use the sigma seed to generate hexagonal Stampfli tilings. The exponential growth of the tilings with inflation iterations limits the number of available points for finite size scaling. However, the largest systems are large enough that we expect finite size corrections to be very small there. Other schemes exist, such as the Schlottmann half-step rule [191], that generates intermediate approximants, but its implementation is cumbersome, and we did not use it here. Likewise, seeds of intermediate size could be used, although, as described above, these can only be inflated with the tile-replacement approach, which we did not implement.

III.5.2 Zipper moves

To generate random tiling configurations, we apply *zipper moves* to ideal configurations [59]. A zipper move is a rearrangement of tiles around a closed loop that conserves the number of tiles of each type. Although to our knowledge, the ergodicity of the zippers have not been rigorously proven, numerical estimates of the square-triangle entropy based on zipper moves are consistent with the known exact value, suggesting that zipper moves indeed allow us to sample all configurations in the random tiling ensemble [59].

To obtain random tiling configurations for our free-energy calculations, we generate random configurations from ideal ones by applying 1000 zipper moves. Since the length of the zipper scales with the number of particles in the system [59], there is a priori no need to use more for larger systems. The generated configurations indeed look completely random and uncorrelated with the ideal starting point.

III.5.3 Ideal versus random quasicrystals

To assess the validity of the random tiling hypothesis, we compare the vibrational entropies of the ideal Schlottmann quasicrystal, the ideal hexagonal

Stampfli quasicrystal and their random tiling counterparts, using the Frenkel-Ladd method. For each inflation step ($n = 2, 3$ or 4 for the square seed and $n = 2$ or 3 for the sigma seed), we generate 5 different random configurations by applying zipper moves to the approximant. The density is fixed at $1.5\sigma_{LL}^{-2}$ for all systems.

In order to reduce the statistical error on the entropy, we repeat the Frenkel-Ladd calculation more than 6000 times for the smallest configurations obtained after 2 inflation steps of the square seed, more than 1000 times for the configurations obtained after 3 inflation steps of the square seed, and between 50 and 150 times for the largest systems. For the random configuration obtained from the sigma seed inflation, we repeat the calculation more than 2000 times on the tilings obtained after 2 inflation steps, and more than 200 times on the tilings obtained after 3 inflation steps. We check that for every configuration, the repeated measurements follow a Gaussian distribution, and use the standard deviation of the outcomes, divided by the square root of the number of repetitions (*i.e.* the statistical error on the mean) as our error bars. The results are shown in Figure III.16. The finite size scaling of the free energy appears to be non-linear, and adding the heuristic finite size correction term $\ln(N)/(2N)$ proposed in Reference 145 does not remove the non-linearity. One could argue that a linear regime is reached for very large system sizes, with an almost zero slope. Therefore, we perform no extrapolation and use the value of the free energy per particle for the largest systems as our estimate of the thermodynamic-limit value. We obtain $5.50309(5)k_B T$ for the ideal dodecagonal quasicrystal, $5.50342(4)k_B T$ for the ideal hexagonal quasicrystal and $5.50392(4)k_B T$ for the average over the 5 largest realisations of the random tiling quasicrystal.

First we note that the free energies of the 5 random tiling quasicrystals generated at each system size are consistently degenerate within our errorbars (black clusters in Figure III.16). Although we considered only 5 out of many possible configurations in the random tiling ensemble at each system size, the absence of any outliers gives us confidence that the vast majority of configurations in the random tiling ensemble indeed have essentially the same vibrational entropy. This observation quantitatively validates the random tiling hypothesis and justifies the treatment of the earlier quasicrystals as random tiling phases with non-zero configurational entropy.

The measurements show, nonetheless, that some configurations in the random tiling ensemble are special. The free energy of the ideal quasicrystals is consistently lower than that of the random configurations, with the difference on the order of $10^{-3}k_B T$ per particle. Although small, this difference is measurable, and of the same order of magnitude as the free-energy difference between face centred cubic (FCC) and hexagonal close packing (HCP) crystals of monodisperse hard spheres [135, 136, 192]. Moreover, we find that the ideal dodecagonal quasicrystal obtained with Schlottmann inflation has slightly more vibrational entropy than the ideal hexagonal Stampfli quasicrystal.

The vibrational entropy difference between random and ideal quasicrystals can be understood from the different local environments that can be found in the underlying tiling. For instance, ideal quasicrystals obtained by the inflation

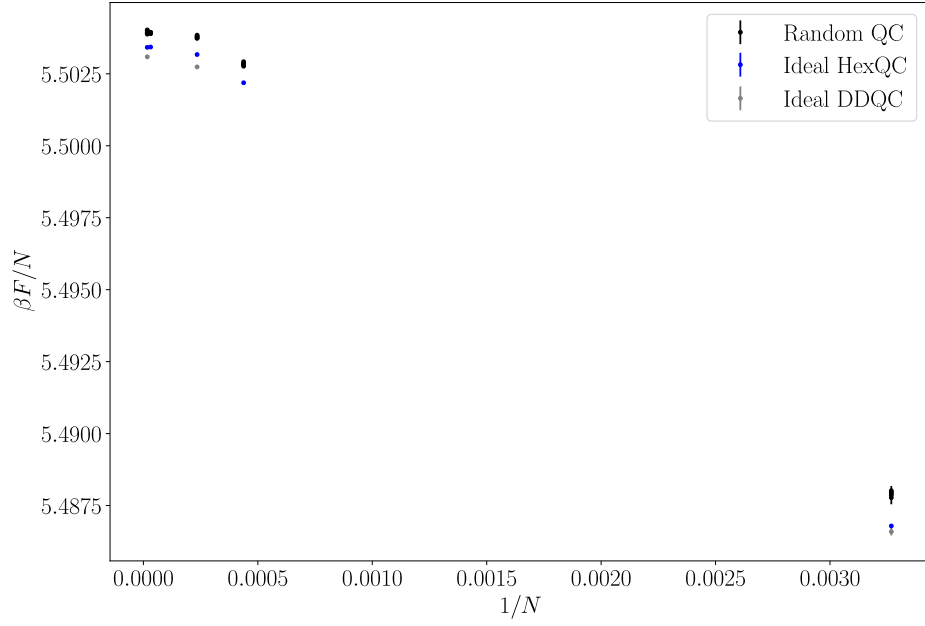


Figure III.16: Free-energies of the dodecagonal (grey), hexagonal (blue) and 5 random dodecagonal quasicrystals (black), for various system size. The error bars are the statistical error on the mean obtained by repeating Frenkel-Ladd calculations many times, and are smaller than the symbols for most points. Two system sizes are obtained by inflation of a sigma seed, for which our implementation of the Schlottmann inflation fails. Hence, two grey points are missing.

method contain no local environment formed of 4 squares meeting at the same vertex while the randomised ones contain a non-zero concentration of those [193]. We expect however that the first-neighbour local environments alone do not explain fully the entropy difference. Indeed, both the dodecagonal and hexagonal ideal quasicrystals have the same distribution of local environments when considering only the first neighbour shell (ignoring the orientation of the environments). Hence, neighbour shells beyond the first one certainly play a non-negligible role.

From the point of view of quasicrystals theory, the vibrational entropy difference between ideal and random structures is an interesting illustration of phonon-phason coupling [30, 63]. The representative surface of the ideal quasicrystal in the high-dimensional picture follows the average slope as closely as possible. In contrast, the surfaces obtained from the lifting of the random tiling quasicrystals exhibit fluctuations in the perpendicular space whose modes correspond to phasons. The lower vibrational entropy of the random quasicrystals shows that the presence of phason modes in these systems hinders lattice vibrations, *i.e.* reduces the amplitude of the phonon modes. Conversely, the high vibration entropy of ideal quasicrystals suggests that phonon modes are the strongest in the ideal quasicrystal, in the absence of phasons.

III.6 Perspectives

The non-linear scaling of the free-energy with inverse system size for the quasicrystals is puzzling [184]. It would be interesting to compute the free energy of systems of intermediate sizes to obtain a better idea of the actual tiling. As mentioned before, such configurations could be generated by using the tile-replacement implementation of the inflation rules, which do not suffer from the absence of exact self-similarity that occur with most seeds. In addition, more complex “half-step” rules could be used to generate tilings of intermediate sizes from all seeds [191].

In addition to ideal dodecagonal, ideal hexagonal, and random quasicrystals, it would be interesting to include the quasicrystals obtained from the random Stampfli rule to the comparison. Random Stampfli tilings are obtained by choosing the orientation of the wheels at random at each inflation step. The resulting structures have dodecagonal symmetry, but in contrast to the ideal Schlottmann tiling, they only have approximate self-similarity properties. Random tiling quasicrystals also have dodecagonal symmetry and lack self-similarity properties, but they exhibit much stronger phason modes.

The use of a binary mixture, which provides an explicit handle on the composition, is very convenient to control the relative amount of each tile. In addition, it allowed us to discover an octagonal quasicrystal whose underlying tiling can be continuously changed as a function of composition. However, the binary nature of the system becomes a limitation when trying to measure phonon-phason couplings. Indeed, the hydrodynamic theory of quasicrystals predicts that the free energy of the system is quadratic in the global perpendicular strain [30]. This

prediction has been verified in the remarkable work of Reference 63, where the authors measured the dependence of the free energy on the perpendicular strain, by measuring the free energy of a sequence of approximants with small perpendicular strains, in one-component Lennard-Jones-Gauss systems. It would be tempting to do the same thing in our mixtures of hard disks. However, in a binary system, changing the perpendicular strain also changes the composition. Hence, the measured free energies cannot be meaningfully compared. Repeating the analysis of Reference 63 in other one-component quasicrystal-forming systems would be extremely valuable in assessing the generality of the random tiling hypothesis and hydrodynamic theory. In particular, the very simple hard-core-square-shoulder systems would be excellent candidates [87, 88].

III.7 Acknowledgements

Results presented in this Chapter, in particular the interpretation of the phonon-phonon couplings, benefited from fruitful discussions with Anuradha Jagannathan and Laura Filion. This work has not been published yet.

Conclusion

Likos and Henley’s intuition that binary mixtures of non-additive hard disks might prove good models for quasicrystals [74] turned out fruitful. This simple two-dimensional model appears naturally in the study of binary mixtures of three dimensional hard spheres confined at an interface (see Section .6.2). As demonstrated throughout this thesis, our simulations strongly suggest that this elegant model system provides a robust recipe for realizing the self-assembly of at least two different colloidal quasicrystals.

In Chapter I, using an Monte-Carlo method to sample candidate structures in a more systematic way than the explicit constructions used in previous studies [74], we confirmed that several random tiling quasicrystal phases are stable in binary mixtures of hard disks at infinite pressure. Moreover, the introduction of non-additivity which models three-dimensional effects that inevitably occur when two different types of particles sit at an interface, was shown to increase the size ratio interval in which the main quasicrystal is stable at infinite pressure. This result is encouraging for experimental searches of this quasicrystal.

In Chapter II, we turned our attention to the finite pressure phase behaviour of our binary mixtures, focusing on the common geometry of spheres lying on a plane. Performing extensive self-assembly simulations, we show that the dodecagonal random tiling quasicrystal predicted to be stable at infinite pressure can also spontaneously self-assemble at finite pressures. In addition, we found a surprising new octagonal random tiling quasicrystal based on a tiling of the plane with three types of tiles, whose composition can be continuously changed while keeping the 8-fold symmetry. This discovery suggests that dense tiles compatible with a random tiling of the plane are sufficient ingredients for the self-assembly of quasicrystals. The configurational entropy of the random tiling ensemble then ensures that the maximally symmetric, quasicrystalline phase, is favoured.

Finally, in Chapter III, we quantitatively addressed the question of the thermodynamic stability of the dodecagonal random tiling quasicrystal. Using both an approximate analytical method and an essentially exact numerical approach, we predict the phase diagram for a binary mixture of hard spheres lying on a plane, at size ratio $q = 0.476$. We confirm that the dodecagonal quasicrystal is indeed thermodynamically stable over all considered competitors, and show that the configurational entropy of the random tiling ensemble is essential to its stability. Finally, we performed high-precision measurements of the free energy

of ideal and random realisations of the dodecagonal quasicrystal showing that all random realisations have essentially degenerate free energies, as conjectured by the random tiling hypothesis. Interestingly, our measurements show that the ideal dodecagonal quasicrystal has a slightly higher vibrational entropy than its randomised counterparts. This is the signature of phonon-phason couplings that are particular to quasicrystals.

This work opens up perspectives in several directions. The most exciting one is perhaps the possibility of an experimental realisation of the system. In contrast to many of the more complex interaction potentials that have been shown to facilitate quasicrystal self-assembly in simulations [82, 87, 99], hard sphere colloids are readily realizable in experiments in a wide range of sizes [103–105]. The expertise on the synthesis of hard colloids is already there, and mixing two types of such particles in a quasi-two-dimensional geometry should be readily doable in experiments. For example, past research by Thorneywork and co-authors has explored both single-component and binary mixtures of hard spheres sedimented onto a substrate, demonstrating excellent agreement with simulations and theoretical predictions based on hard-disk models [106, 107]. Our work suggests that such attempts should focus on size ratios around $q \sim 0.46$ and number fractions of small spheres close to $x_S \sim 0.32$. The octagonal quasicrystal might be found for size ratio between 0.45 and 0.55, and number fractions of small particles between 0.65 and 0.73. These range of size ratio can be accurately realised in current experimental systems, where size polydispersity is very well controlled. Having an experimental system in which quasicrystals of different symmetries could reliably self-assemble, on the micron scale, would be a real breakthrough in the study of quasicrystals. Imaging at this scale only requires optical microscopy, enabling real-time and real-space tracking of particles. This would be particularly valuable in the study of nucleation and growth of quasicrystals, as well as the dynamics of their peculiar defects. Moreover, colloidal quasicrystals with particle sizes similar to the wave length of visible light have been suggested as intriguing candidate structures for creating photonic materials capable of *e.g.* manipulating light signals [39, 40]. Hence, a colloidal quasicrystal at the micron scale would also be a huge step forward in the direction of photonic applications in the visible spectrum.

Growth and defect studies can already be carried out in numerical simulations and will be valuable to guide or interpret experiments. More studies are required in general on the dodecagonal and octagonal quasicrystals found in the hard sphere mixtures. Aside from the obvious extension to non-additivities that realise other geometries than spheres-on-plane, the study of the self-assembled structures would benefit from improved methods to analyze the perpendicular space structure of quasicrystals in the presence of strong thermal fluctuations. Additionally, significant work remains to be done on the new octagonal quasicrystal. In particular, it would be interesting to compute its tiling entropy as a function of composition, and to identify possible ideal configurations hidden in the random tiling ensemble. Having access to the correct configurational entropy of the octagonal quasicrystal would also enable direct free-energy calculations on this phase, which would be extremely helpful for proving its thermodynamic

stability. In the absence of a good estimate of this entropy, direct coexistence simulations could still be used to determine phase boundaries and quasicrystal free energies [95].

In a more exploratory direction, self-assembly of hard spheres lying on a plane is reminiscent of billiard balls, and begs the question of how far can these systems be scaled up. In contrast to colloidal systems which undergo thermal motion and hence fall under the laws of equilibrium statistical mechanics, granular systems formed of millimetre-sized particles must be shaken up to induce motion. For some vibration parameters, a so-called *vibro-fluidised* steady state can be reached in which the energy injected by the vibration is dissipated as heat (and sound) in the collisions. Such systems are clearly out of equilibrium and should in principle obey very different physics than the thermal ones. Yet, it has been shown that in some regimes, vibro-fluidised quasi-2D granular systems behave very closely to thermal systems [194, 195]. Using a realistic granular model, taking into account friction, deformation and dissipation of the beads, we performed molecular dynamics simulations of systems mimicking the thermal situation of spheres on a plane. Preliminary results shown in Figure III.17, left out of this thesis, suggest that the analogy with the thermal systems could hold so far as allowing self-assembly of a dodecagonal quasicrystal in a granular system.

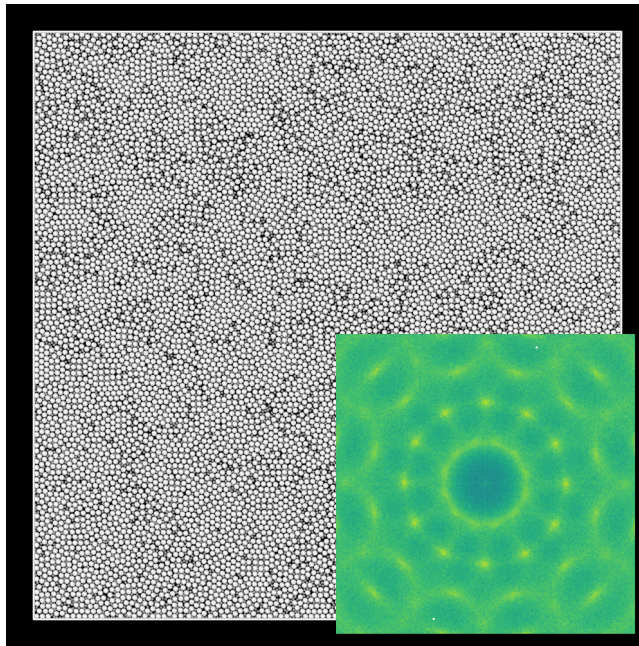


Figure III.17: Last snapshot of a molecular dynamics simulations of a vibro-fluidised mixture of steel beads of diameters 1.19 mm and 2.5 mm. The self-assembled structure exhibits a 12-fold symmetric diffraction pattern, shown in the inset, and the contact graph of large beads shows extended regions of square-triangle tilings. Could a dodecagonal quasicrystal form spontaneously at the granular scale?

Résumé en français

Découverte des quasicristaux

Le 8 avril 1982, Dan Shechtman conduit des expériences routinières de microscopie électronique sur des échantillons d'alliages d'aluminium au Bureau National des Standards (USA). Le diagramme de diffraction d'un des échantillons le plonge dans une grande perplexité. En effet, le diagramme de diffraction de l'échantillon 1725 semble avoir une symétrie d'ordre 10. Bien formé à la cristallographie, Schechman sait bien que les cristaux périodiques peuvent adopter uniquement l'un des "symétrie cristallographiques", c'est à dire d'ordre 1, 2, 3, 4 ou 6. Mais il sait aussi que le zoo cristallographique abrite des bêtes étranges, et se lance dans une étude plus poussée de l'échantillon, suspectant que l'apparent symétrie d'ordre 10 pourrait être causée par une macle (une association de plusieurs cristaux dans plusieurs orientations). Mais ces recherches supplémentaires l'amènent à la conclusion que la macle n'est pas une solution satisfaisante. L'échantillon 1725 est un nouveau type de matériau, le premier d'une longue série présentant de nouvelles symétries qui allaient provoquer un changement de paradigme en cristallographie.

En effet, avant la découverte de Shechtman, la cristallographie traitait ordre et périodicité comme équivalents [2]. Les matériaux ordonnés étaient supposés être des cristaux périodiques, qui pouvaient être décrits comme une répétition périodique d'un motif de base : la *cellule unitaire*. Un argument géométrique élémentaire montre alors que les seules symétries de rotations autorisées dans ce cas sont les fameuses symétries "cristallographiques". Quelques structures étaient déjà connues qui déviaient du cas périodique idéal. Par exemple, dans les *phases modulées incommensurables*, les positions des sites atomiques d'une structure périodique sont modulées par une fonction périodique dont la période est incommensurable avec le paramètre de maille de la structure de base [3–5], produisant une structure globalement aperiodique. Quelques exemples étaient aussi connus où l'occupation, ou la nature chimique des sites sont modulés [6]. De même, quelques *composites incommensurables* étaient connus. Ces systèmes sont composés de plusieurs sous-structures périodiques interagissant faiblement, avec des paramètres de maille incommensurables [7]. Dans ces deux cas, le diagramme de diffraction est composé de pics de Bragg. La modulation se manifeste par la présence de pic "satellites" supplémentaires autour des pic prin-

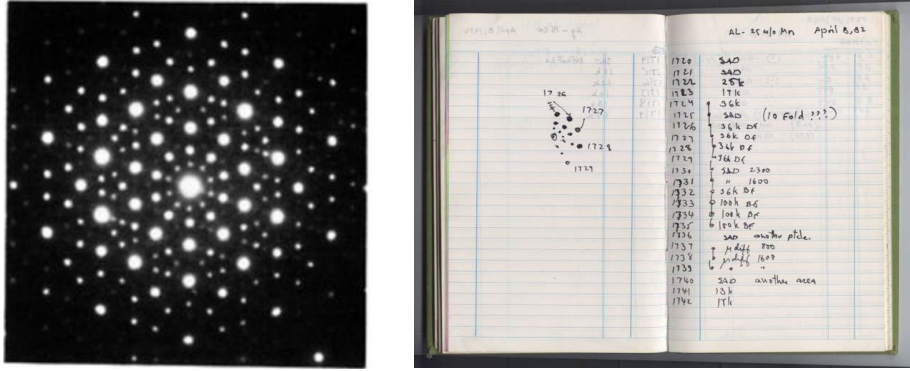


Figure III.18: (Gauche) Diagramme de diffraction électronique d'un alliage d'aluminium et manganèse le long de l'axe de symétrie 10. Extrait de la référence 1. (Droite) Carnet de bord de Shechtman à la page du 8 avril 1982, montrant l'annotation perplexe à propos de la symétrie d'ordre 10 de l'échantillon 1725. Propriété de Dan Shechtman.

cipaux qui correspondent à la structure périodique de base [8, 9]. Bien qu'elles auraient pu suggérer l'existence d'ordre sans périodicité, ces structures étaient considérées comme de rares curiosités, et comme, dans tous les cas, elles pouvaient être facilement reliées à des structures périodiques de base, leur existence ne remettait pas en question l'équivalence établie entre ordre et périodicité.

Dans le diagramme de diffraction mesuré par Shechtman et reproduit en Figure III.18-gauche, il n'est pas possible d'identifier un ensemble de pics principaux accompagnés de satellites. Ainsi, la structure ne peut pas être comprise comme une modulation d'une structure périodique sous-jacente. Cependant, la présence de pics de Bragg prove la nature très ordonnée du solide. La clef pour comprendre ces résultats fut trouvée dans des recherches antérieures sur les pavages en mathématiques. Dans les années 70, Penrose a étudié une famille de pavages qui portent maintenant son nom. Une portion d'un pavage de Penrose en deux dimension est présenté en Figure III.19. Le pavage est formé de deux tuiles, un rhombe obtus et un aigu. Ces tuiles peuvent être décorées avec des particules (par exemple en mettant une particule à chaque sommet des tuiles) pour créer une structure aperiodique mais ordonnée. Plusieurs tentatives de construction de structures atomiques

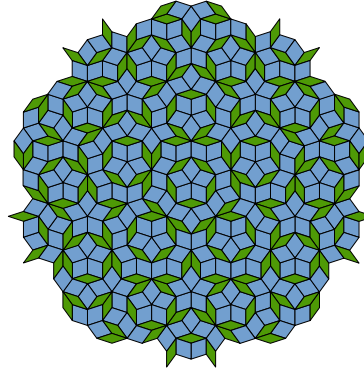


Figure III.19: Pavage de Penrose formé de deux tuiles. Le pavage est aperiodique, mais ordonné. Il possède une symétrie rotationnelle d'ordre 5.

réalistes basées sur le pavage de Penrose ont précédé la découverte de Shechtman [11, 12]. Mackay a construit un modèle atomique basé sur une version 3D du pavage et mesuré son diagramme de diffraction directement à l'aide d'un diffractomètre [13]. Finalement, Levine et Steinhardt furent les premiers à reconnaître dans l'échantillon de Shechtman la première réalisation expérimentale d'un cristal aperiodique [14]. Ils calculèrent le diagramme de diffraction d'une structure basée sur une généralisation en trois dimensions du pavage de Penrose et montrèrent que les pics correspondaient exactement à ceux trouvés dans les mesures expérimentales, et baptisèrent *quasicristal* ce nouveau type de matériaux ordonnés mais non périodiques. Un récit de première main de cette histoire par Steinhardt peut être trouvé dans la Référence 15.

La découverte du premier quasicristal a rencontré un certain scepticisme dans les rangs des cristallographes. En effet, la précision des mesures de Shechtman ne permettait pas d'exclure certaines configurations complexes de macles [16]. Rapidement, cependant, d'autres quasicristaux furent découverts dans d'autres alliages métalliques [17–19], établissant leur existence sur des bases plus convaincantes. En 1992, la Commission des Cristaux Aperiodiques de l'Union Internationale des Cristallographes proposa une nouvelle définition de *cristal* comme “un solide possédant un diagramme de diffraction essentiellement discret”, qualifiant de ce fait les quasicristaux comme des cristaux de plein droit.

Quasicristaux en matière molle

Avant les années 2000, tous les quasicristaux connus avaient été découverts dans des alliages de métaux. En 2004, Zeng *et al.* ont découvert un quasicristal dodécagonal (symétrie d'ordre 12) dans un système de micelles [38]. Cette trouvaille introduit les quasicristaux dans le champ de la physique de la matière molle, qui s'intéresse aux systèmes dont les constituants élémentaires sont bien plus grands que des atomes (nanoparticules, macromolécules, colloïds etc...). L'interaction entre les constituants de base des systèmes de matière molle est typiquement plus faible que les interactions fortes qui lient les atomes entre eux dans les solides. De ce fait, la densité d'énergie et le module élastique de ces assemblages sont typiquement assez faibles, produisant des matériaux “mous” comme des gels, pâtes ou cristaux liquides⁹.

Les quasicristaux en matière molle sont rapidement devenus un sujet de recherche actif. En effet, leur nature ordonnée combinée avec leur symétries exotiques promettent d'intéressantes propriétés optiques [39–42], qui se manifestent quand la longueur d'onde de la lumière incidente est comparable aux distances typiques dans le matériau. Dans les quasicristaux métalliques, les constituants pertinents sont les atomes, qui interagissent principalement avec les rayons X. Pour utiliser les propriétés des quasicristaux à des longueurs d'onde plus grandes, des constituants de bases plus gros, comme ceux trouvés dans les systèmes de matière molle sont nécessaires.

⁹Daan Frenkel définit parfois la matière molle comme “tout ce qui ne passe pas les contrôles de sécurité à l'aéroport”

Depuis la découverte de Zeng *et. al.*, d'autres quasicristaux ont été observés dans des systèmes de matière molle remarquablement différents [46–50]. La nature des constituents (micelles ou nanoparticules, aussi bien que leur propriétés chimiques (micelles de nature très différente), semble importer peu à l'émergence de l'ordre quasi-cristallin. La taille des constituents élémentaires varie de presque deux ordres de grandeur entre les micelles de silice [47] (quelques Angströms) et les polymers étoilés [48] (plusieurs dizaines de nanomètres), et pourtant ces systèmes forment des quasicristaux très similaires. Cela suggère qu'au delà des détails des interactions microscopiques, des mécanismes généraux stabilisent les quasicristaux dans les systèmes de matière molle. Cette thèse est une contribution aux tentatives d'élucidation de ces mécanismes.

Simulations numériques

Les simulations numériques sont un outil de choix pour aborder ces questions. En particulier, nous utilisons des simulations d'auto-assemblages, qui peuvent être imaginées comme de véritables expériences numériques. En effet, on commence par préparer le système dans un état initial contrôlé (composition, densité...). Ensuite, la simulation est démarrée, qui fait évoluer les systèmes selon la dynamique choisie, et des mesures sont prises qui fournissent des données brutes sur lesquelles des analyses seront ensuite effectuées. A l'image d'une expérience réelle, la simulation donne accès au comportement réel du système, sans approximation. A la différence de la plupart des expériences traditionnelles en revanche, les données brutes collectées contiennent toute l'information microscopique du système (position et vitesse de toutes les particules), ce qui permet une analyse très détaillée. Le prix à payer pour cette précision est que les systèmes étudiés sont généralement très petits (typiquement jusqu'à 10^8 particules, à comparer avec les 10^{23} qui forment un échantillon macroscopique), et simulés sur des temps réels très courts. De plus, les simulations traitent de systèmes modèles. Ceci est à la fois une force et une faiblesse, selon l'ambition du physicien ou de la physicienne. D'un côté, le système modèle n'existe jamais tel quel dans le monde des expériences sensibles (par exemple, il n'existe pas d'objet parfaitement sphérique et dur) et les tentatives de reproduire des interactions réalistes dans des systèmes complexes produisent typiquement des simulations incroyablement compliquées et coûteuses en ressources de calcul, pour des comparaisons souvent décevantes avec les expériences. D'un autre côté, les simulations numériques peuvent se révéler extrêmement précieuses quand elles sont utilisées sur des systèmes simples, car on peut alors épurer le modèle jusqu'à ne garder que quelques ingrédients clef, et obtenir le comportement exact de ce système idéalisé. Si le phénomène d'intérêt (par exemple la formation d'un quasicristal) persiste, le modèle minimal fournit des indices précieux sur les mécanismes fondamentaux à l'oeuvre.

Un très grand nombre de simulations se sont attachées à la formation des quasicristaux. On peut grossièrement les classer en deux groupes, selon que les différents longueurs nécessaires à l'ordre quasipériodique sont obtenus par

un mélange de plusieurs types de particules [72–77], ou intégrées dans un potentiel d'interaction plus complexe pour un système ne contenant que un type de particules [22, 63, 78–93]. Certaines études ont aussi étudié la possibilité de remplacer une longueur caractéristique par une contrainte sur les angles de liaison des particules, en simulant des particules munies de patches attractifs directionnels [94–100]

Un modèle minimal pour les quasicristaux

La plupart des observations de quasicristaux dans des systèmes de matière molle sont le fruit du hasard. Concevoir un système expérimental pour l'auto-assemblage de quasicristaux reste très ardu. Pourtant, un système colloidal simple dans lequel des quasicristaux se formerait de manière robuste et reproductible serait très précieux car il offrirait une fenêtre sur la dynamique des quasicristaux en temps réel, dans l'espace direct à l'échelle micrométrique. Une telle plateforme expérimentale est indispensable pour attaquer plusieurs questions ouvertes quant à la nucléation et la croissance des quasicristaux, ou la dynamique de leur défauts particuliers par exemple. La grande variété de simulations numériques passées ont exploré la possibilité d'auto-assemblage de quasicristaux dans de nombreux systèmes modèles, mais la plupart d'entre eux sont difficilement réalisable expérimentalement.

A l'inverse, des colloïds durs peuvent aujourd'hui être produits avec un grand contrôle sur la taille [103–105]. Ces particules sont extrêmement bien modélisées par de simples sphères dures, au point que les simulations et les expériences concordent quantitativement dans une grande gamme de paramètres [106, 107]. Motivés par cette possibilité expérimentale et prenant la suite des travaux de Likos et Henley qui ont montré l'existence d'un quasicristal dodécagonal dans des mélanges binaires de disques durs à pression infinie [74], notre travail étudie l'auto-assemblage de quasicristaux dans des mélanges binaires de sphères dures. Comme tous les quasicristaux de matière molle observés à l'heure actuelle dans des expériences possèdent un ordre quasipériodique en deux dimensions seulement, notre étude se focalise sur les systèmes 2D et considère des mélanges de sphères dures confinées à une interface. Cette géométrie est similaire à celle utilisée par Talapin *et. al.*, qui ont observé la formation d'un quasicristal dodécagonal dans un mélange binaire de nanoparticules.

Un mélange de sphères dures confinées à une interface peut être transformé en un système 2D équivalent de disques durs, en considérant la projection des particules sur le plan de l'interface (voir Figure III.20). En général, des particules composées de matériaux différents ont des propriétés de mouillage différentes avec l'interface fluide et reposeront donc à des hauteurs différentes. Dans la configuration 3D, une petite sphère peut alors glisser légèrement en dessous (ou au dessus) d'une grande avant qu'un contact n'ait lieu. Cela se traduit dans le système 2D équivalent par une distance de contact entre les petits et grands disques inférieure à la somme de leurs rayons. Les sphères d'un même type reposent toutes à la même hauteur et se comportent donc comme des disques

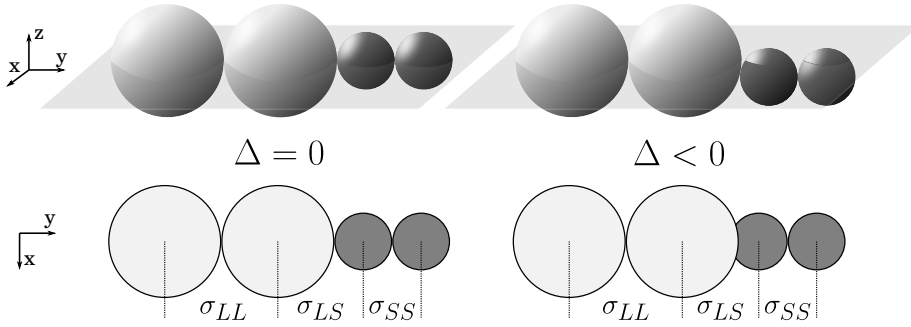


Figure III.20: Un mélange binaire de sphères dures confinées à une interface (haut) peut être décrit par un système équivalent de disques durs en 2D, en considérant la projection des sphères sur le plan de l'interface (bas). Si les particules de différents types reposent à des niveaux différents par rapport à l'interface, à cause d'angle de mouillage différents avec les fluides par exemple, la distance de contact entre les petits et grands disques devient plus petite que la somme des rayons des sphères correspondantes. Le système modèle ainsi obtenu est un mélange de disques durs *non-additifs*.

durs standard dans le système 2D équivalent. Dans ce modèle très simple, les interactions qui pourraient résulter des déformations de l'interface sont ignorées. Le modèle 2D équivalent est appelé mélange binaire de disque durs *non-additifs*, et constitue le système exclusif des travaux présentés dans cette thèse.

Le diagramme de phase des mélanges binaires de disques durs additifs à pression infinie a été étudié par Likos et Henley dans les années 90 [74]. Ils ont montré que, même à pression infinie, ce système simple peut former un quasicristal dodecagonal, et suggèrent dans leur publication l'étude de systèmes non-additifs comme une extension naturelle de leurs travaux. Dans le premier chapitre de cette thèse, nous suivons leurs pas et explorons le diagramme de phase à pression infinie des mélanges de disques durs non-additifs. En améliorant l'échantillonnage des structures candidates, nous trouvons de nouvelles phases stables qui n'étaient pas considérées précédemment et montrons que l'introduction de la non-additivité promeut la zone de stabilité du quasicristal.

Dans le second chapitre, la contrainte de pression infinie est relâchée et des simulations directes d'auto-assemblage sont conduites à pression finie. Cette étude confirme que le quasicristal dodecagonal prédit à pression infinie peut aussi se former spontanément dans des conditions réalistes. Nous rapportons aussi l'auto-assemblage d'un nouveau quasicristal octagonal dont la composition peut être continuellement variée tout en préservant la symétrie non cristallographique d'ordre 8.

Le troisième chapitre explore en détail la stabilité du quasicristal dodecagonal à l'aide de calculs numériques d'énergie libre. Ces calculs nous permettent de tracer un diagramme de phase essentiellement exact pour notre système, et

prouvent que le quasicristal dodécagonal est bien thermodynamiquement stable. Enfin, à l'aide de calculs d'énergie libre de grande précision, nous évaluons quantitativement la validité de l'hypothèse de pavage aléatoire, utilisée plus tôt dans cette thèse à plusieurs reprises.

Appendix A

Infinite pressure phases

Phases drawn in Figure I.2 depict the structures at “magic ratios” where they are highly symmetric, with a large number of contacts between the disks. When the size ratio q deviates from those values, structures are deformed, bonds are broken and some symmetries are lost while others are gained. This appendix provides additional details on the magic ratios of these phases, and the deformations they undergo at infinite pressure as a function of size ratio.

A.1 Magic ratios

In Table A.1, we provide numerical values for the various magic ratios for $\Delta = 0, -0.03, -0.05$ and -0.1 . Each crystal structure has several magic ratios associated with its deformation path. For example, $q_{T2.2}$ is the magic ratio for crystal structure T2, with index 2. Note that some magic ratios that carry different labels are actually identical.

A.2 Deformation paths

In Figures A.1 to A.8, we present deformation paths for the phases that appear in the phase diagrams, in which we highlight how the contacts between particles (red lines) are changed upon deformation between different magic size ratios. In some cases, multiple paths are possible, which will have different volumes per particle depending on the exact choice of size ratio and non-additivity parameter.

All deformations are obtained from Floppy Box Monte Carlo simulations [124]. Some structures that have the same composition x_S can deform continuously one into the other. We still give them separate names to conform to the naming scheme of Ref. 74. In such cases, the deformation paths are linked together and each phase corresponds to one portion.

label	$\Delta = 0$	$\Delta = -0.03$	$\Delta = -0.05$	$\Delta = -0.1$
$qT_{1.0}$	0.155	0.190	0.215	0.283
$qT_{1.1}$	0.281	0.308	0.327	0.376
$qT_{2.0}$	0.101	0.124	0.140	0.183
$qT_{2.1}$	0.216	0.220	0.224	0.235
$qT_{2.2}$	0.349	0.335	0.326	0.304
$qT_{3.0}$	0.082	0.101	0.115	0.152
$qT_{3.1}$	0.119	0.131	0.139	0.163
$qT_{3.2}$	0.233	0.224	0.219	0.205
$qT_{4.0}$	0.349	0.335	0.326	0.304
$qT_{4.1}$	0.308	0.319	0.326	0.344
$qS_{1.0}$	0.155	0.190	0.215	0.283
$qS_{1.1}$	0.414	0.458	0.489	0.571
$qS_{2.0}$	0.101	0.124	0.140	0.183
$qS_{2.1}$	0.217	0.238	0.252	0.290
$qS_{2.2}$	0.369	0.372	0.374	0.381
$qS_{2.3}$	0.620	0.590	0.571	0.525
$qS_{3.0}$	0.187	0.204	0.217	0.250
$qS_{3.1}$	0.473	0.453	0.439	0.407
$qS_{4.0}$	0.073	0.090	0.102	0.136
$qS_{4.1}$	0.199	0.162	0.149	0.131
$qS_{4.2}$	0.136	0.149	0.156	0.175
$qS_{4.3}$	0.288	0.284	0.281	0.272
$qS_{5.0}$	0.244	0.248	0.251	0.260
$qS_{5.1}$	0.389	0.373	0.363	0.337
$qH_{1.0}$	0.533	0.536	0.538	0.543
$qH_{1.1}$	1	0.942	0.905	0.818
$qH_{2.0}$	0.638	0.669	0.691	0.748
$qH_{3.0}$	0.101	0.124	0.140	0.183
$qH_{3.1}$	0.386	0.404	0.416	0.448
$qH_{3.2}$	1	0.942	0.905	0.818
$qH_{4.0}$	1	0.942	0.905	0.818
$qSh_{1.0}$	0.101	0.124	0.140	0.183
$qSh_{1.1}$	0.545	0.571	0.589	0.636

Table A.1: “Magic” size ratios where the various crystal structures exactly accommodate a specific set of contacts between neighbours.

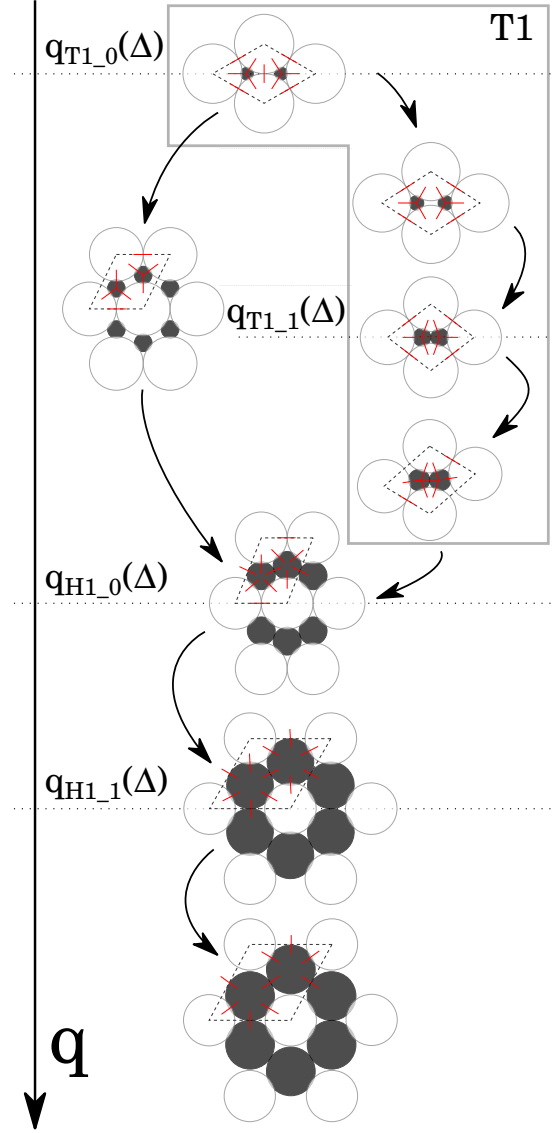


Figure A.1: T1 and H1 deformation paths. Both phases have the same composition and can continuously deform one into the other at $q = q_{H1_0}(\Delta)$. We call T1 the branch of the path in the grey frame. The other portions are labelled H1.

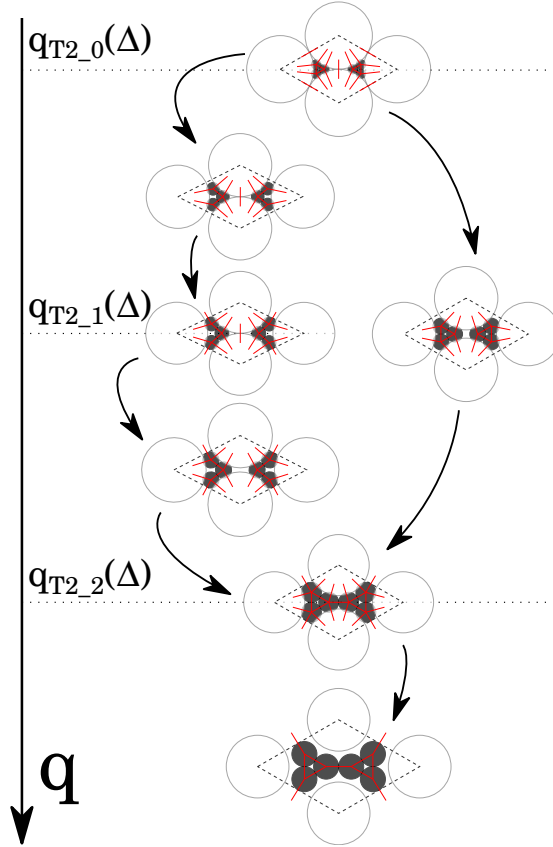


Figure A.2: T2 deformation path. There are two ways to expand the unit cell above $q_{T2_0}(\Delta)$. The right branch takes over the other in terms of volume per particle at a size ratio between $q_{T2_0}(\Delta)$ and $q_{T2_2}(\Delta)$, that does not correspond to a magic ratio. We decide to keep the same name T2 for both branches to lighten the naming scheme.

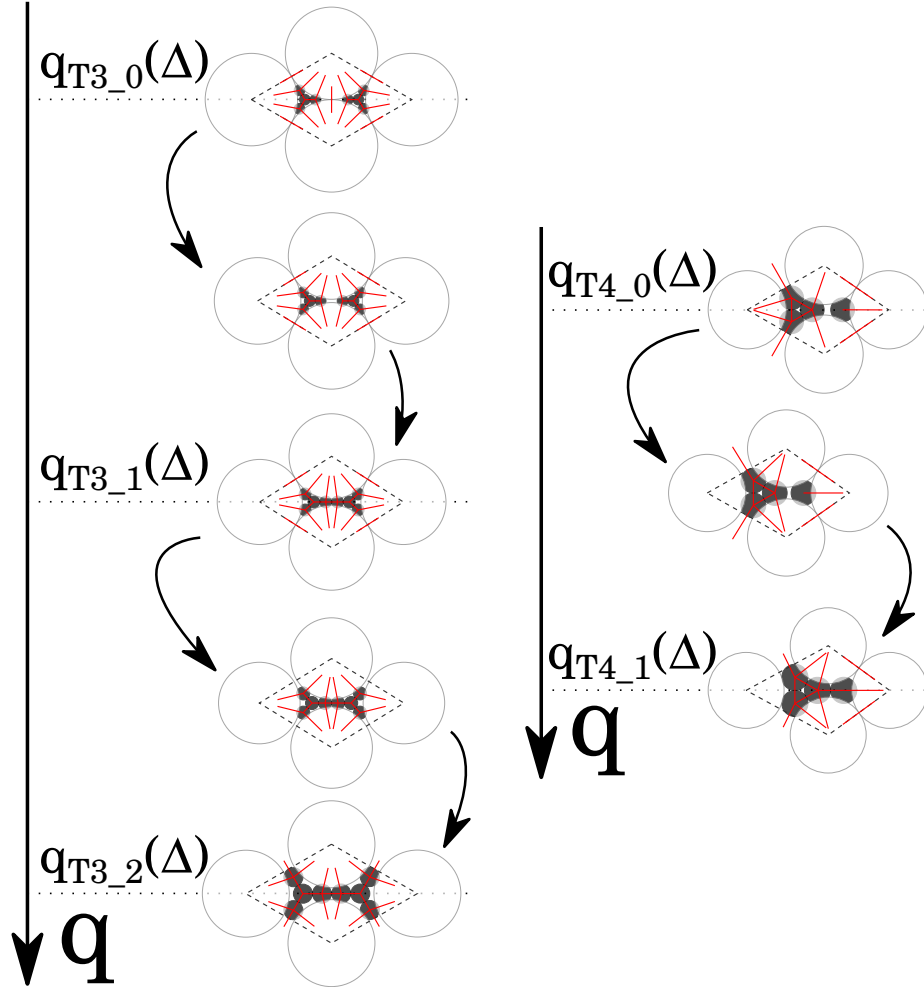


Figure A.3: T3 (Left) and T4 (Right) deformation paths.

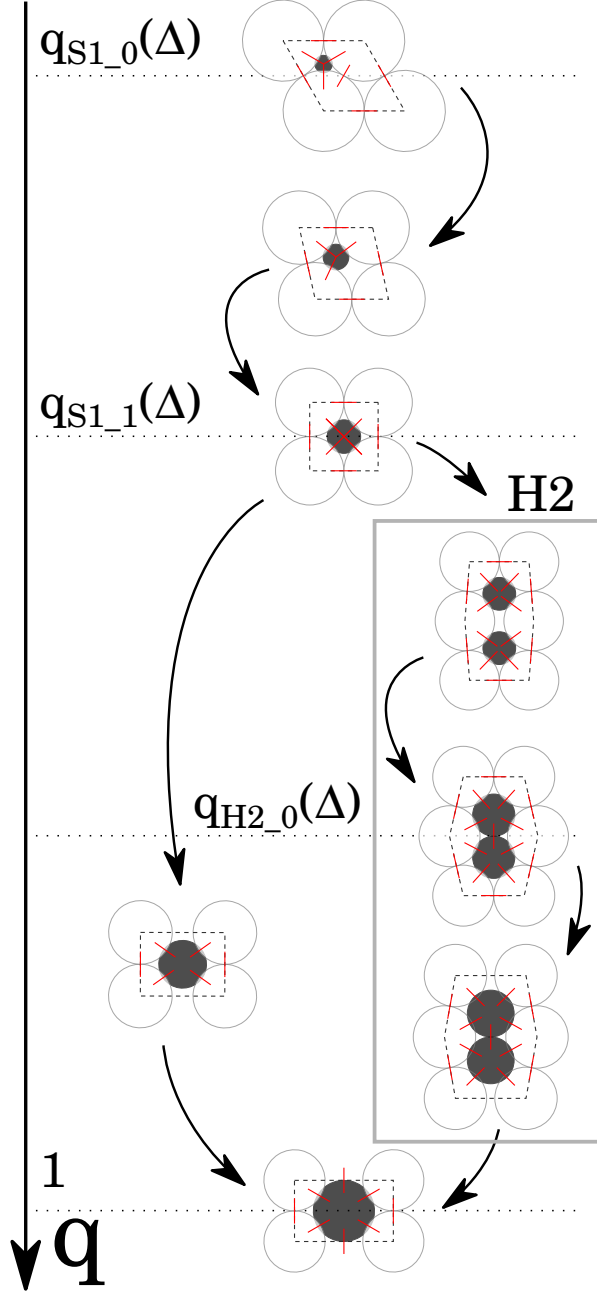


Figure A.4: Deformation paths of S1 and H2 structures. We label H2 the branch that deforms the unit cell beyond $q_{S1_1}(\Delta)$ by breaking one contact between large disks. The rest of the path is labelled S1.

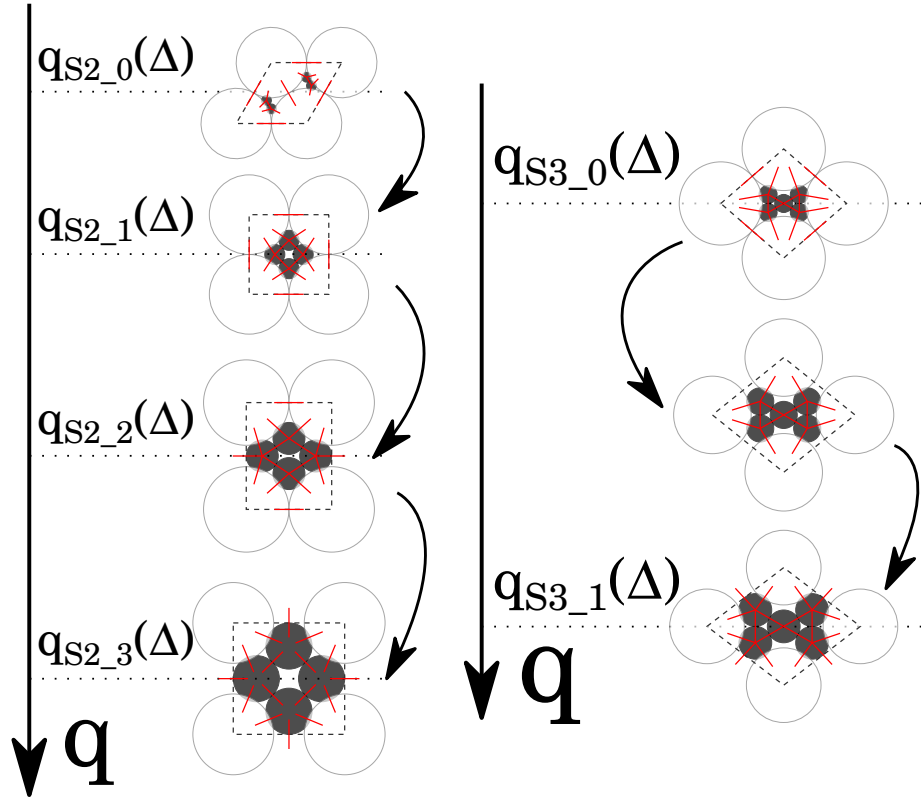


Figure A.5: S2 (Left) and S3 (Right) deformation paths.

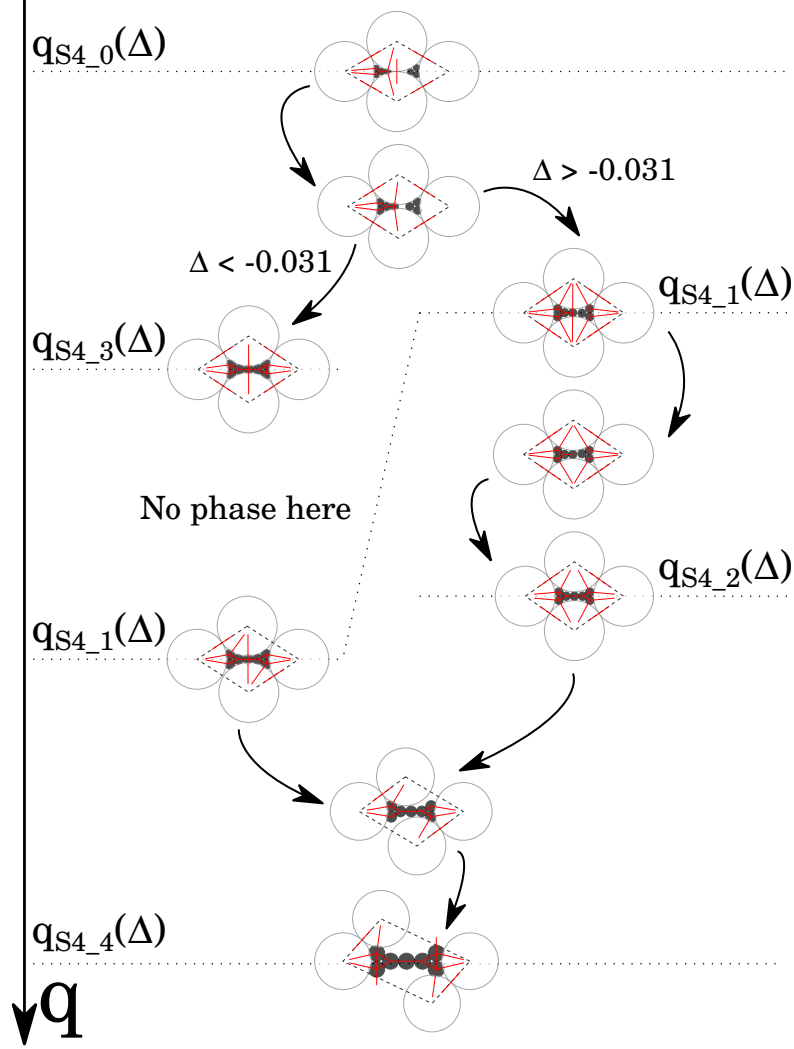


Figure A.6: S4 deformation path. Depending on the non-additivity parameter Δ , different contacts occur first as the small disks are inflated, leading to two possible deformation branches. On the left branch ($\Delta < -0.031$), we could not find a deformation linking the S4 structure at $q_{S4_3}(\Delta)$ and $q_{S4_1}(\Delta)$

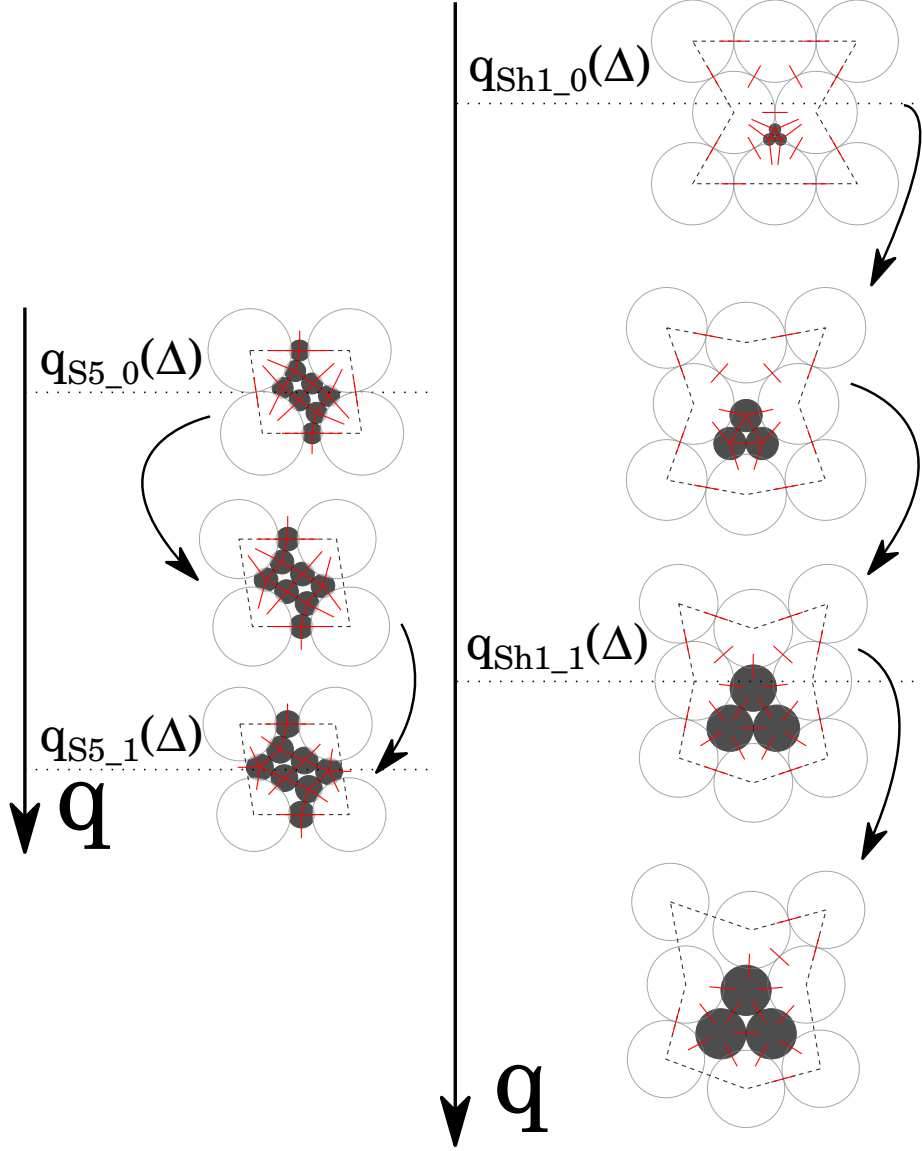


Figure A.7: S5 (Left) and Sh1 (Right) deformation paths.

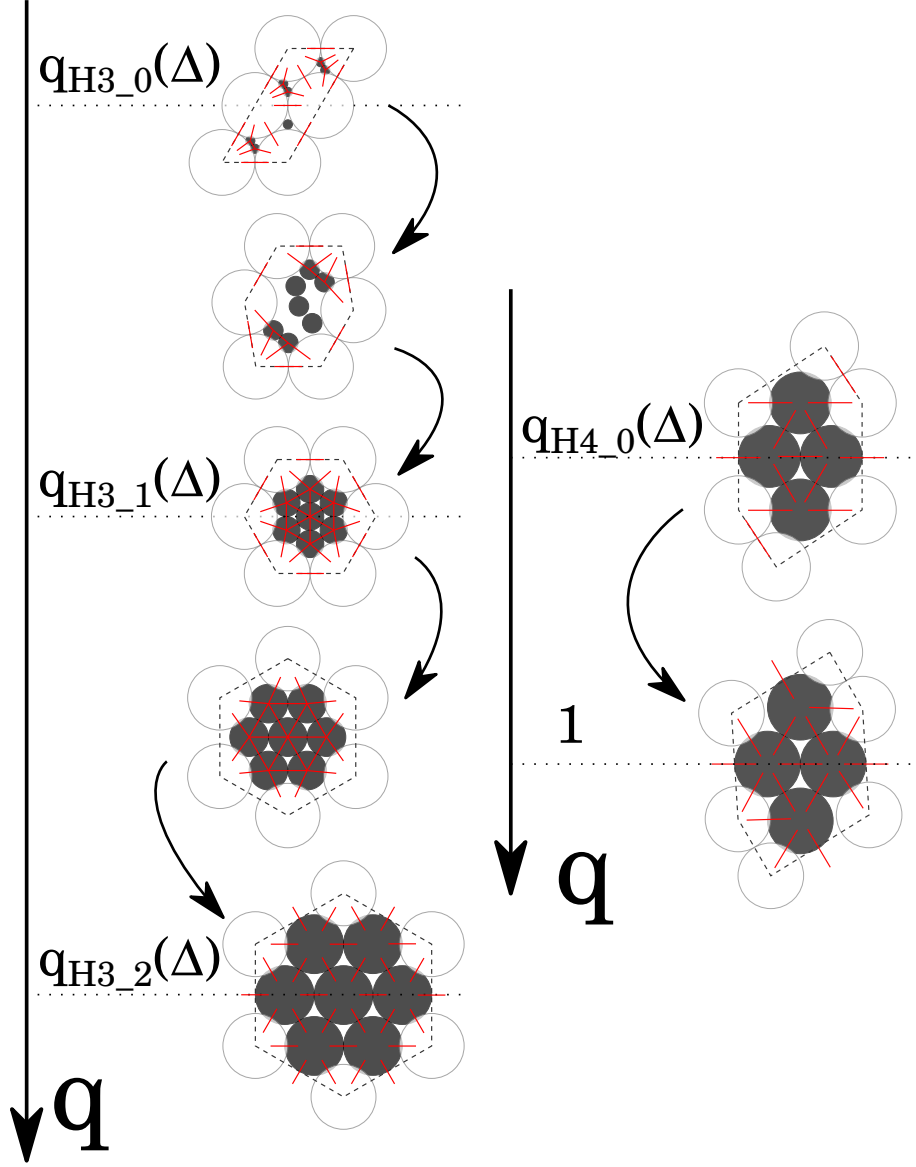


Figure A.8: H3 (Left) and H4 (Right) deformation paths.

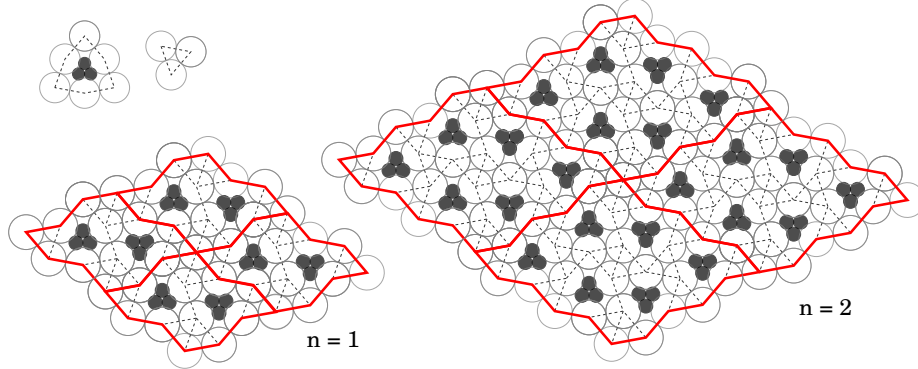


Figure A.9: The two first iterations of an (infinite) family of periodic structures with shield and triangular tiles (upper-left). They have the same volume per particle as the coexistence of Sh1 and Hex_L at the same fraction of small disks p .

A.3 Shield-triangle structures

The Sh1 unit cell can be decomposed into a shield-shaped tile and triangular Hex_L tiles. Those tiles can be combined without volume-per-particle cost for $q \leq q_{Sh,0}(\delta)$ (see Figure A.9). While these shields and triangles do not allow random tiling of the plane, they can be combined into a family of periodic structures with larger and larger unit cells[137]. In Figure A.9 we show the two first members ($n = 1$ and $n = 2$) of an infinite family of periodic structures that exist for a fraction of small disks. In this family, the structure with index n has a composition

$$x_S(n) = \frac{3n(n+1)}{6n(n+1) + 1}. \quad (\text{A.1})$$

In the limit where $n \rightarrow \infty$ this converges to $x_S = 1/2$, and the phase becomes identical to the Sh1 phase. However, for small n , the composition is slightly smaller, as extra large particles are included at the crossing points of the red lines in Fig. A.9. Since this inclusion of Hex_L tiles comes without volume cost, structures within this family (or coexistences between them) are as stable as the Hex_L-Sh1 coexistence at infinite pressure at their respective compositions. Hence, there is a small region of many competing tilings at compositions between $x_S = 6/13$ and $1/2$ in the phase diagram in Figure I.4. However, we expect that vibrational entropy contribution will favour one of these crystals and simplify this region of the phase diagram, either in the infinite pressure limit, or in any case at finite pressures.

In our simulations, we only consider periodic crystals with up to 12 disks in the unit cell so the family of structures mentioned above is out of scope. However, we note that the existence of these complex structures suggests that

periodic structures with large unit cells may exist elsewhere, when unit cells of coexisting phases can be decomposed into a set of matching tiles that can tile the plane in a variety of ways, even if fully aperiodic tilings are not possible.

A.4 Calculations of the volumes per particle

Candidate crystal structures are sampled by Floppy-Box simulations for discrete values of the size ratio q and composition x_S . To draw the phase diagrams and get the exact range of stability of the different phases, we compute their volume per particle v along the deformation paths. To this end, we identify the disks in contact from the simulations, and write down a set of equations for the position of all the disks in the unit cell. Then, we use the symbolic library `sympy` [196] to obtain analytical expressions for the magic ratios, particle positions and the volume per particle of each structure as a function of q and Δ .

In some cases, `sympy` fails to solve the equation for the magic ratio. We then rely on a numerical solution. In the worst case (S4), we did not find analytical expressions for the position of the particles. For this case, we compute the positions numerically, deduce the volume per particle for a large number of (q, Δ) points and use 2D linear interpolation to estimate missing values.

Figure A.10 displays the packing fraction of the pure phases that appear in the additive phase diagram ($\Delta = 0$) in Figure I.4. Note that the best packing phase in these diagrams is not necessarily the stable phase, because a coexistence of two phases (not shown in the graph), could pack better at this composition.

Finding optimal deformations, even with guidance from Floppy-Box simulations, remains a challenging task. It can never be excluded that we missed some more optimal deformation paths, and indeed, in Figure A.11, we reproduce deformation paths for the T2 and H3 phases in the additive case, provided by Thomas Fernique in a private communication, which have a higher packing fraction than the ones presented above for $q \in]q_{T2.2}, 1[$ and $q < q_{H3.1}$ respectively.

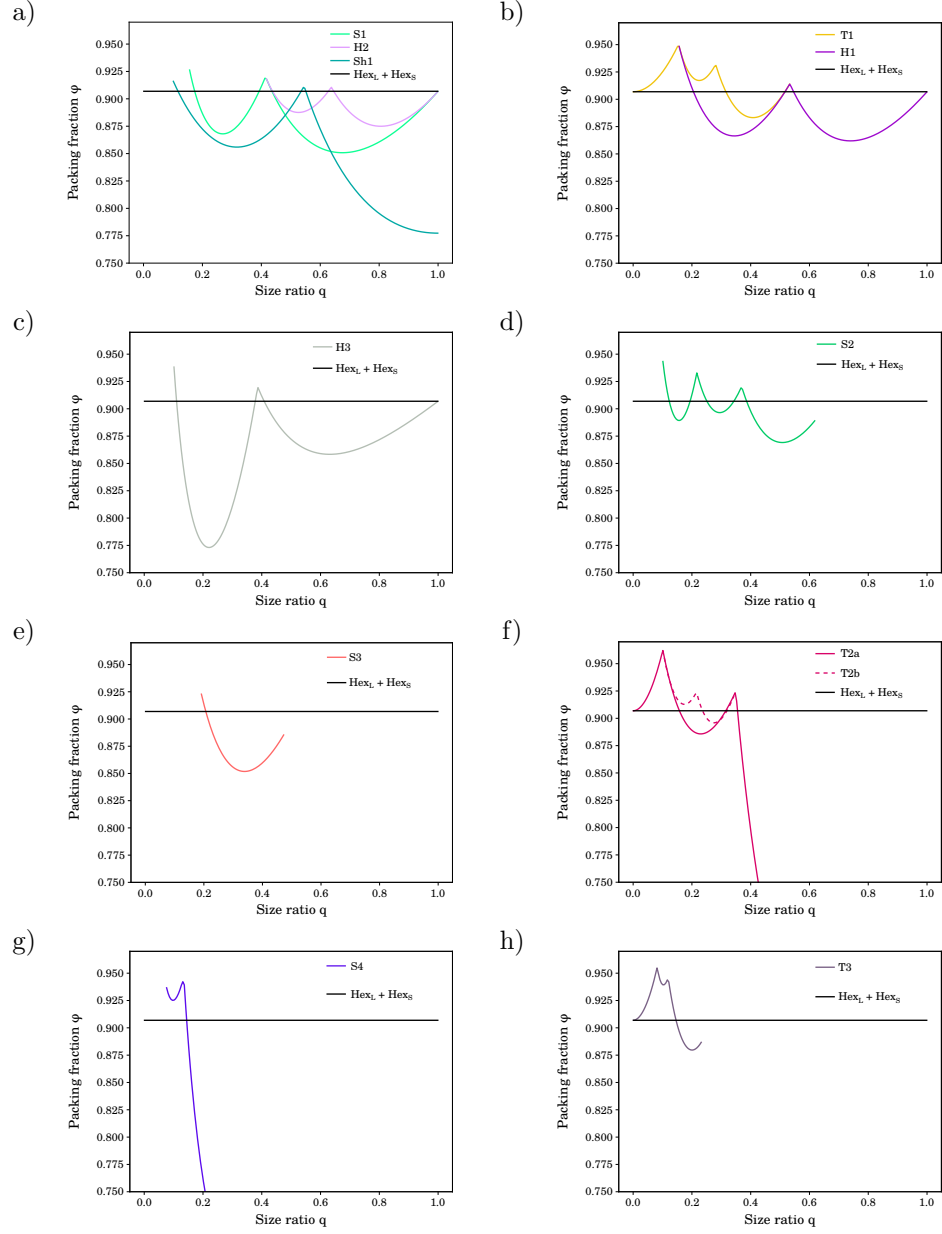


Figure A.10: Packing fraction of the pure phases at $\Delta = 0$, for compositions a) $x_S = 1/2$, b) $2/3$, c) $7/9$, d) $4/5$, e) $5/6$, f) $6/7$, g) $7/8$, and h) $8/9$.

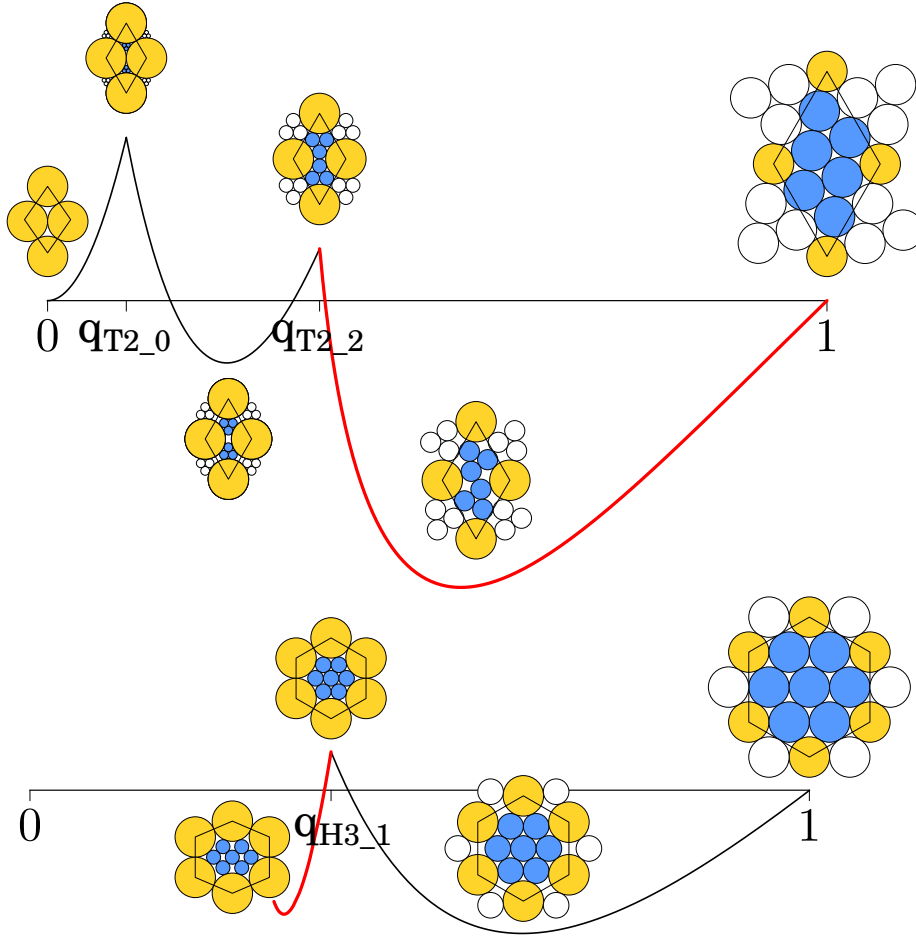


Figure A.11: Denser deformation paths found by Thomas Fernique for the T2 (Top) and H3 (Bottom) phases for $q \in]q_{T2.2}, 1[$ and $q < q_{H3.1}$ respectively (red thick lines).

Appendix B

Automatic detection of non-equilibrated simulations

Our work relies heavily on measuring equilibrium quantities from simulation snapshots containing the position and – in the case of molecular dynamics simulations – velocities of all the particles. Under the assumption that the system is ergodic and at equilibrium, the time averages taken from simulations are the same as ensemble averages.

The ergodicity hypothesis is not very easy to assess, and rarely checked in practice. The equilibrium hypothesis is easier to verify, and usually checked by looking at a property versus simulation time plot. If the quantity fluctuates around a mean value, the system is assumed to be at equilibrium. If a drift is observed in curve, the simulation has not reached equilibrium yet.

This visual verification works fine, but quickly gets impractical when the number of simulations grows. This section presents attempts made at automating the detection of non-equilibrated simulations. To benchmark the methods, I use data from a Monte Carlo measurement of an equation of state for a binary mixture of non-additive hard disks. The volume is recorded as a function of simulation time for various pressures in $[0.05 \, k_B T \sigma_L^{-2}, 45 \, k_B T \sigma_L^{-2}]$. At high pressures, the simulations are typically less equilibrated.

B.1 Linear fit

At equilibrium, thermodynamic quantities fluctuate around a constant mean. Therefore, a linear fit to an infinitely long measurement of an equilibrated quantity should yield a line of slope 0. Fitting an affine function to the data is essentially what one does when eyeballing at the curve to check whether a drift is present or not.

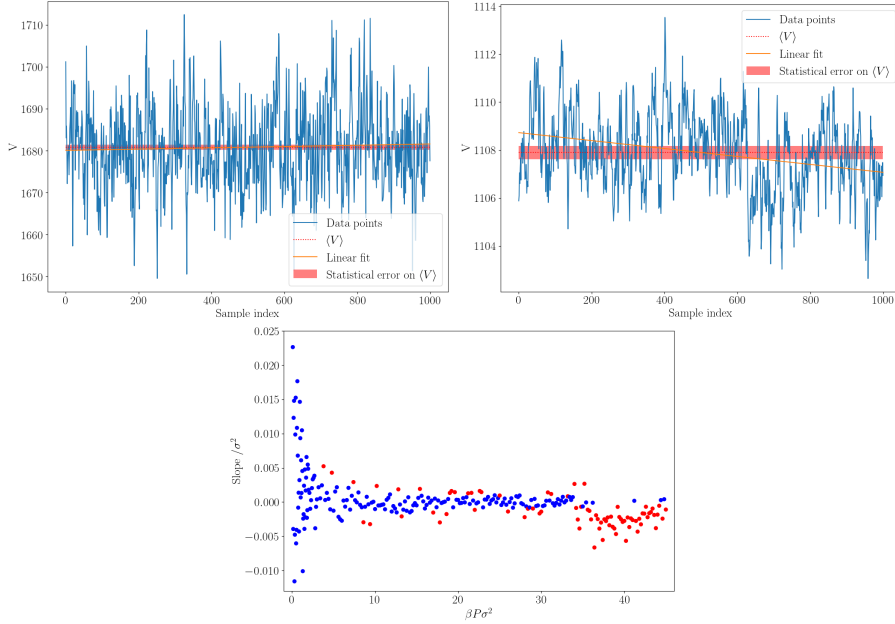


Figure B.1: Results of the linear fit on Monte Carlo measurement of the volume in a binary mixture of non-additive hard disks at pressures $5.3 k_B T \sigma_{LL}^{-2}$ (left, equilibrated) and $42.2 k_B T \sigma_{LL}^{-2}$ (right, not equilibrated). The bottom plot shows the outcome of the classification on all points sampled for the equation of state. Blue and red points are classified as equilibrated and non-equilibrated respectively.

The x-axis is arbitrary, and simply taken as the index of the sample in the data set. The fit function returns both fit parameters and standard error. The standard error is multiplied by a factor to obtain the confidence interval for the slope. The factor is computed from a Student's t-distribution adapted to the size of the data set. Finally, if zero does not lie within the slope error bars, the system is assumed to be out of equilibrium. The output of the method is illustrated in Figure B.1.

The confidence level used in the error bar determination gives the probability that the true slope lies within the error bars. It can be used to adapt the strictness of the test. The smaller the confidence level, the smaller the error bars, thus the stricter the test.

For the equation of state data, the method allows to clearly identify that simulations of pressure above $\sim 33 k_B T \sigma^{-2}$ have not reached equilibrium. However, at lower pressures, some simulations are classified as not equilibrated although visual inspection suggests they are. Increasing the size of the confidence interval reduces this effect, but does not suppress it.

This method yields decent results. It corresponds to a relatively direct im-

plementation of the manual process. It would however fail spectacularly in some pathological cases such as sampling that would be symmetrical around the middle of the x-axis. This could occur with long wavelength fluctuations for instance, although this should be pretty rare.

We use this method to assess equilibration in the Frenkel-Ladd calculations, as discussed in section III.4. The next two sections describe a failed attempt at solving the same problem using a normality test, and suggestion of a possible better solution using block averages.

B.2 Normality test

The thermodynamic quantities of a system at thermal equilibrium can be represented as random variables following a Gaussian distribution whose mean and width are physically meaningful quantities.

To assess equilibration of a system, one could use a statistical test to see whether the measured points can reasonably be assumed to have been drawn from a normal distribution.

The Shapiro-Wilk test computes a p-value for the null hypothesis that the samples were drawn from a normal distribution. P-values are strange objects, and interpretations should be made with extreme care. The p-value of the Shapiro-Wilk test is the probability that a set of points drawn from a normal distribution would have displayed a behaviour at least as extreme as the observed one. Typical use of p-values involve setting a-priori a threshold value and rejecting the null hypothesis if the computed p-value is smaller than the threshold.

This method does not work well. This might be due to time correlations between samples. Indeed, the samples are not exactly drawn from a normal distribution when snapshots are dumped too often. A way around this would be to prune the data set to keep only uncorrelated samples. The mixing time can be obtained from the Flyvbjerg-Peterson (or block average) analysis.

B.3 Block averages

In a time sequence of equilibrated simulation snapshots, samples are usually correlated. To measure meaningful errors on the calculated means, we routinely use Flyvbjerg-Peterson (or block-average) analysis [145, 188]. This works great and allows us to detect whether the simulation was long enough to decorrelate or not by looking at the appearance of a plateau in the standard error on mean computed on block averages.

The plateau typically doesn't appear when the simulation is not equilibrated. Instead, the standard error grows monotonically.

Figure B.2 displays the Flyvbjerg-Peterson analysis for equation of state simulations at $P = 4.8 k_B T \sigma^{-2}$ and $P = 44.8 k_B T \sigma^{-2}$. The first one would reasonably be classified as equilibrated and is not by the slope analysis, while the

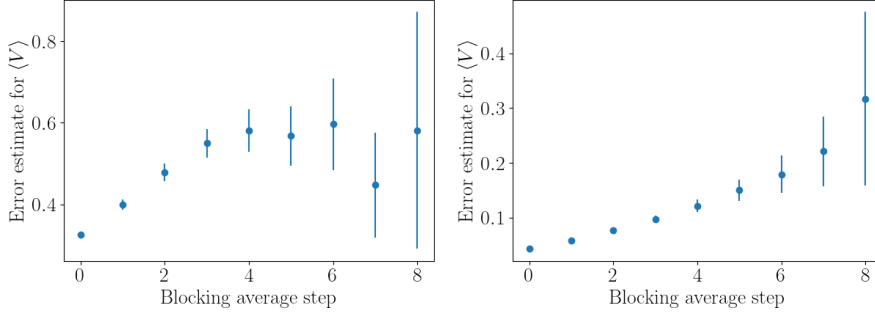


Figure B.2: Flyvbjerg-Peterson (or block average) analysis for equation of state simulations of non-additive hard disks at pressures $P = 4.8 k_B T \sigma^{-2}$ (left) and $P = 44.8 k_B T \sigma^{-2}$ (right). In the first case, a plateau appears indicating that equilibrium was reached, while in the second case, samples are still correlated.

second looks equilibrated (and is classified as such by the slope analysis) but is in fact still completely correlated, which means that no meaningful equilibrium quantities can be measured from it.

In both cases, the block average plot provides a clear indication. This suggests that detecting the plateau in the block averages is a more reliable method to assess equilibration. However, automatic plateau detection on curves with typically less than a dozen points seems tricky, and I did not implement it provided that the slope method provides good enough results.

Bibliography

- [1] D. Shechtman, I. Blech, D. Gratias, and J. W. Cahn, *Metallic Phase with Long-Range Orientational Order and No Translational Symmetry*, Phys. Rev. Lett. **53**, 1951 (1984).
- [2] R. Lifshitz, *Quasicrystals: A Matter of Definition*, Fond. Phys. **33**, 1703 (2003).
- [3] V. Daniel and L. Henry Solomon, *An X-ray study of the dissociation of an alloy of copper, iron and nickel*, Proc. R. Soc. Lond. A **181**, 368 (1943).
- [4] S. Tanisaki, *Microdomain Structure in Paraelectric Phase of NaNO_2* , J. Phys. Soc. Jpn. **16**, 579 (1961).
- [5] G. C. Dumbledam and P. M. de Wolff, *The average crystal structure of $\gamma\text{-Na}_2\text{CO}_3$* , Acta Crystallogr B Struct Sci **25**, 2665 (1969).
- [6] P. B. Jamieson, D. de Fontaine, and S. C. Abrahams, *Determination of atomic ordering arrangements from a study of satellite reflections*, J Appl Crystallogr **2**, 24 (1969).
- [7] C. K. Johnson, *Superstructure and modulation wave analysis for the uni-dimensional conductor hepta- (tetrathiafulvalene) pentaiodide*, J. Chem. Phys. **64**, 2271 (1976).
- [8] C. Janot, *Quasicrystals: A Primer* (Oxford Univ. Press, Oxford, 1998). OCLC: 833136900.
- [9] T. Janssen, G. Chapuis, and M. de Boissieu, *Aperiodic Crystals: From Modulated Phases to Quasicrystals* (Oxford University Press, Oxford ; New York, 2007).
- [10] P. J. Lu and P. J. Steinhardt, *Decagonal and Quasi-Crystalline Tilings in Medieval Islamic Architecture*, Science **315**, 1106 (2007).
- [11] P. Kramer and R. Neri, *On periodic and non-periodic space fillings of E^n obtained by projection*, Acta Crystallogr A Found Crystallogr **40**, 580 (1984).

- [12] V. Elser, *The diffraction pattern of projected structures*, Acta Crystallogr A Found Crystallogr **42**, 36 (1986).
- [13] A. L. Mackay, *Crystallography and the penrose pattern*, Physica A **114**, 609 (1982).
- [14] D. Levine and P. J. Steinhardt, *Quasicrystals: A New Class of Ordered Structures*, Phys. Rev. Lett. **53**, 2477 (1984).
- [15] P. J. Steinhardt, *Quasicrystals: A brief history of the impossible*, Rend. Fis. Acc. Lincei **24**, 85 (2013).
- [16] L. Pauling, *Apparent icosahedral symmetry is due to directed multiple twinning of cubic crystals*, Nature **317**, 512 (1985).
- [17] A.-P. Tsai, A. Inoue, and T. Masumoto, *A Stable Quasicrystal in Al-Cu-Fe System*, Jpn. J. Appl. Phys. **26**, L1505 (1987).
- [18] N. Wang, H. Chen, and K. H. Kuo, *Two-dimensional quasicrystal with eightfold rotational symmetry*, Phys. Rev. Lett. **59**, 1010 (1987).
- [19] A.-P. Tsai, *“Back to the Future”-An Account Discovery of Stable Quasicrystals*, Acc. Chem. Res. **36**, 31 (2003).
- [20] IUCr, *Report of the Executive Committee for 1991*, Acta Crystallogr A Found Crystallogr **48**, 922 (1992).
- [21] R. Lifshitz, *The square Fibonacci tiling*, J. Alloys Compd. **342**, 186 (2002).
- [22] T. Dotera, S. Bekku, and P. Ziherl, *Bronze-mean hexagonal quasicrystal*, Nature Mater **16**, 987 (2017).
- [23] F. Beenker, *Algebraic Theory of Non-Periodic Tilings of the Plane by Two Simple Building Blocks : A Square and a Rhombus* (Eindhoven University of Technology, 1982).
- [24] Y. Watanabe, M. Ito, and T. Soma, *Nonperiodic tessellation with eight-fold rotational symmetry*, Acta Crystallogr A Found Crystallogr **43**, 133 (1987).
- [25] M. Baake and D. Joseph, *Ideal and defective vertex configurations in the planar octagonal quasilattice*, Phys. Rev. B **42**, 8091 (1990).
- [26] R. Ammann, B. Grünbaum, and G. C. Shephard, *Aperiodic tiles*, Discrete Comput Geom **8**, 1 (1992).
- [27] P. Stampfli, *A dodecagonal quasi-periodic lattice in two dimensions*, Helv. Phys. Acta **59**, 1260 (1986).
- [28] J. Hermisson, C. Richard, and M. Baake, *A Guide to the Symmetry Structure of Quasiperiodic Tiling Classes*, J. Phys. I France **7**, 1003 (1997).

- [29] R. Lifshitz, *What is a crystal?*, Z. Kristallogr. Cryst. Mater. **222**, 313 (2007).
- [30] C. L. Henley. *Random Tiling Models*, volume 11, pages 429–524. WORLD SCIENTIFIC, (1991).
- [31] M. Baake and U. Grimm, *Aperiodic Order* (Cambridge University Press, Cambridge ; New York, 2013).
- [32] M. Baake, D. Écija, and U. Grimm, *A guide to lifting aperiodic structures*, Zeitschrift für Kristallographie - Crystalline Materials **231**, 507 (2016).
- [33] R. Lifshitz, *The symmetry of quasiperiodic crystals*, Physica A **232**, 633 (1996).
- [34] R. Lifshitz, *Symmetry Breaking and Order in the Age of Quasicrystals*, Isr. J. Chem. **51**, 1156 (2011).
- [35] M. de Boissieu, *Stability of quasicrystals: Energy, entropy and phason modes*, Philos. Mag. **86**, 1115 (2006).
- [36] C. L. Henley, M. de Boissieu, and W. Steurer, *Discussion on clusters, phasons and quasicrystal stabilisation*, Philos. Mag. **86**, 1131 (2006).
- [37] D. P. DiVincenzo, *Quasicrystals: The State of the Art* (World Scientific, Singapore, 1999).
- [38] X. Zeng, G. Ungar, Y. Liu, V. Percec, A. E. Dulcey, and J. K. Hobbs, *Supramolecular dendritic liquid quasicrystals*, Nature **428**, 157 (2004).
- [39] Y. S. Chan, C. T. Chan, and Z. Y. Liu, *Photonic Band Gaps in Two Dimensional Photonic Quasicrystals*, Phys. Rev. Lett. **80**, 956 (1998).
- [40] W. Man, M. Megens, P. J. Steinhardt, and P. M. Chaikin, *Experimental measurement of the photonic properties of icosahedral quasicrystals*, Nature **436**, 993 (2005).
- [41] W. Steurer and D. Sutter-Widmer, *Photonic and phononic quasicrystals*, J. Phys. D: Appl. Phys. **40**, R229 (2007).
- [42] M. Florescu, S. Torquato, and P. J. Steinhardt, *Complete band gaps in two-dimensional photonic quasicrystals*, Phys. Rev. B **80**, 155112 (2009).
- [43] A.-P. Tsai, *Discovery of stable icosahedral quasicrystals: Progress in understanding structure and properties*, Chem. Soc. Rev. **42**, 5352 (2013).
- [44] A. P. Tsai, J. Q. Guo, E. Abe, H. Takakura, and T. J. Sato, *A stable binary quasicrystal*, Nature **408**, 537 (2000).

- [45] L. Bindi, W. Kolb, G. N. Eby, P. D. Asimow, T. C. Wallace, and P. J. Steinhardt, *Accidental synthesis of a previously unknown quasicrystal in the first atomic bomb test*, Proc Natl Acad Sci USA **118**, e2101350118 (2021).
- [46] S. Fischer, A. Exner, K. Zielske, J. Perlich, S. Deloudi, W. Steurer, P. Lindner, and S. Förster, *Colloidal quasicrystals with 12-fold and 18-fold diffraction symmetry*, Proc. Natl. Acad. Sci. U.S.A. **108**, 1810 (2011).
- [47] C. Xiao, N. Fujita, K. Miyasaka, Y. Sakamoto, and O. Terasaki, *Dodecagonal tiling in mesoporous silica*, Nature **487**, 349 (2012).
- [48] K. Hayashida, T. Dotera, A. Takano, and Y. Matsushita, *Polymeric Quasicrystal: Mesoscopic Quasicrystalline Tiling in A B C Star Polymers*, Phys. Rev. Lett. **98**, 195502 (2007).
- [49] T. M. Gillard, S. Lee, and F. S. Bates, *Dodecagonal quasicrystalline order in a diblock copolymer melt*, Proc. Natl. Acad. Sci. U.S.A. **113**, 5167 (2016).
- [50] D. V. Talapin, E. V. Shevchenko, M. I. Bodnarchuk, X. Ye, J. Chen, and C. B. Murray, *Quasicrystalline order in self-assembled binary nanoparticle superlattices*, Nature **461**, 964 (2009).
- [51] D. Wang, T. Dasgupta, E. B. van der Wee, D. Zanaga, T. Altantzis, Y. Wu, G. M. Coli, C. B. Murray, S. Bals, M. Dijkstra, and A. van Blaaderen, *Binary icosahedral quasicrystals of hard spheres in spherical confinement*, arXiv:1906.10088 [cond-mat] (2019).
- [52] V. Elser, *Comment on "Quasicrystals: A New Class of Ordered Structures"*, Phys. Rev. Lett. **54**, 1730 (1985).
- [53] L. Bindi, P. J. Steinhardt, N. Yao, and P. J. Lu, *Natural Quasicrystals*, Science **324**, 1306 (2009).
- [54] L. Bindi, J. M. Eiler, Y. Guan, L. S. Hollister, G. MacPherson, P. J. Steinhardt, and N. Yao, *Evidence for the extraterrestrial origin of a natural quasicrystal*, Proc. Natl. Acad. Sci. U.S.A. **109**, 1396 (2012).
- [55] S. Dworkin and J.-I. Shieh, *Deceptions in quasicrystal growth*, Commun.Math. Phys. **168**, 337 (1995).
- [56] W. Steurer, *On a Realistic Growth Mechanism for Quasicrystals*, Z. anorg. allg. Chem. **637**, 1943 (2011).
- [57] P. A. Bancel, *Dynamical phasons in a perfect quasicrystal*, Phys. Rev. Lett. **63**, 2741 (1989).

- [58] K. Yue, M. Huang, R. L. Marson, J. He, J. Huang, Z. Zhou, J. Wang, C. Liu, X. Yan, K. Wu, Z. Guo, H. Liu, W. Zhang, P. Ni, C. Wesdemiotis, W.-B. Zhang, S. C. Glotzer, and S. Z. D. Cheng, *Geometry induced sequence of nanoscale Frank–Kasper and quasicrystal mesophases in giant surfactants*, Proc Natl Acad Sci USA **113**, 14195 (2016).
- [59] M. Oxborrow and C. L. Henley, *Random square-triangle tilings: A model for twelvefold-symmetric quasicrystals*, Phys. Rev. B **48**, 6966 (1993).
- [60] M. Shin and K. J. Strandburg, *Random tiling approach to the structure of decagonal quasicrystals*, J. Non Cryst. Solids **153–154**, 253 (1993).
- [61] M. Widom, *Bethe ansatz solution of the square-triangle random tiling model*, Phys. Rev. Lett. **70**, 2094 (1993).
- [62] P. A. Kalugin, *The square-triangle random-tiling model in the thermodynamic limit*, J. Phys. A: Math. Gen. **27**, 3599 (1994).
- [63] A. Kiselev, M. Engel, and H.-R. Trebin, *Confirmation of the Random Tiling Hypothesis for a Decagonal Quasicrystal*, Phys. Rev. Lett. **109**, 225502 (2012).
- [64] N. D. Mermin and S. M. Troian, *Mean-Field Theory of Quasicrystalline Order*, Phys. Rev. Lett. **54**, 1524 (1985).
- [65] J. E. S. Socolar, T. C. Lubensky, and P. J. Steinhardt, *Phonons, phasons, and dislocations in quasicrystals*, Phys. Rev. B **34**, 3345 (1986).
- [66] R. Lifshitz and H. Diamant, *Soft quasicrystals—Why are they stable?*, Philos Mag **87**, 3021 (2007).
- [67] K. Barkan, H. Diamant, and R. Lifshitz, *Stability of quasicrystals composed of soft isotropic particles*, Phys. Rev. B **83**, 172201 (2011).
- [68] A. W. Huran, H.-C. Wang, and M. A. L. Marques, *Two-dimensional binary metal-oxide quasicrystal approximants*, 2D Mater. (2021).
- [69] Z. Wang, T.-Y. Chang, and D. Xu, *Spontaneously formed quasicrystal grains in a pure metal*, AIP Adv. **11**, 015141 (2021).
- [70] J. C. Johnston, N. Kastelowitz, and V. Molinero, *Liquid to quasicrystal transition in bilayer water*, J. Chem. Phys. **133**, 154516 (2010).
- [71] J. C. Johnston, S. Phippen, and V. Molinero, *A Single-Component Silicon Quasicrystal*, J. Phys. Chem. Lett. **2**, 384 (2011).
- [72] M. Widom, K. J. Strandburg, and R. H. Swendsen, *Quasicrystal equilibrium state*, Phys. Rev. Lett. **58**, 706 (1987).
- [73] P. W. Leung, C. L. Henley, and G. V. Chester, *Dodecagonal order in a two-dimensional Lennard-Jones system*, Phys. Rev. B **39**, 446 (1989).

- [74] C. N. Likos and C. L. Henley, *Complex alloy phases for binary hard-disc mixtures*, Philos. Mag. B **68**, 85 (1993).
- [75] D. Salgado-Blanco and C. I. Mendoza, *Non-additive simple potentials for pre-programmed self-assembly*, Soft Matter **11**, 889 (2015).
- [76] H. M. Cataldo, *Stability of a hard-sphere binary quasicrystal*, Philos. Mag. B **79**, 1603 (1999).
- [77] C. R. Iacovella, A. S. Keys, and S. C. Glotzer, *Self-assembly of soft-matter quasicrystals and their approximants*, Proc. Natl. Acad. Sci. U.S.A. **108**, 20935 (2011).
- [78] M. Engel, P. F. Damasceno, C. L. Phillips, and S. C. Glotzer, *Computational self-assembly of a one-component icosahedral quasicrystal*, Nature Mater **14**, 109 (2015).
- [79] P. F. Damasceno, S. C. Glotzer, and M. Engel, *Non-close-packed three-dimensional quasicrystals*, J. Phys.: Condens. Matter **29**, 234005 (2017).
- [80] A. Metere, P. Oleynikov, M. Dzugutov, and S. Lidin, *A smectic dodecagonal quasicrystal*, Soft Matter **12**, 8869 (2016).
- [81] A. J. Archer, A. M. Rucklidge, and E. Knobloch, *Quasicrystalline Order and a Crystal-Liquid State in a Soft-Core Fluid*, Phys. Rev. Lett. **111**, 165501 (2013).
- [82] M. Zu, P. Tan, and N. Xu, *Forming quasicrystals by monodisperse soft core particles*, Nat Commun **8**, 2089 (2017).
- [83] Y. D. Fomin, E. A. Gaiduk, E. N. Tsiok, and V. N. Ryzhov, *The phase diagram and melting scenarios of two-dimensional Hertizian spheres*, Molecular Physics **116**, 3258 (2018).
- [84] G. Malescio and F. Sciortino, *Self-assembly of quasicrystals and their approximants in fluids with bounded repulsive core and competing interactions*, J. Mol. Liq. **349**, 118209 (2022).
- [85] C. Duan, M. Zhao, Y. Qiang, L. Chen, W. Li, F. Qiu, and A.-C. Shi, *Stability of Two-Dimensional Dodecagonal Quasicrystalline Phase of Block Copolymers*, Macromolecules **51**, 7713 (2018).
- [86] E. A. Jagla, *Phase behavior of a system of particles with core collapse*, Phys. Rev. E **58**, 1478 (1998).
- [87] T. Dotera, T. Oshiro, and P. Ziherl, *Mosaic two-lengthscale quasicrystals*, Nature **506**, 208 (2014).
- [88] H. Pattabhiraman, A. P. Gantapara, and M. Dijkstra, *On the stability of a quasicrystal and its crystalline approximant in a system of hard disks with a soft corona*, J. Chem. Phys. **143**, 164905 (2015).

- [89] R. Ryltsev, B. Klumov, and N. Chetelkatchev, *Self-assembly of the decagonal quasicrystalline order in simple three-dimensional systems*, Soft Matter **11**, 6991 (2015).
- [90] H. G. Schoberth, H. Emmerich, M. Holzinger, M. Dulle, S. Förster, and T. Gruhn, *Molecular dynamics study of colloidal quasicrystals*, Soft Matter **12**, 7644 (2016).
- [91] A. Haji-Akbari, M. Engel, A. S. Keys, X. Zheng, R. G. Petschek, P. Palffy-Muhoray, and S. C. Glotzer, *Disordered, quasicrystalline and crystalline phases of densely packed tetrahedra*, Nature **462**, 773 (2009).
- [92] K. Je, S. Lee, E. G. Teich, M. Engel, and S. C. Glotzer, *Entropic formation of a thermodynamically stable colloidal quasicrystal with negligible phason strain*, Proc. Natl. Acad. Sci. U.S.A. **118**, e2011799118 (2021).
- [93] R. van Damme, G. M. Coli, R. van Roij, and M. Dijkstra, *Classifying Crystals of Rounded Tetrahedra and Determining Their Order Parameters Using Dimensionality Reduction*, ACS Nano (2020).
- [94] M. N. van der Linden, J. P. K. Doye, and A. A. Louis, *Formation of dodecagonal quasicrystals in two-dimensional systems of patchy particles*, J. Chem. Phys. **136**, 054904 (2012).
- [95] A. Reinhardt, F. Romano, and J. P. K. Doye, *Computing Phase Diagrams for a Quasicrystal-Forming Patchy-Particle System*, Phys. Rev. Lett. **110**, 255503 (2013).
- [96] A. Reinhardt, J. S. Schreck, F. Romano, and J. P. K. Doye, *Self-assembly of two-dimensional binary quasicrystals: A possible route to a DNA quasicrystal*, J. Phys.: Condens. Matter **29**, 014006 (2017).
- [97] A. Gemeinhardt, M. Martinsons, and M. Schmiedeberg, *Stabilizing quasicrystals composed of patchy colloids by narrowing the patch width*, EPL **126**, 38001 (2019).
- [98] D. F. Tracey, E. G. Noya, and J. P. K. Doye, *Programming patchy particles to form three-dimensional dodecagonal quasicrystals*, J. Chem. Phys. **154**, 194505 (2021).
- [99] E. G. Noya, C. K. Wong, P. Llombart, and J. P. K. Doye, *How to design an icosahedral quasicrystal through directional bonding*, Nature **596**, 367 (2021).
- [100] R. Veneziano, S. Ratanalert, K. Zhang, F. Zhang, H. Yan, W. Chiu, and M. Bathe, *Designer nanoscale DNA assemblies programmed from the top down*, Science **352**, 1534 (2016).
- [101] B. Pansu and J.-F. Sadoc, *Metallurgy of soft spheres with hard core: From BCC to Frank-Kasper phases*, Eur. Phys. J. E **40**, 102 (2017).

- [102] B. Pansu, C. Goldmann, D. Constantin, M. Impérator-Clerc, and J.-F. Sadoc, *Softness-driven complexity in supercrystals of gold nanoparticles*, Soft Matter **17**, 6461 (2021).
- [103] A. Van Blaaderen and A. Vrij, *Synthesis and characterization of colloidal dispersions of fluorescent, monodisperse silica spheres*, Langmuir **8**, 2921 (1992).
- [104] R. P. A. Dullens, *Colloidal hard spheres: Cooking and looking*, Soft Matter **2**, 805 (2006).
- [105] C. P. Royall, W. C. K. Poon, and E. R. Weeks, *In search of colloidal hard spheres*, Soft Matter **9**, 17 (2013).
- [106] A. L. Thorneywork, R. Roth, D. G. A. L. Aarts, and R. P. A. Dullens, *Communication: Radial distribution functions in a two-dimensional binary colloidal hard sphere system*, J. Chem. Phys. **140**, 161106 (2014).
- [107] A. L. Thorneywork, J. L. Abbott, D. G. A. L. Aarts, and R. P. A. Dullens, *Two-Dimensional Melting of Colloidal Hard Spheres*, Phys. Rev. Lett. **118**, 158001 (2017).
- [108] M. H. Kim, S. H. Im, and O. O. Park, *Rapid fabrication of two-and three-dimensional colloidal crystal films via confined convective assembly*, Adv. Funct. Mater. **15**, 1329 (2005).
- [109] J. Yu, Q. Yan, and D. Shen, *Co-self-assembly of binary colloidal crystals at the air- water interface*, ACS Appl. Mater. Interfaces **2**, 1922 (2010).
- [110] J. Zhang, Y. Li, X. Zhang, and B. Yang, *Colloidal self-assembly meets nanofabrication: From two-dimensional colloidal crystals to nanostructure arrays*, Adv. Mater. **22**, 4249 (2010).
- [111] A. Dong, X. Ye, J. Chen, and C. B. Murray, *Two-dimensional binary and ternary nanocrystal superlattices: The case of monolayers and bilayers*, Nano Lett. **11**, 1804 (2011).
- [112] J.-T. Zhang, L. Wang, D. N. Lamont, S. S. Velankar, and S. A. Asher, *Fabrication of large-area two-dimensional colloidal crystals*, Angew. Chem. Int. Ed. **51**, 6117 (2012).
- [113] V. Lotito and T. Zambelli, *Approaches to self-assembly of colloidal monolayers: A guide for nanotechnologists*, Adv. Colloid Interface Sci. **246**, 217 (2017).
- [114] M. Dijkstra, *Phase behavior of nonadditive hard-sphere mixtures*, Phys. Rev. E **58**, 7523 (1998).
- [115] A. A. Louis, R. Finken, and J. Hansen, *Crystallization and phase separation in nonadditive binary hard-sphere mixtures*, Phys. Rev. E **61**, R1028 (2000).

- [116] F. Saija and P. Giaquinta, *Monte carlo simulation and phase behavior of nonadditive hard-core mixtures in two dimensions*, J. Chem. Phys. **117**, 5780 (2002).
- [117] A. Widmer-Cooper and P. Harrowell, *Structural phases in non-additive soft-disk mixtures: Glasses, substitutional order, and random tilings*, J. Chem. Phys. **135**, 224515 (2011).
- [118] D. Salgado-Blanco and C. I. Mendoza, *Non-additive simple potentials for pre-programmed self-assembly*, Soft Matter **11**, 889 (2015).
- [119] F. L. Tóth, *Über die dichteste Kugellagerung*, Math Z **48**, 676 (1942).
- [120] G. Blind, *über Unterdeckungen der Ebene durch Kreise.*, J. Reine Angew. Math. **1969**, 145 (1969).
- [121] T. Kennedy, *Compact Packings of the Plane with Two Sizes of Discs*, Discrete Comput Geom **35**, 255 (2006).
- [122] N. Bédaride and T. Fernique, *Density of Binary Disc Packings: The Nine Compact Packings*, Discrete Comput Geom **67**, 787 (2022).
- [123] T. Fernique, *Density of Binary Disc Packings: Lower and Upper Bounds*, Exp. Math. (2022).
- [124] L. Filion, M. Marechal, B. van Oorschot, D. Pelt, F. Smalenburg, and M. Dijkstra, *Efficient Method for Predicting Crystal Structures at Finite Temperature: Variable Box Shape Simulations*, Phys. Rev. Lett. **103**, 188302 (2009).
- [125] J. de Graaf, L. Filion, M. Marechal, R. van Roij, and M. Dijkstra, *Crystal-structure prediction via the Floppy-Box Monte Carlo algorithm: Method and application to hard (non)convex particles*, J. Chem. Phys. **137**, 214101 (2012).
- [126] S. Torquato and Y. Jiao, *Dense packings of the Platonic and Archimedean solids*, Nature **460**, 876 (2009).
- [127] M. Marechal, U. Zimmermann, and H. Löwen, *Freezing of parallel hard cubes with rounded edges*, J. Chem. Phys. **136**, 144506 (2012).
- [128] E. Bianchi, G. Doppelbauer, L. Filion, M. Dijkstra, and G. Kahl, *Predicting patchy particle crystals: Variable box shape simulations and evolutionary algorithms*, J. Chem. Phys. **136**, 214102 (2012).
- [129] T. Vissers, Z. Preisler, F. Smalenburg, M. Dijkstra, and F. Sciortino, *Predicting crystals of Janus colloids*, J. Chem. Phys. **138**, 164505 (2013).
- [130] I. Staneva and D. Frenkel, *The role of non-specific interactions in a patchy model of protein crystallization*, J. Chem. Phys. **143**, 194511 (2015).

- [131] A. Gabriëlse, H. Löwen, and F. Smalenburg, *Low-Temperature Crystal Structures of the Hard Core Square Shoulder Model*, Materials **10**, 1280 (2017).
- [132] W. Shen, J. Antonaglia, J. A. Anderson, M. Engel, G. van Anders, and S. C. Glotzer, *Symmetries in hard polygon systems determine plastic colloidal crystal mesophases in two dimensions*, Soft Matter **15**, 2571 (2019).
- [133] A. Meurer, C. P. Smith, M. Paprocki, O. Čertík, S. B. Kirpichev, M. Rocklin, A. Kumar, S. Ivanov, J. K. Moore, S. Singh, T. Rathnayake, S. Vig, B. E. Granger, R. P. Muller, F. Bonazzi, H. Gupta, S. Vats, F. Johansson, F. Pedregosa, M. J. Curry, A. R. Terrel, Š. Roučka, A. Saboo, I. Fernando, S. Kulal, R. Cimrman, and A. Scopatz, *SymPy: Symbolic computing in Python*, PeerJ Computer Science **3**, e103 (2017).
- [134] O. Uche, F. Stillinger, and S. Torquato, *Concerning maximal packing arrangements of binary disk mixtures*, Physica A **342**, 428 (2004).
- [135] S.-C. Mau and D. A. Huse, *Stacking entropy of hard-sphere crystals*, Phys. Rev. E **59**, 4396 (1999).
- [136] E. G. Noya and N. G. Almarza, *Entropy of hard spheres in the close-packing limit*, Molecular Physics **113**, 1061 (2015).
- [137] T. Fernique, A. Hashemi, and O. Sizova, in *Discrete Geometry for Computer Imagery*, edited by M. Couprie, J. Cousty, Y. Kenmochi, and N. Mustafa (Springer International Publishing, Cham, 2019).
- [138] H. Kawamura, *Statistics of Two-Dimensional Amorphous Lattice*, Prog. Theor. Phys. **70**, 352 (1983).
- [139] B. Nienhuis, *Exact solution of random tiling models*, Phys. Rep. **301**, 271 (1998).
- [140] M. Impérator-Clerc, A. Jagannathan, P. Kalugin, and J.-F. Sadoc, *Square-triangle tilings: An infinite playground for soft matter*, Soft Matter **17**, 9560 (2021).
- [141] H. Kawamura, *Entropy of the random triangle-square tiling*, Physica A **177**, 73 (1991).
- [142] E. Fayen, A. Jagannathan, G. Foffi, and F. Smalenburg, *Infinite-pressure phase diagram of binary mixtures of (non)additive hard disks*, J. Chem. Phys. **152**, 204901 (2020).
- [143] P. M. Reis, R. A. Ingale, and M. D. Shattuck, *Crystallization of a Quasi-Two-Dimensional Granular Fluid*, Phys. Rev. Lett. **96**, 258001 (2006).

- [144] N. Mujica and R. Soto, in *Recent Advances in Fluid Dynamics with Environmental Applications*, edited by J. Klapp, L. D. G. Sigalotti, A. Medina, A. López, and G. Ruiz-Chavarría (Springer International Publishing, Cham, 2016).
- [145] D. Frenkel and B. Smit, *Understanding Molecular Simulation: From Algorithms to Applications* (Academic Press, San Diego, 2002).
- [146] M. P. Allen and D. J. Tildesley, *Computer Simulation of Liquids* (Oxford University Press, Oxford, United Kingdom, 2017).
- [147] B. D. Lubachevsky, *How to simulate billiards and similar systems*, J. Comput. Phys. **94**, 255 (1991).
- [148] D. C. Rapaport, *The Art of Molecular Dynamics Simulation* (Cambridge University Press, Cambridge, UK ; New York, NY, 2004).
- [149] A. Donev, S. Torquato, and F. H. Stillinger, *Neighbor list collision-driven molecular dynamics simulation for nonspherical hard particles. I. Algorithmic details*, J. Comput. Phys. **202**, 737 (2005).
- [150] G. Paul, *A Complexity $O(1)$ priority queue for event driven molecular dynamics simulations*, J. Comput. Phys. **221**, 615 (2007).
- [151] F. Smalenburg, *Efficient event-driven simulations of hard spheres*, Eur. Phys. J. E **45**, 22 (2022).
- [152] M. Engel, J. A. Anderson, S. C. Glotzer, M. Isobe, E. P. Bernard, and W. Krauth, *Hard-disk equation of state: First-order liquid-hexatic transition in two dimensions with three simulation methods*, Phys. Rev. E **87**, 042134 (2013).
- [153] N. D. Mermin, *Crystalline Order in Two Dimensions*, Phys. Rev. **176**, 250 (1968).
- [154] B. Illing, S. Fritschi, H. Kaiser, C. L. Klix, G. Maret, and P. Keim, *Mermin–Wagner fluctuations in 2D amorphous solids*, Proc. Natl. Acad. Sci. U.S.A. **114**, 1856 (2017).
- [155] F. F. Abraham, *Melting in Two Dimensions is First Order: An Isothermal-Isobaric Monte Carlo Study*, Phys. Rev. Lett. **44**, 463 (1980).
- [156] R. C. Thompson-Flagg, M. J. B. Moura, and M. Marder, *Rippling of graphene*, Europhys. Lett. **85**, 46002 (2009).
- [157] P. W. Leung, C. L. Henley, and G. V. Chester, *Dodecagonal order in a two-dimensional Lennard-Jones system*, Phys. Rev. B **39**, 446 (1989).
- [158] X. Ye, J. Chen, M. Eric Irrgang, M. Engel, A. Dong, S. C. Glotzer, and C. B. Murray, *Quasicrystalline nanocrystal superlattice with partial matching rules*, Nature Mater **16**, 214 (2017).

- [159] A. Haji-Akbari, M. Engel, and S. C. Glotzer, *Degenerate Quasicrystal of Hard Triangular Bipyramids*, Phys. Rev. Lett. **107**, 215702 (2011).
- [160] P. Kalugin and A. Katz, *Robust minimal matching rules for quasicrystals*, Acta Crystallogr A Found Adv **75**, 669 (2019).
- [161] T. Fernique, A. Hashemi, and O. Sizova, *Compact Packings of the Plane with Three Sizes of Discs*, Discrete Comput Geom **66**, 613 (2021).
- [162] D. Joseph and V. Elser, *A Model of Quasicrystal Growth*, Phys. Rev. Lett. **79**, 1066 (1997).
- [163] A. S. Keys and S. C. Glotzer, *How do Quasicrystals Grow?*, Phys. Rev. Lett. **99**, 235503 (2007).
- [164] J.-F. Sadoc and R. Mosseri, *Quasiperiodic Frank–Kasper phases derived from the square–triangle dodecagonal tiling*, Struct Chem **28**, 63 (2017).
- [165] J. de Gier and B. Nienhuis, *The exact solution of an octagonal rectangle–triangle random tiling*, J Stat Phys **87**, 415 (1997).
- [166] J. M. Kosterlitz and D. J. Thouless, *Ordering, metastability and phase transitions in two-dimensional systems*, J. Phys. C: Solid State Phys. **6**, 1181 (1973).
- [167] B. I. Halperin and D. R. Nelson, *Theory of Two-Dimensional Melting*, Phys. Rev. Lett. **41**, 121 (1978).
- [168] A. P. Young, *Melting and the vector Coulomb gas in two dimensions*, Phys. Rev. B **19**, 1855 (1979).
- [169] C. H. Mak, *Large-scale simulations of the two-dimensional melting of hard disks*, Phys. Rev. E **73**, 065104 (2006).
- [170] B. Li, Y. Nishikawa, P. Hoellmer, L. Carillo, A. C. Maggs, and W. Krauth, *Hard-disk computer simulations – a historic perspective*, (2022).
- [171] J. Russo and N. B. Wilding, *Disappearance of the Hexatic Phase in a Binary Mixture of Hard Disks*, Phys. Rev. Lett. **119**, 115702 (2017).
- [172] E. Fayen, M. Impérator-Clerc, L. Filion, G. Foffi, and F. Smalenburg, *Self-assembly of dodecagonal and octagonal quasicrystals in hard spheres on a plane*, (2022).
- [173] A. Santos, M. López de Haro, and S. B. Yuste, *Equation of state of non-additive D-dimensional hard-sphere mixtures*, J. Chem. Phys. **122**, 024514 (2005).
- [174] C. Vega, E. Sanz, J. L. F. Abascal, and E. G. Noya, *Determination of phase diagrams via computer simulation: Methodology and applications to water, electrolytes and proteins*, J. Phys.: Condens. Matter **20**, 153101 (2008).

- [175] D. Henderson, *A simple equation of state for hard discs*, Mol. Phys. **30**, 971 (1975).
- [176] D. Frenkel, *Simulations: The dark side*, Eur. Phys. J. Plus **128**, 10 (2013).
- [177] B. J. Alder and T. E. Wainwright, *Phase Transition in Elastic Disks*, Phys. Rev. **127**, 359 (1962).
- [178] E. P. Bernard and W. Krauth, *Two-Step Melting in Two Dimensions: First-Order Liquid-Hexatic Transition*, Phys. Rev. Lett. **107**, 155704 (2011).
- [179] J. E. Lennard-Jones and A. F. Devonshire, *Critical phenomena in gases - I*, Proc. R. Soc. Lond. A **163**, 53 (1937).
- [180] X. Cottin and P. A. Monson, *A cell theory for solid solutions: Application to hard sphere mixtures*, J. Chem. Phys. **99**, 8914 (1993).
- [181] X. Cottin and P. A. Monson, *Solid-fluid phase equilibrium for single component and binary Lennard-Jones systems: A cell theory approach*, J. Chem. Phys. **105**, 10022 (1996).
- [182] R. Wheatley, *Phase diagrams for hard disc mixtures*, Mol. Phys. **93**, 965 (1998).
- [183] D. Frenkel and A. J. C. Ladd, *New Monte Carlo method to compute the free energy of arbitrary solids. Application to the fcc and hcp phases of hard spheres*, J. Chem. Phys. **81**, 3188 (1984).
- [184] J. M. Polson, E. Trizac, S. Pronk, and D. Frenkel, *Finite-size corrections to the free energies of crystalline solids*, J. Chem. Phys. **112**, 5339 (2000).
- [185] N. G. Almaraz, *Computation of the free energy of solids*, J. Chem. Phys. **126**, 211103 (2007).
- [186] C. Vega and E. G. Noya, *Revisiting the Frenkel-Ladd method to compute the free energy of solids: The Einstein molecule approach*, J. Chem. Phys. **127**, 154113 (2007).
- [187] T. Schilling and F. Schmid, *Computing absolute free energies of disordered structures by molecular simulation*, J. Chem. Phys. **131**, 231102 (2009).
- [188] H. Flyvbjerg and H. G. Petersen, *Error estimates on averages of correlated data*, J. Chem. Phys. **91**, 461 (1989).
- [189] R. A. LaCour, T. C. Moore, and S. C. Glotzer, *Tuning Stoichiometry to Promote Formation of Binary Colloidal Superlattices*, arXiv:2112.06100 [cond-mat] (2021).
- [190] D. Frettlöeh, *A fractal fundamental domain with 12-fold symmetry*, Symmetry Cult. Sci **22**, 237 (2011).

- [191] X. Zeng and G. Ungar, *Inflation rules of square-triangle tilings: From approximants to dodecagonal liquid quasicrystals*, Philos. Mag. **86**, 1093 (2006).
- [192] W. W. Wood, *A Brief History of the Use of the Metropolis Method at LANL in the 1950s*, AIP Conf. Proc. **690**, (2003).
- [193] B. Rubinstein and S. I. Ben-Abraham, *The ‘random’ square-triangle tiling: Simulation of growth*, Mat. Sci. Eng. A **294–296**, 418 (2000).
- [194] Y. Komatsu and H. Tanaka, *Roles of Energy Dissipation in a Liquid-Solid Transition of Out-of-Equilibrium Systems*, Phys. Rev. X **5**, 031025 (2015).
- [195] G. Briand and O. Dauchot, *Crystallization of Self-Propelled Hard Discs*, Phys. Rev. Lett. **117**, 098004 (2016).
- [196] A. Meurer, C. P. Smith, M. Paprocki, O. Čertík, S. B. Kirpichev, M. Rocklin, A. Kumar, S. Ivanov, J. K. Moore, S. Singh, T. Rathnayake, S. Vig, B. E. Granger, R. P. Muller, F. Bonazzi, H. Gupta, S. Vats, F. Johansson, F. Pedregosa, M. J. Curry, A. R. Terrel, Š. Roučka, A. Saboo, I. Fernando, S. Kulal, R. Cimrman, and A. Scopatz, *SymPy: Symbolic computing in Python*, PeerJ Computer Science **3**, e103 (2017).